

EXCEEDING THE BIOCHEMICAL SPEED LIMIT OF FIBRINOLYSIS USING
MAGNETICALLY POWERED MICROWHEELS

by

Dante Disharoon

© Copyright by Dante Disharoon, 2021

All rights reserved

A thesis submitted to the Faculty and Board of Trustees of the Colorado School of Mines in partial fulfillment of the requirements for the degree of Doctor of Philosophy (Chemical Engineering).

Golden, Colorado

Date _____

Signed: _____

Dante Disharoon

Signed: _____

Dr. David W.M. Marr
Thesis Advisor

Signed: _____

Dr. Keith Neeves
Thesis Advisor

Golden, Colorado

Date _____

Signed: _____

Dr. Anuj Chauhan
Department Head
Department of Chemical and Biological Engineering

ABSTRACT

The biochemical lysis of blood clots, or thrombolysis, using tissue plasminogen activator (tPA) is an effective treatment option for some types of clots, but its use has been limited by its rate of transport to and dissolution of thrombi. This thesis develops a technology that could broaden the indications for thrombolytic therapy using rotating magnetic fields to assemble and direct drug-bearing microwheels (μ wheels) to target and lyse blood clots.

μ Wheels driven by rotating magnetic fields translate because of friction against a surface. The translational velocity of μ wheels depends on the thickness of the liquid gap separating them from the surface, which can be controlled by applying magnetic load and colloidal forces. μ Wheel rolling is characterized by stick-slip behavior where μ wheels near the surface “stick” and translate rapidly and μ wheels farther from the surface “slip” and translate slowly.

μ Wheels functionalized with tPA (tPA- μ wheels) can be targeted to plasma clots formed in vitro, demonstrating their utility as drug delivery vehicles. tPA- μ wheels are five- to tenfold more effective than therapeutic concentrations of free tPA because they translate more rapidly than diffusion and localize near the clot at concentrations two orders-of-magnitude above the bulk. However, at high tPA concentrations, fibrinolysis rates are limited by the concentration of tPA’s substrate, plasminogen. To address this biochemical limitation, plasminogen-laden mesoporous silica nanoparticles are conjugated to tPA- μ wheels (pgn-tPA- μ wheels) to co-deliver both molecules. Pgn-tPA- μ wheels match the maximum lysis rate achieved using artificially high concentrations of free plasminogen and tPA. By tuning the ratio of tPA to plasminogen and combining co-delivery with magnetically-driven mechanical action, we achieve lysis rates beyond what are possible using fibrinolytic agents alone.

TABLE OF CONTENTS

ABSTRACT.....	III
LIST OF FIGURES	IX
LIST OF TABLES	XIV
ACKNOWLEDGEMENTS	XV
CHAPTER 1: ENGINEERED MICRO- AND NANOPARTICLES FOR FIBRINOLYSIS	1
1.1 Summary	1
1.2 Introduction.....	2
1.3 Macromolecule modification of plasminogen activators.....	4
1.4 Encapsulation of plasminogen activators in liposomes and polymer particles.....	6
1.5 Coupling plasminogen activators to blood cells and blood cell mimics.....	8
1.6 Ultrasound mediated lysis and release	10
1.6.1 Echogenic Liposomes	10
1.6.2 Sonothrombolysis	10
1.7 Magnetic particles and magnetic field control.....	12
1.7.1 Synthesis and functionalization of magnetic nanoparticles carriers	12
1.7.2 Magnetic field control of magnetic particles	15
1.8 Outlook	19
1.9 References.....	20
CHAPTER 2: ASSEMBLY AND CONTROL OF MAGNETIC MICROWHEELS: A BRIEF SUMMARY	30
2.1 Introduction.....	30
2.2 Magnetic field generation and microwheel assembly.....	30
2.3 Microwheel translation	31

2.4 Conclusions.....	33
2.5 References.....	33
CHAPTER 3: AC/DC MAGNETIC FIELDS FOR ENHANCED TRANSLATION OF COLLOIDAL MICROWHEELS	35
3.1 Abstract.....	35
3.2 Introduction.....	36
3.3 Experimental Section	37
3.3.1 Superparamagnetic particles	37
3.3.2 Magnetic field application	38
3.3.3 Total Internal Reflection Microscopy	38
3.3.4 Preparation of Janus sphere	39
3.4 Results and Discussion	40
3.4.1 Gap width measurement for rolling spheres	40
3.5 Summary and Conclusions	44
3.6 References.....	45
CHAPTER 4: ENHANCED FIBINOLYSIS WITH MAGNETICALLY POWERED COLLOIDAL MICROWHEELS	49
CHAPTER 5: BREAKING THE FIBRINOLYTIC SPEED LIMIT WITH MICROWHEEL CO-DELIVERY OF TISSUE PLASMINOGEN ACTIVATOR AND PLASMINOGEN.....	50
5.1 Abstract.....	50
5.2 Introduction.....	51
5.3 Results.....	54
5.3.1 Plasminogen depletion limits fibrinolysis rate at high tPA concentrations .	54
5.3.2 Synthesis and characterization of plasminogen releasing magnetic colloids.....	55

5.3.3 Designing co-delivery strategy for tPA and plasminogen	56
5.3.4 Fibrinolysis with μ wheel co-delivery of tPA and plasminogen	60
5.4 Discussion	62
5.5 Materials and Methods	65
5.5.1 Materials	65
5.5.2 Synthesis of magnetic mesoporous silica nanoparticles (mMSN)	66
5.5.3 Characterization of mMSN	66
5.5.4 Co-functionalization of Dynabeads TM with tPA and pgn-mMSN	67
5.5.5 Magnetic field induced assembly and translation	67
5.5.6 Loading and release of plasminogen	68
5.5.7 Biotinylation of tPA	68
5.5.8 Measurement of tPA activity on functionalized beads	69
5.5.9 Modeling tPA and plasminogen concentrations at the lysis front	69
5.5.10 Fabrication of microfluidic devices	71
5.5.11 Fibrinolysis experiments	71
5.6 References	72
CHAPTER 6: CONCLUSION AND RECOMMENDATIONS	78
6.1 Summary	78
6.2 Outlook and recommendations	79
6.2.1 Modular co-delivery for different clot morphologies	79
6.2.1.1 Remediating exclusion of plasminogen from retracted clots	80
6.2.1.2 μ Wheels targeted to platelets	80
6.2.1.3 μ Wheels targeted to deoxyribonucleic acid (DNA)	81
6.2.2 Materials design	81

6.2.2.1 Biocompatibility	81
6.2.2.2 Ternary complex between immobilized tPA, plasminogen and fibrin.....	82
6.2.2.3 Controlled release	83
6.2.3 Hyperthermia	84
6.3 Conclusion	84
6.4 References.....	84
APPENDIX A: SUPPLEMENTARY MATERIALS FOR CHAPTER 3.....	89
APPENDIX B: ENHANCED FIBRINOLYSIS WITH MAGNETICALLY POWERED COLLOIDAL MICROWHEELS	92
B.1 Abstract	92
B.2 Introduction	93
B.3 Results and Discussion.....	96
B.4 Conclusions	108
B.5 Experimental Section	109
B.5.1 Magnetic Field Setup	109
B.5.2 Wheel Assembly and Motion.....	109
B.5.3 Preparation of tPA Conjugated Beads.....	110
B.5.4 Concentration Profiles.....	110
B.5.5 Fibrinolysis Experiments.....	111
B.5.6 tPA Activity Measurements	112
B.5.7 Blood Collection and Preparation	112
B.5.8 Microfluidic Model of Hemostasis	113
B.5.9 Statistical Analysis	115

B.6 References	115
APPENDIX C: SUPPLEMENTARY MATERIALS FOR APPENDIX B.....	120
APPENDIX D: SUPPLEMENTARY MATERIALS FOR CHAPTER 5.....	122
APPENDIX E: LIST OF ADDITIONAL FILES	124

LIST OF FIGURES

Figure 1.1: Overview of engineered particles for fibrinolysis covered in this review with features of different materials, targeting strategies, and actuation.	5
Figure 1.2: Mechanisms of assisting thrombolysis using ultrasound. A) Ultrasound forces cause ELIP to deliver a payload of PA near a thrombus. B) Sonic forces cause acoustic streaming that induces flow and improves transport of PA to a thrombus. C) Sonic forces cause cavitation, which imparts mechanical energy into the thrombus and initiates degradation even in the absence of PA. D) Microbubbles increase the frequency of cavitation and accelerate lysis. See Table 1.1 for details and references.	14
Figure 1.3: Methods of magnetic control of magnetic nanoparticles (MNP). A) MNP move down a magnetic field gradient toward a clot using a permanent magnet. B) A rotating magnet is used to rotate rod-like MNP, inducing convection and improving transport of PA to a clot. C) A high frequency magnetic field induces local heating of cube-like MNP. D) A low frequency rotating magnetic field causes MNP to assemble into microwheels and roll into a thrombus. See Table 1.2 for details and references.	17
Figure 2.1 A) A μ wheel in a rotating magnetic field (black arrows) in the xy-plane spins (red arrow) but does not translate. B) When a z component is added to the magnetic field (black arrows), the μ wheel rolls (red arrow) along the surface and translates (blue arrow).	31
Figure 2.2: Free body diagram of a μ wheel at camber angle θ_c , rotating at angular frequency ω , and translating at velocity V . A) The forces on the z axis are the load and normal forces. B) Friction and drag are the forces on the x axis.	33
Figure 3.1: Experimental apparatus. Coils generate an AC or AC/DC magnetic field that cause μ wheels to roll near a prism surface, scattering an evanescent wave created by a laser passing through the prism. Laser power is measured continuously via power meter. Scattered intensity is measured using a calibrated camera and normalized by laser output. Inset: $\Theta = 42^\circ$, $\Theta_1 = 70.1^\circ$, $\Theta_2 = 25.1^\circ$, $n_1 = 1.52$ and $n_2 = 1.33$	40
Figure 3.2: A) Normalized intensity in TIRM and calculated gap width for a single sphere transitioning from Brownian to rolling. The dotted line indicates the time when the AC field is turned on. The field strength is 4.5 mT and $\Omega = 30$ Hz. <i>The lines represent moving averages.</i> B) Gap width and velocity as a function of particle rotation rate [Video 3.S2]. Both velocity and gap width measurements at higher rotation rates are subject to large	

experimental error. Sources of error include variable particle density, magnetic doping, surface roughness, sphericity and size. Data represent the mean and standard deviation of $n = 25-450$ particles.41

Figure 3.3 Varying gap with DC-induced load force or screening electrostatic repulsion
 A) The load force is varied ± 0.2 Fg using a 2.5 mT DC magnetic field. Velocity and gap width are shown at field frequencies of 10, 20, and 40 Hz. B) NaCl concentration is varied to manipulate the Debye length (inset) for a field frequency of 40 Hz. Note that the data provided here is for non-sticking particles only. For A and B, $n = 250-1250$ measurements. C) Translational velocity as a function of gap width for particle rotation rates of $10 < \Omega < 40$. For AC/DC samples (red triangles), load force is 1.2 Fg. Data represent averages and standard deviation of $n = 25-450$ measurements. D) A force balance between frictional force F_f and drag force F_D provides a linear relationship between the translational velocity and experimental parameters. Error bars calculated from propagation of error in experimental measurements of v_b , Ω , and h43

Figure 3.4: A) The traction coefficient (1-s) follows the predicted scaling (dotted line) for all experimental conditions. B) A transition in slip is observed at a gap width of ~ 20 nm. Data summarizes experiments across all rotation frequencies and field conditions. C) Electron micrograph of a single colloidal particle and representative AFM image and surface roughness profile insets (corrected for curvature). Dashed line is the average height corrected for curvature. D) Instantaneous velocity measurements from representative data in B show stick-slip behavior at length scales less than or equal to the particle surface roughness (Video 3.S4).44

Figure 5.1: A) The rate-limiting steps of fibrinolysis include the transport to a clot and binding of tPA to fibrin fibers at low tPA concentrations. B) At sufficiently high tPA concentrations, its substrate plasminogen (pgn), becomes the limiting factor in fibrinolysis. C) These rate-limiting steps are overcome using magnetically powered μ wheels, superparamagnetic beads (orange spheres) that self-assemble in rotating magnetic fields. When μ wheels are coupled to tPA (tPA- μ wheels) they accumulate at the clot interface leading to high tPA concentrations and plasminogen limited fibrinolysis. D) By attaching plasminogen releasing nanoparticles (green spheres) to μ wheels (tPA-pgn- μ wheels) co-delivery of both enzyme and substrate are achieved yielding fibrinolysis rates that overcomes plasminogen-limited fibrinolysis.54

Figure 5.2: Measuring the fibrinolytic speed limit of plasma clots. A) Heat map of lysis rates as a function of tPA and plasminogen (pgn) concentrations. The bold border outlines the accelerated fibrinolysis (AF) zone. Symbols denote data shown in panel B. B) Dissolution of fibrin at 400 nM tPA with endogenous plasma plasminogen concentration (1 μ M) and the addition of exogenous plasminogen up to 6 μ M total plasminogen concentration.55

Figure 5.3: Synthesis and characterization of magnetic mesoporous silica nanoparticles (mMSN) and their coupling to superparamagnetic beads. A) Schematic of tPA-functionalization, mMSN-bead coupling, and plasminogen (pgn) loading to create tPA- and tPA-pgn- μ wheels. B) Transmission electron micrograph (TEM) of mMSN. Darker areas are Fe₃O₄ domains incorporated into the silica matrix. C) High-angle annular dark field energy-dispersive X-ray (HAADF-EDS) spectrum showing iron oxide domains (blue) distributed throughout silica matrix (green). D) Representative BJH isotherm data with TEM image of pore structure (inset). E) Magnetization profile for mMSN. F) Scanning electron micrograph (SEM) of studded beads.57

Figure 5.4 Representative velocity profile for tPA-beads (A) and pgn-tPA-beads (B). C) Plasminogen release profile for pgn-mMSN and pgn-tPA-beads at a number density of 10⁶/ μ L. Fractional release is normalized to the total plasminogen loading as measured by spectrometry. D) Activity of 10⁵/ μ L bead populations compared to solvated tPA.59

Figure 5.5 A) tPA activity as a function of coverage as measured using a fluorogenic substrate in a plate reader. B) Percentage of a 60 min experiment during which plasminogen concentration is within the accelerated fibrinolysis (AF) zones, defined as regions where lysis exceeds 13.5 μ m/min (see Fig. 5.2B). C) Coverage of mMSN to beads as a function of mixing time in the with and without a 4 mT magnetic field. D) Histogram of coverage for t = 24 hr in the presence of a 4 mT magnetic field (n=50). Data in (A) and (C) expressed as average and standard deviation of n = 3 and 25, respectively.60

Figure 5.6: A) Time lapse of lysis of plasma clots using different μ wheel formulations. Brightfield at left, and fluorescently labeled fibrin(ogen) at right. Dashed lines indicate the front position. B) Representative lysis curves for each formulation. Lines indicate periods of maximum lysis rates lasting for a minimum of 10 min. C) Maximum lysis rates for each formulation. Corkscrew condition uses pgn-tPA- μ wheels. Dashed line indicates biochemical speed limit (see Fig. 5.2B).63

Figure A.1: Left: Schematic of coils used to produce AC and DC magnetic fields. Brown coils produce AC rotating magnetic field while transparent gray coils produce DC fields to vary loads in the direction parallel to the gravitational field. Right: Experimental apparatus.89

Figure A.2: Electron micrographs of Ag Janus particles. Red crosses indicate regions with Ag. Representative EDX results for Ag and normal hemispheres. The carbon peak comes from the polystyrene and the silicon peak from the wafer substrate.90

Figure A.3: Particle rotation rate measured on Ag-coated Janus particles as a function of applied AC field frequency. The particle rotation rate equals the field frequency up to ~40 Hz.....91

Figure B.1: Approach to tPA- μ wheel-induced reperfusion of occluded channels. A,C,D) With application of a rotating magnetic field, \hat{B} , oriented out of the surface plane at a camber angle θ_c relative to the normal \hat{n} , colloids assemble, “stand up,” and roll along the surface. Color of vector tracing indicates field rotation angle. C) Because field orientation can be instantly changed, μ wheels can be quickly redirected and follow preprogrammed or manually controlled paths. Scale bar = 10 μm . B,E) With a rotating “corkscrew” field, an additional helical component to wheel motion can be induced. Scale bar = 10 μm (Video B.S1). While both modes can be used to assemble μ wheels and do lead to high concentration of μ wheels at the gel interface, F) direct motion based primarily on biochemical dissolution lyses slower than G) helical motion that yields combined mechanical and biochemical action.97

Figure B.2: Wheel-based drug transport overcomes diffusion limitations down stagnant channels. A) Upon application of the magnetic field, tPA- μ wheels accumulate at the front edge of the fibrin gel in a microfluidic device (rust colored region). Note the fibrin gel is present in the region separating the two reservoirs (see also Figure 3A). B) Larger μ wheels translate faster than smaller μ wheels as shown in red overlay ($\Delta t = 10$ s, scale bar = 10 μm). C) Measured tPA-wheel velocity distribution for direct motion ($N = 102$) with log-normal fit. D) Predicted tPA concentration C/C_0 at the gel front for $L = 1$ mm and both free tPA and μ wheel-bound tPA (see the Experimental Section). Corresponding measurements of μ wheel concentration at the interface shown as data points. Note that μ wheel concentration quickly exceeds the maximum concentration achievable via tPA diffusion alone. E) Driven by wheel rolling only, μ wheel accumulation at the gel front (right) is easily observed at low resolution (Video B.S2, scale bar = 200 μm).99

Figure B.3: Faster lysis occurs with tPA-coated beads and addition of corkscrew action. A) Illustration of Figure 2A where a plasma-derived fibrin gel is formed between two normal pooled plasma (NPP) reservoirs. Images and data acquired near the center of the dashed circle region. B) tPA-coated beads (left) penetrating by corkscrew motion into fibrin gel, magnetic field strength = 9 mT, frequency = 100 Hz; C) tPA-coated beads and direct motion; D) soluble tPA alone ($1 \mu\text{g mL}^{-1}$), scale bar = 40 μm . E) tPA and tPA-coated bead activity measured by cleavage of a fluorogenic substrate. F) Fibrinolysis velocity of tPA versus tPA- μ wheels for plasma-derived fibrin gels and gels formed with platelet rich plasma (PRP) (Video B.S3).....101

Figure B.4: An increasing volume of tPA- μ wheels penetrate into the gel as time proceeds via direct (biochemical) or corkscrew (biochemical + mechanical) lysis

modes. A–D) Snapshot of Video B.S3 ($t = 6$ min) where improved penetration via corkscrew motion is apparent. E) Bead penetration with smaller wheels penetrating deeper. F) Penetrating beads with distribution of large and small wheels for direct motion. G) Corkscrew mode with higher total bead number penetration at shallower depth at short times. H) Penetrating bead distribution for corkscrew motion.106

Figure B.5: Fibrinolysis of a platelet-rich thrombus in a microfluidic model of hemostasis by tPA- μ wheels. Snapshots from Video B.S5 (Supporting Information) at 0, 15, and 30 min. The thrombus occludes the horizontal channel coated with collagen-mimetic peptides and tissue factor. Following occlusion, μ wheels are introduced from the left vertical channel with blood present in the right vertical channel. A–C) Brightfield images of μ wheels accumulating at and penetrating into the thrombus. Epifluorescence of D–F) fibrin(ogen) and G–I) platelets.107

Figure C.1: Fibrinolysis velocity of PA versus tPA- μ wheels in fibrin gels derived from normal pooled plasma (NPP) with exogenous fibrinogen (final fibrinogen concentration = 10 μ g/mL. (Video B.S4).120

Figure C.2: Thrombus formation and tPA- μ wheel fibrinolysis in a microfluidic model of hemostasis. A. The device consists of two vertical channels connected by a horizontal channel. Recalcified citrated whole blood is perfused through the right vertical channel and a wash buffer containing sodium citrated in perfused through the left vertical channel. The horizontal channel is coated with collagen peptides to promote platelet adhesion and tissue factor (TF) to initiate coagulation. A. The inlet pressures of the two vertical channels are set so that there is a pressure difference across the horizontal channel that drives the blood from the right vertical channel to the left vertical channel. B. After ~5 min a thrombus occluded the horizontal channel. C. After occlusion, tPA- μ wheels are introduced through the left vertical channel and directed to the interface of the thrombus where they penetrate into the thrombus and lyse the fibrin.121

Figure D.1: A) Local concentration of tPA and plasminogen 1 mm from the injection of a 50 nM bolus of tPA and 1 μ M plasminogen. B) Local concentration of tPA and plasminogen 1mm from the injection of $10^5/\mu$ L tPA-beads. C) Local concentration of tPA and plasminogen 1mm from the injection of $10^5/\mu$ L tPA-beads and $10^6/\mu$ L pgn-mMSN. D) Local concentration of tPA and plasminogen 1 mm from the injection of $10^5/\mu$ Lpgn-tPA-beads.122

Figure D.2: Schematic of microfluidic device used for fibrinolysis experiments.123

LIST OF TABLES

Table 1.1: Clinical studies using microbubble-assisted sonothrombolysis.	13
Table 1.2: Summary of preclinical studies for MNP targeting and actuation.	18
Table 1.3: Summary of approaches to engineered fibrinolytic macromolecules and particles	20

ACKNOWLEDGEMENTS

I owe almost everything to Drs. Dave W. M. Marr and Keith B. Neeves. Their positive influence will continue to shape my life for decades to come.

I also have a considerable debt to my parents, Dave Wasson, the Vicary-Rzab clan, Brianna Sauerland, Harrison Dunbar and the Seesters, all of whom contributed to my education in those all-important ways that are difficult to measure.

Dr. Dendy Sloan has been a mentor and a friend to me for the past decade. He taught me the power of curiosity, and for that I shall forever be grateful.

Special thanks are due to David Goggin, Tao Yang and Coy Zimmermann. Their friendship and intellect made all the difference day by day.

CHAPTER 1

ENGINEERED MICRO- AND NANOPARTICLES FOR FIBRINOLYSIS

This chapter is adapted with permission from

*Journal of Thrombosis and Haemostasis*¹

Dante Disharoon², David W.M. Marr³, and Keith B. Neeves⁴

1.1 Summary

Fibrinolytic agents including plasmin and plasminogen activators improve outcomes in acute ischemic stroke and thrombosis by recanalizing occluded vessels. In the decades since their introduction into clinical practice, several limitations have been identified both in terms of efficacy and bleeding risk associated with these agents. Engineered nano- and microparticles address some of these limitations by improving circulation time, reducing inhibition and degradation in circulation, accelerating recanalization, improving targeting to thrombotic occlusions, and reducing off-target effects. This review covers four advances in coupling fibrinolytic agents with engineered particles; (1) modifications of plasminogen activators with macromolecules, (2) encapsulation of plasminogen activators and plasmin in polymer and liposomal particles, (3) triggered release of encapsulated fibrinolytic agents and mechanical disruption of clots with ultrasound, and (4) enhancing targeting with magnetic particles and magnetic fields. Technical challenges for the translation of these approaches to the clinic are discussed.

¹ Reprinted with permission from: Disharoon D, Marr DWM, Neeves KB. Engineered microparticles and nanoparticles for fibrinolysis. *J Thromb Haemost* 2019; **17**: 2004–15. Copyright 2019, John Wiley & Sons, Inc.

² Primary author, Colorado School of Mines

³ Colorado School of Mines

⁴ Colorado School of Mines, University of Colorado School of Medicine

1.2 Introduction

Plasminogen activators (PA) were introduced into clinical practice in the 1980s primarily for indications of ischemic stroke and myocardial infarction [1]. Large clinical trials show the benefits of recombinant tissue plasminogen activator (tPA) in acute ischemic stroke [2,3]. During the last 30 years of clinical practice several limitations have arisen including a limited time window (4.5-6 hrs from onset of symptoms), neurotoxicity, and bleeding [4,5]. Over this same time, mechanical thrombectomy devices have emerged as an effective treatment for many types of occlusions in large arteries and veins [6–8]. In some cases, the combination of fibrinolytics and mechanical thrombectomy have been used successfully [9,10]. However, their use is limited to stroke centers that are not always available to individuals outside of major urban areas. Furthermore, mechanical thrombectomy devices cannot reach all types of clots. For example, in the brain, these devices cannot reach the M3/M4 branches where many strokes occur. Taken together, these considerations motivate the need for alternative drug delivery strategies for fibrinolytic agents.

The principle of fibrinolytic therapy is to deliver plasmin or PA to an occlusion to lyse fibrin, thus robbing the thrombus of its mechanical stability, and restoring blood flow in the vessel [11]. Plasmin binds directly to and lyses fibrin, however its efficacy is limited by rapid binding to its endogenous inhibitor α -antiplasmin. PA such as tPA, urokinase plasminogen activator (uPA), and streptokinase (SK) act indirectly by first cleaving plasminogen to plasmin. Intravenous (IV) delivery provides an elevated systemic concentration of these fibrinolytic agents. PA are more effective in IV delivery than plasmin because their endogenous inhibitors, plasminogen activator inhibitor 1 (PAI-1) and 2 (PAI-2), are found at lower plasma concentrations compared to α -antiplasmin. Alternatively, local delivery to occluded vessels

accessible to catheters can overcome some of the effects of these inhibitors with a high local concentration of plasmin or PA.

The most cited complication of fibrinolytic therapy is the risk for iatrogenic bleeding since these agents degrade hemostatic as well as thrombotic clots [12,13]. PA cause bleeding in a small fraction (1-6%) of patients when used to treat ischemic stroke [12], pulmonary embolism [14], or myocardial infarction [15]. Furthermore, IV delivery of PA has a high incidence of failure for certain types of clots because it relies on blood flow, which is restricted or non-existent, to deliver them to the thrombus location [16]. Fibrinolytic therapy can also fail if a patient has high levels of PAI-1 [17] or SK antibody [18], or if the rate of deactivation exceeds the rate of delivery to the clot [19,20]. These limitations have prompted researchers to modify plasminogen activators (PA) with macromolecules to protect them from clearance and degradation in blood, thereby improving circulation half-life [21,22]. Further modifications of PA facilitate thrombus targeting via functionalization with moieties that bind to activated platelets or fibrin [23].

Nano- and microparticle carriers for PA have been developed to improve circulation time, reduce inhibition and degradation, and target occlusive thrombi [24,25]. Many of these are polymeric or liposomal spheres that encapsulate or embed PA. In addition to improving half-life and preventing loss of activity in circulation, these particles can be engineered to release PA at a controlled and prolonged rate [24]. Encapsulation allows delivery not only of PA, but also of plasmin itself by protecting it from inhibition by α 2-antiplasmin [26]. Other novel fibrinolytic carriers include PA-functionalized red blood cells with prophylactic effects on thrombosis [27], nanoclusters that release PA in response to increased shear stress in stenosed vessels [28], and activated platelet-stimulated liposomes that release their PA cargo [29].

Though such approaches offer improvements, designing PA carriers that selectively target occlusive thrombi without causing bleeding or reaching small vessels remains a challenge and motivates the need for carriers that can be actuated using an external control mechanism. For example, echogenic liposomes only release a PA payload when exposed to ultrasound [30]. Similarly, magnetically responsive liposomes, microbubbles, and micro- and nanoparticles can be driven to accumulate at the thrombus site using external magnetic fields. In this review, we highlight engineered micro- and nanoparticle PA carriers with special attention to particles externally actuated by ultrasound or magnetic fields.

1.3 Macromolecule modification of plasminogen activators

PA coupling to macromolecules can improve circulation time and protect against endogenous inhibitors (Fig. 1.1). One of the first examples of this approach was coupling streptokinase (SK) to polyethylene glycol (PEG), a process called PEGylation, which reduces α_2 -macroglobulin mediated catabolism of SK-plasmin complexes by 50% and extends its half-life from 5 min to 30 min [31]. Additionally, PEGylated SK binding to SK antibodies is reduced by 95%, indicating that this modification reduces the potential immunogenic response to SK [19]. Sakuragawa et al. PEGylated urokinase plasminogen activator (uPA) and showed extended activity over a 6 hr period, compared to a 1 hr period for native uPA, and 6-fold higher antithrombotic capabilities for PEGylated uPA compared to native uPA [32]. Berger and Pizzo showed that PEGylated tPA circulates for ten times longer in mice, rats, and beagles than tPA, though the active half-life is only increased threefold because of inhibition by PAI-1 and PAI-2 [33]. In all of these reports, the fibrinolytic rate of the PEGylated PA is slightly accelerated compared to the non-PEGylated control, likely due to reduced inhibition.

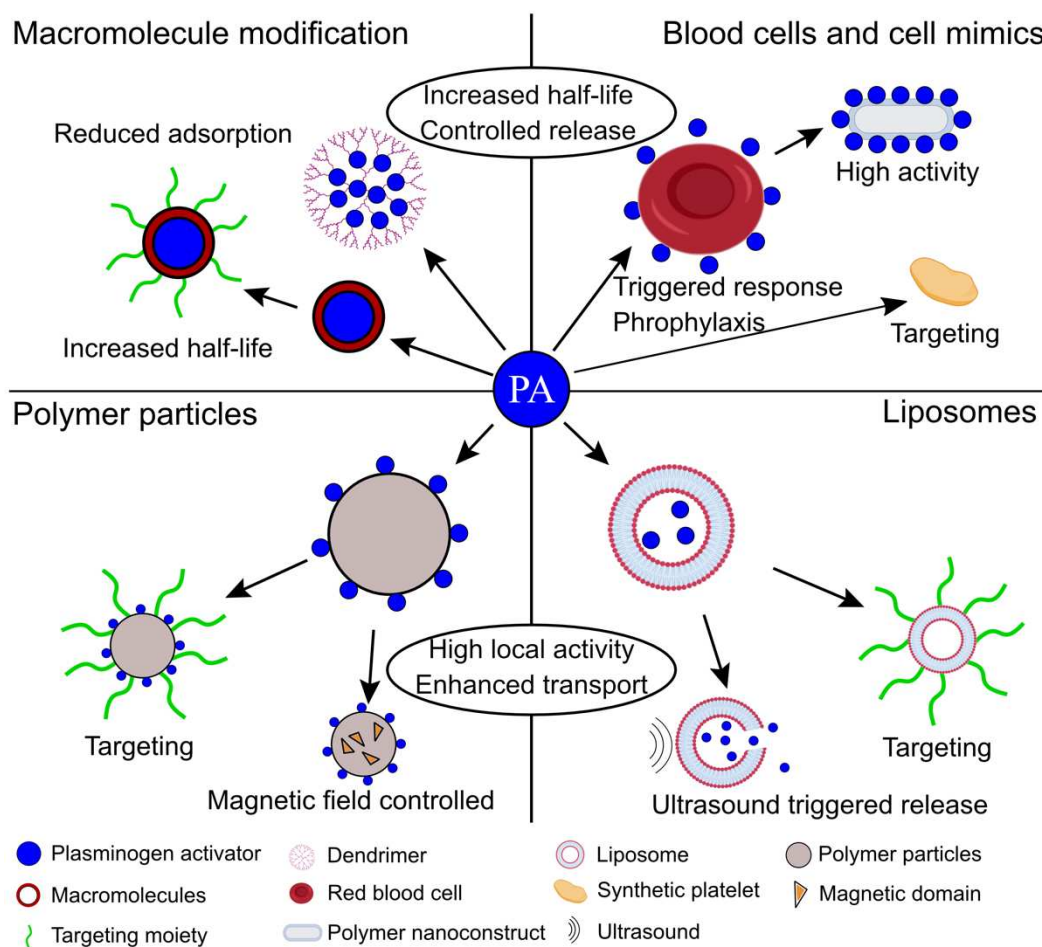


Figure 1.1: Overview of engineered particles for fibrinolysis covered in this review with features of different materials, targeting strategies, and actuation.

Beyond PEGylation, tPA has been coupled to albumin via a thrombin cleavable peptide [34]. The activity of the albumin coupled tPA is reduced by 25% but, upon exposure to thrombin, regains activity to 90% of the uncoupled tPA control. Additionally, circulation time is increased to 24 hr with a concentrated burst lasting 30 minutes after exposure to thrombin, and fibrinogenolysis is reduced by half. Another method of improving circulation time is embedding PA into branched synthetic polymers called dendrimers. Wang et al. embedded SK within a poly(amido amine) dendrimer and showed that it retained 80% of its activity and was stable in buffer for three-fold longer than free SK [35]. Fibrinolysis rates were nearly identical for the PA

dendrimer and free SK. Other studies using SK in dendrimers report slightly enhanced lysis rates [36] and reduced fibrinogen degradation [37].

Other macromolecule modifications focus on coupling PA to macromolecules that target activated platelets, activated endothelial cells, or fibrin [22]. Bode et al. conjugated uPA to a monoclonal antibody to the integrin $\alpha_{IIb}\beta_3$ on platelets [38]. They found that anti- $\alpha_{IIb}\beta_3$ antibody modified uPA was drastically better at lysing platelet-rich clots in platelet density dependent manner. Similarly, targeting $\alpha_{IIb}\beta_3$ with a peptide attached to staphylokinase (SAK) improved fibrinolysis as well as decreased platelet aggregation relative to SAK without the peptide [39]. For a more detailed review of approaches for targeting platelets, endothelial cells, fibrin and erythrocytes, we refer the reader to the excellent review by Absar et al. [23].

1.4 Encapsulation of plasminogen activators in liposomes and polymer particles

An alternative way to prevent PA degradation and inhibition in circulation is to encapsulate them within lipid vesicles, liposomes, or polymer matrices (Fig. 1.1). SK encapsulated in unilamellar phosphatidylcholine liposomes retains 100% of its activity after 30 min incubation in plasma while unencapsulated SK loses more than 50% of its activity [40]. Stability tests indicate that liposomes do not leak SK over a period of 24 hours at body temperature. They release SK through membrane pores during interaction with a thrombus, resulting in similar lysis rates to unencapsulated SK. In another study, tPA encapsulated in poly-(lactide-*co*-glycolide) (PLGA) nanoparticles coated with the polysaccharide chitosan reduces tPA degradation while reducing lysis time of in vitro whole blood clots by 40% [41]. Both liposome and PEG encapsulated SK outperform free SK in thrombi formed in the carotid artery of rabbits; reperfusion was achieved in 75 min for free SK, 19 min for liposomal SK, and 7 min for PEG encapsulated SK [42]. Similarly, SK encapsulation in distearolphosphatidylcholine with

PEG in the lipid bilayer increases half-life by 16-fold and activity by 6-fold in rats [43]. Such encapsulated PA are more effective, in part, because they display reduced adsorption to fibrin front relative to non-encapsulated PA, and instead support penetration of PA into the thrombus [42].

To mitigate off-target fibrinolysis, micro- and nanoparticles carrying PA have also been decorated with targeting molecules. Huang et al. modified tPA carrying liposomes with PEG and cyclic arginine-glycine-aspartic acid (cRGD), which is found on the γ chains of fibrin and binds to activated $\alpha_{IIb}\beta_3$ [29]. The cRGD supports fusion between the liposomes and activated platelets, causing the liposomes to destabilize and release 90% of their tPA payload within 1 hr of interaction. Liposomes without cRGD motifs or those not exposed to activated platelets only release 10% of their tPA after 6 hr, indicating that tPA release is platelet-sensitive and targeted. Thrombolytic efficiency of the cRGD coated tPA-liposomes is equivalent to free tPA and three-fold faster than liposomes not triggered by platelets using cRGD. While there is no enhancement to lysis rate over the soluble drug, there are three advantages of cRGD PEGylated liposomes. First, liposomal encapsulation of tPA protects the drug from degradation in plasma. Second, PEGylation of tPA-liposomes make them less susceptible to unwanted destabilization. Finally, the cRGD motifs ensure that large payloads of tPA are only released in the presence of activated platelets, preventing systemic action of tPA.

Another approach is to target the biophysical environment of thrombosis. Korin et al. fabricated shear-activated nanotherapeutics (SA-NT) where 1-5 μm aggregates of nanoparticle were produced by drying concentrated solutions of PLGA nanoparticles carrying immobilized tPA. [28]. These aggregates are stable up to shear stresses of $\sim 100 \text{ dyn/cm}^2$ and disassemble into their constituent nanoparticles at higher shear stresses, such as those experienced in stenotic or

obstructed vessels. In a microfluidic model of stenosis with peak shear stress of 450 dyn/cm², sixteen-fold more nanoparticles released from the SA-NT than in the straight part of the channel with shear stress of 30 dyn/cm². Thrombi were lysed within 5 min of SA-NT administration in the ferric chloride thrombosis model in murine mesenteric arteries. This approach also shows promise as a prophylactic antithrombotic as pre-circulating SA-NT delayed time to full occlusion three-fold relative to control mice. In a murine pulmonary embolism model, the SA-NT conferred a survival advantage; 100% of control mice died while 80% of mice receiving SA-NT survived the embolism with >60% reperfusion after 45 min. Another advantage of SA-NT is that tPA-nanoparticles selectively concentrate near occlusions in regions of high shear stress, potentially reducing off-target side effects.

1.5 Coupling plasminogen activators to blood cells and blood cell mimics

Another targeting and triggered-release strategy relies on imitating or hijacking platelets or red blood cells (RBC) (Fig. 1.1). Pawlowski et al. designed platelet microparticle-inspired nanovesicles (PMIN) carrying SK that interact with platelets via ligands for $\alpha_{IIb}\beta_3$ and P-selectin [44]. Once the PMIN interacted with platelets, phospholipase-A₂, an enzyme that is upregulated in sclerotic arteries [45], destabilizes the PMIN and triggers release of SK. In the ferric chloride thrombosis model in the murine carotid artery the SK-PMIN had antithrombotic properties indistinguishable from an equal dose of free SK. In a murine tail bleeding model the bleeding times for mice treated with SK-PMIN is equivalent to those for untreated controls, while bleeding times for mice receiving free SK was three-fold higher [44]. Unlike free SK, these SK-PMIN do not initiate systemic fibrinogenolysis.

PA can be bound directly to blood cells as a targeted therapeutic strategy. For example, tPA has been coupled to biotinylated red blood cells (RBC) [46]. In the ferric chloride

thrombosis model of the murine carotid artery, tPA-RBC restored blood flow in 20-30 min, where unbound tPA failed to reperfuse the vessel. tPA-RBC were also combined with traditional PA delivery to accelerate fibrinolysis by creating large (>20 μm) pores within the thrombus to promote tPA penetration [47]. These tPA-RBC are an example of antithrombotic particles that are entrained in thrombi during their formation and either initiate or enhance fibrinolysis. Prophylaxis however requires particles to be present in the blood prior to an unpredictable event and therefore are likely most useful in individuals at high risk for thrombosis. See Greineder et al. for further discussion of antithrombotic drug delivery approaches [22].

Rather than using blood cells, Colasuonno et al. synthesized discoidal polymeric nanoconstructs (DPN) mimetics shaped like RBC and functionalized with tPA (tPA-DPN) [48]. DPN are 1 μm in diameter, 0.4 μm in height, biconcave, and can be synthesized from either PEG or PLGA. tPA-DPN have a fibrinolytic efficiency roughly 50% higher than free tPA at 10% the free tPA concentration. In thrombi formed in the the ferric chloride thrombosis model in murine mesentery venules, 0.1 mg/kg of tPA-DPN recanalizes 70% of thrombi in under 60 min, whereas 1 mg/kg of free tPA only recanalizes 40% thrombi after 90 min. Importantly, tPA associated to DPN is also protected from degradation by PAI-1 for longer than 3 hr in plasma, where free tPA is degraded to 30% activity.

Synthetic platelets have been developed as hemostats [49–52], but also for thrombolysis [53], where cross-linked actin layers are grown on a discoidal polymer core. Upon removal of the core, the remaining protein structure retains the size, shape and flexibility of platelets and are functionalized with the A1 domain of von Willebrand factor or the amino terminal domain of GPIIb α to bind to platelet-rich thrombi. Thrombi formed in ex vivo whole blood perfusion over collagen with at concentrations of $1.5\text{-}4\times 10^5$ particles/ μL comprised between 40-80% of the

thrombus, while spheres functionalized with the same moieties only comprised between 5% and 10% of the volume. These data indicate that both physical and biochemical properties can be exploited to enhance thrombus targeting, and SP functionalized with PA could be a potent targeted thrombolytic.

1.6 Ultrasound mediated lysis and release

1.6.1 Echogenic Liposomes

Instead of relying on systemic circulation, biochemical targeting, or blood flow induced mechanical forces to achieve local thrombolysis, external forces can trigger the release of encapsulated tPA from liposomes (Fig. 1.1, Fig. 1.2A). Echogenic liposomes (ELIP) release payloads on demand with application of sonic forces [54]. Shaw et al. used thrombi formed from whole blood *ex vivo* to test ELIP containing tPA (tPA-ELIP) with 120 kHz ultrasound. tPA-ELIP in the presence of ultrasound lysed thrombi four-fold faster than tPA alone [55]. The efficacy of tPA-ELIP was also shown in a murine model of thrombosis that uses denudation of the aorta followed by injection of 5% sodium ricinoleate and thrombin [56]. Blood flow was restored twice as fast by tPA-ELIP than empty ELIP in the presence of tPA and ultrasound at 5.7 MHz, and tPA-ELIP in the presence of ultrasound was twice as fast compared to no ultrasound. ELIP has also been used to deliver plasmin [26]. Kandadai et al. used plasmin-loaded ELIP to lyse blood clots formed from human whole blood *in vitro*, and reported that plasmin-ELIP exposed to 120 kHz ultrasound with 1.7 MHz pulses lysed clots at 15% faster rates than free tPA.

1.6.2 Sonothrombolysis

Sonothrombolysis refers to methods using sonic energy to directly or indirectly degrade thrombi. For the interested reader, Bader et al. reviews the mechanisms of sonothrombolysis

[30]. Here we focus on micro- and nanoparticles that enhance the efficiency of these mechanisms; acoustic streaming, cavitation, and ultrasound-induced temperature rise. Acoustic streaming describes the use of acoustic radiation forces to create flow, which at the site of a thrombus helps overcome the slow, diffusion-mediated transport of PA in occluded vessels (Fig. 1.2B) [57]. Cavitation directly degrades thrombi with mechanical energy from bubble formation, oscillation, and collapse (Fig. 1.2C) [58]. Ultrasound can cause local temperature to increase by up to 5 °C and thereby accelerate fibrinolysis; however, when the contributions of each mechanism are decoupled, acoustic streaming and cavitation contribute more significantly to fibrinolytic enhancements than heating directly [59].

Sonothrombolysis is enhanced in the presence of microbubbles (Fig. 1.2D), gas-filled vesicles typically less than 8 μm in diameter [60]. Microbubbles are used as an ultrasound contrast agent because they scatter sonic waves more than blood, but they have recently garnered attention as agents for drug delivery and gene therapy [60]. Microbubbles can be stabilized with silanes, surfactants, protein shells, polymer coatings, or lipids. Bader et al. investigated the mechanism for microbubble-assisted sonothrombolysis using 50 μm octofluoropropane bubbles stabilized with a lipid monolayer [61]. They concluded that the oscillations and coalescence of microbubbles with a resonant frequency close to the frequency of ultrasound exposure were the primary contributors to lysis during exposure to sonic forces. They also observed more sustained cavitation over 50 s periods in the presence of microbubbles which further contributes to enhanced thrombolysis.

A series of clinical trials show the potential for sonothrombolysis in treatment of ischemic stroke of major cerebral arteries (Table 1.1). One trial found that ultrasound therapy in the presence microbubbles reduced reperfusion times to less than 20 min, while achieving full

recanalization in 71% of patients within 2 hr [62]. By comparison, full recanalization was achieved in only 39% of patients receiving just tPA. There was no increased risk of intracranial hemorrhage due to the microbubbles compared to patients receiving only tPA. In another trial, sonothrombolysis accelerated reperfusion but increased risk of hemorrhage [63]. Out of 35 patients, risk of intracerebral hemorrhage was directly related to the dosage of microbubble infusion. Patients receiving a 1.4 mL dose of microspheres over a 90 min period experienced recanalization in half the time of control patients and did not experience an increase in hemorrhagic events; however, 27% of patients who received a double dose of microspheres experienced hemorrhage without a decrease in reperfusion time. A similar study validated these results [64]. The data from these studies indicate that the effects of microbubble size, composition, viscoelasticity and ultrasound frequency on microbubble-assisted sonothrombolysis merit further investigation.

1.7 Magnetic particles and magnetic field control

1.7.1 Synthesis and functionalization of magnetic nanoparticles carriers

Ultrasound waves attenuate in tissues, and thrombolytic methods that use ultrasound may be ineffective in vessels away from the body's surface or not easily accessible by surgical intervention. Moreover, both ultrasound mediated drug release and microbubble enhanced sonothrombolysis rely on local catheter delivery or circulation to bring particles near a thrombus. This could be challenging for occlusions in small vessels where catheters cannot reach. Magnetic fields overcome these limitations as they do not attenuate in tissue for frequencies <30 Mhz [65]. They can also be used to concentrate PA-laden magnetic particles at the thrombus periphery [66]. Magnetic nanoparticles (MNP) used for fibrinolysis are made from <30 nm superparamagnetic iron oxide crystals of magnetite (Fe_3O_4) or maghemite ($\gamma\text{-Fe}_2\text{O}_3$), FDA

approved materials [67,68] with low toxicity in humans [69], embedded in a polymer matrix [67]. The small, randomly distributed domains allow the MNP to orient themselves in the direction of a magnetic field at all times with an induced dipole.

Table 1.1: Clinical studies using microbubble-assisted sonothrombolysis.

Vessel	Number of patients	Initial NIHSS score (Range)	3-month favorable outcome	Ultrasound frequency	Gas	Microbubble size	Microbubble stabilizing agent	Ref.
MCA	15	17 (6-28)	40%	2 MHz	C ₃ F ₈	1-2 μ m	Lipids	[64]
MCA	111	18 (15-19)	56%	2 MHz	Air	2-8 μ m	Galactose	[62]
MCA, ACA or PCA	35	18 (9-21)	72%	2 MHz	C ₃ F ₈	1-2 μ m	Lipids	[63]
MCA	138	17 (12-20)	46%	300 kHz	Air or SF ₆	2-8 μ m (air) or 1.5-4.5 μ m	Galactose (air) or Lipids	[91]

National Institute of Health Stroke Scale (NIHSS) rates the severity of an occlusion. A higher score indicates a more severe clot with NIHSS > 4 requiring treatment. A 3-month favorable outcome is characterized by a decrease in the NIHSS score to 0-3. MCA, middle cerebral artery; ACA, anterior cerebral artery; PCA, posterior cerebral artery.

As in other fibrinolytic particles discussed above, encapsulating or immobilizing PA on MNP increases enzyme stability during storage [70] and improves half-life [71]. MNP carrying tPA, uPA, or SK have been decorated with coatings that further improve half-life and reduce immunogenicity including dextran [72,73], chitosan [74], silica [71,75], hydrosol [76], PLGA and PLA-PEG [77], polyacrylic acid (PAA) [78], polyethylene glycol (PEG) [79,80], poly[aniline-co-N-(1-one-butyrac acid) aniline] [70], and heparin [81]. PA functionalization of MNP can rely on either physical adsorption to the MNP matrix or covalent attachment [82].

Adsorption yields high concentrations of tPA ($> 20 \mu\text{g/mL}$) near a thrombus [77]; however, PA desorb from PLGA, PAA, and uncoated magnetite rods within 30 min of injection [77,82,83].

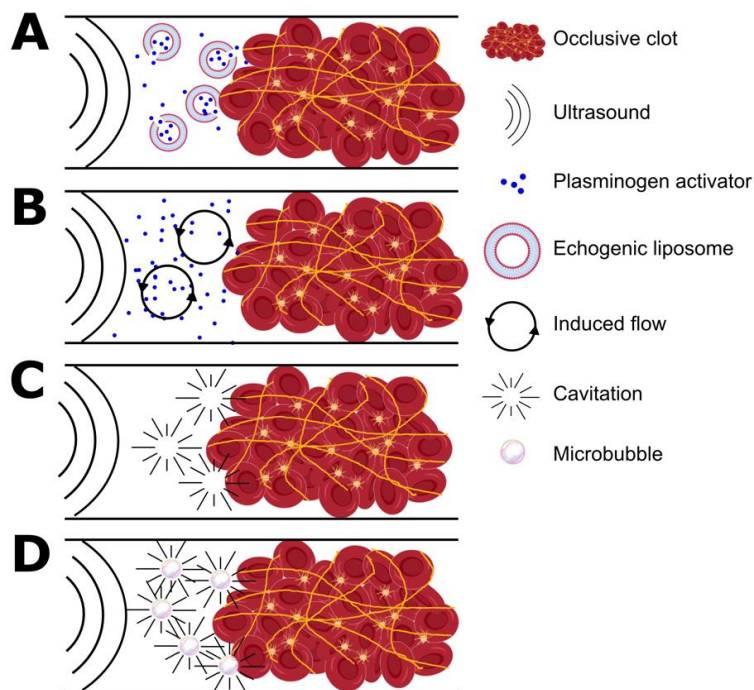


Figure 1.2: Mechanisms of assisting thrombolysis using ultrasound. A) Ultrasound forces cause ELIP to deliver a payload of PA near a thrombus. B) Sonic forces cause acoustic streaming that induces flow and improves transport of PA to a thrombus. C) Sonic forces cause cavitation, which imparts mechanical energy into the thrombus and initiates degradation even in the absence of PA. D) Microbubbles increase the frequency of cavitation and accelerate lysis. See Table 1.1 for details and references.

Premature release of PA before particles reach their target is problematic and compounded by the short half-life (5 min) of recombinant tPA in blood [84]. Limitations related to timing of PA release motivate the need for magnetic carriers with triggered release and alternative functionalization methods. Drozdov et al. developed a magnetite composite material that incorporates uPA that does not leach, enabling magnetically responsive drug carriers to have prolonged activity for several hours [76]. In this, negatively charged plasminogen interacts with a positively charged particle matrix containing uPA. Once converted, positively charged plasmin is repelled out of the MNP. A covalent bonding strategy is functionalization of PAA particle

surfaces using N-hydroxysuccinimide followed by coupling with tPA [82]. Alternatively, streptavidin-functionalized particles can be conjugated to biotinylated tPA [66]. Such immobilization of PA protects the enzyme from inhibition by PAI-1 and degradation in the liver.

1.7.2 Magnetic field control of magnetic particles

The simplest form of magnetic control is to use a permanent magnet to establish a magnetic field gradient to move MNP towards a target (Fig. 1.3A, Table 1.2). This is the most widely reported method for manipulating PA carriers [71,73,79,80,83]. Ma et al. used PAA particles conjugated with tPA to show recanalization of the iliac artery in rats and demonstrated reperfusion using only 20% of the therapeutic tPA concentration (1 mg/kg) [78]. Experiments in rat and mouse models also use a moving permanent magnet to drag MPN from the drug injection site to the thrombus [12,14,19]. Magnetic field gradients are difficult to scale to humans as the strength of a magnetic gradient force decays with the inverse square of the distance ($1/r^2$) from the magnet. As an example, a 1.5 T magnet is capable of creating a 40 mT/m gradient in the carotid artery of pigs, which is sufficient to propel a 1.5 mm sphere at a velocity of 13 mm/s, but a 5 μ m sphere only 1 μ m/s [38]. The tortuosity of the human vasculature also renders a unidirectional field gradient potentially ineffective as MPN must navigate through vessels in varying orientations.

Magnetic field induced mixing can enhance fibrinolysis by free PA (Fig. 1.3B, Table 1.2). Torno et al. used a permanent magnet to move magnetic microspheres back and forth, inducing a flow field near a bolus of tPA [85]. Mixing doubled the thrombolytic efficiency by reducing concentration gradients and, when combined with 20 kHz ultrasound, accelerated lysis three-fold over no mixing or ultrasound. A similar mixing strategy was reported by Huang et al. where rotating permanent magnets made rod-shaped particles spin [86]. In an embolic rat model,

they reported that mixing doubled tPA-mediated lysis. Khalil showed thrombi removal using a ~1 mm helical robot made to abrade a thrombus via external magnetic control [87]. This purely mechanical mechanism removed a clot at three times the rate of the clinical dose of SK and may provide a less invasive alternative to catheters. MNP can also be heated with applied magnetic fields. For example, Voros et al. immobilized tPA on nanocubes, particles with cubic rather than spherical geometry, and subjected them to 500 kHz radio frequency (RF) fields to locally raise the temperature to 42 °C (Fig. 1.3C) [88]. Here, fibrin dissolution occurred an order-of-magnitude faster at 42 °C compared to 37 °C in vitro. In a ferric chloride thrombosis model in murine mesentery vessels, tPA nanocubes lysed clots in <1 min compared to 5-10 minutes in the absence of heating. This enhancement is greater than predicted based on the temperature-dependence of lysis kinetics and is also attributed to faster tPA release from the nanocubes [88].

Some of the most novel MNP strategies initiate thrombolysis through both chemical and mechanical mechanisms (Table 1.2). De Saint Victor et al. made 0.2-15 µm microbubbles containing air and 10 nm magnetite particles stabilized by phospholipids [89]. The mechanical energy from ultrasound cavitation combined with the biochemical action of free tPA degraded whole blood thrombi 2.5-fold faster than free tPA alone. Magnetic targeting provided further enhancement; retention of a high local concentration of magnetic microbubbles using a permanent magnet resulted in a continuous supply of high cavitation energy. The cavitation energy was itself enhanced by a large concentration of microbubbles resulting from magnetic focusing. This magnetically mediated sonothrombolysis degraded clots roughly twenty-fold faster than soluble tPA alone, ten-fold faster than ultrasound alone, and four-fold faster than tPA and ultrasound in the presence of microbubbles but in the absence of magnetic focusing.

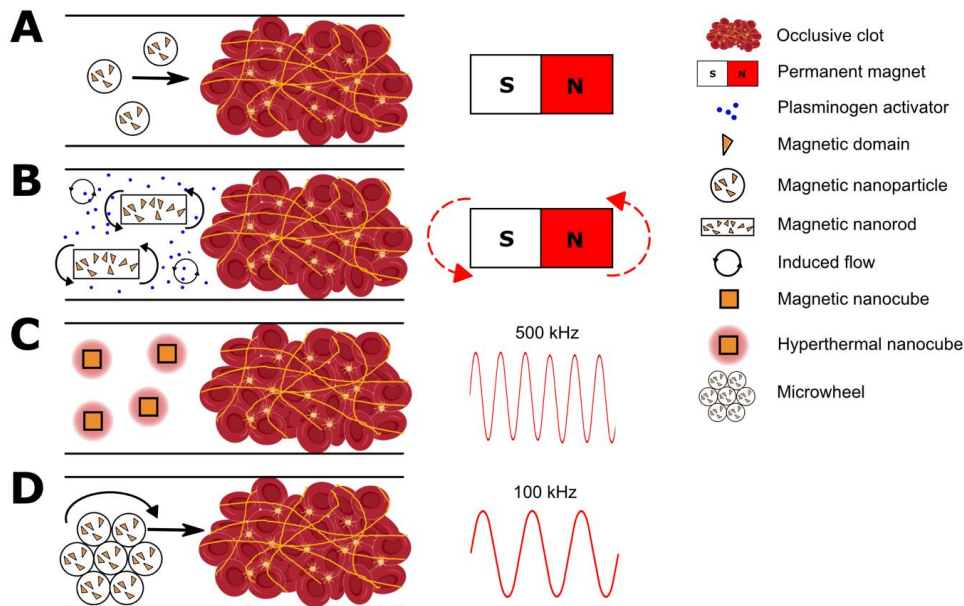


Figure 1.3: Methods of magnetic control of magnetic nanoparticles (MNP). A) MNP move down a magnetic field gradient toward a clot using a permanent magnet. B) A rotating magnet is used to rotate rod-like MNP, inducing convection and improving transport of PA to a clot. C) A high frequency magnetic field induces local heating of cube-like MNP. D) A low frequency rotating magnetic field causes MNP to assemble into microwheels and roll into a thrombus. See Table 1.2 for details and references.

Tasci and Disharoon et al. demonstrated enhanced fibrinolysis using a combination of biochemical and mechanical action using magnetically powered microwheels assembled in situ [66]. Biotinylated tPA was immobilized on 1 μm streptavidin-coated MNP. The microwheels rolled to the interface of a plasma clot (Fig. 1.3D) and accumulated tPA at this interface at a concentration 50 times higher than the injected concentration. Once at the interface, a corkscrew-like motion was used to drive the microwheels into the clot yielding a lysis rate six-fold faster than tPA alone. This approach relies on low strength (~ 10 mT), rotating magnetic fields rather than field gradients which is easier to scale-up to humans. The microwheels assemble to structures greater than 10 μm in diameter, which is within the detection limits of MRI [90], but disassemble into 1 μm spheres upon removal of the magnetic field, making them passable through capillaries.

Table 1.2: Summary of preclinical studies for MNP targeting and actuation.

PA	Particle matrix	Magnetism	Iron oxide loading	Magnetic guidance	Type of experiment	Lysis rate relative to soluble PA	Ref.
tPA	PLGA	SP	5 wt%	None	None	Not Compared	[77]
uPA	PEG	P	0.54 wt%	PM	In vitro	1.8	[79]
uPA	PEG	P	2 wt%	PM	In vitro	3.7	[80]
tPA	PLA-PEG	SP	Unmedicated	Translating PM	In vitro	2.7	[85]
tPA	Silica	SP	9.4 wt%	PM	In vitro	1.7	[75]
tPA-SK	Silica	SP	0.2 mg/mL	PM	In vitro	2.2	[71]
uPA	Hydrosol	SP	1 wt%	PM	In vitro	3.0	[76]
tPA	None	SP	6 wt%	Rotating PM	In vitro	1.4	[83]
tPA	Dextran	SP	0.25 mg/mL	PM	In vitro	Not Compared	[73]
tPA	PAA	SP	8 wt%	Translating PM	Rat, iliac artery embolism	>1.6	[78]
uPA	Dextran	SP	20000 IU/mL	PM	Rat, arteriovenous shunt	5.0	[72]
tPA	Chitosan	SP	9.5 wt %	Translating PM	Rat, iliac artery embolism	2.1	[74]
tPA	Poly aniline	SP	27.6 wt%	PM	Rat, iliac artery embolism	6.5	[70]
uPA	Heparin	SP	8 wt%	PM	Rat and rabbit, carotid	20.8	[81]
tPA	Ferrolipids	SP	Unmedicated	PM	In vitro	~20	[89]
tPA	Aluminum	M	Unmedicated	Rotating PM	In vitro	3.3	[87]
tPA	Nickel	P	Unmedicated	Rotating PM	In vitro	1.8	[86]
tPA	BSA	SP	~0.5 mg/mL	AC Field	Mouse, mesentery vasculature	~1000	[88]
tPA	Polystyrene	SP	3.6 ug/ mL	Helmholtz coils	In vitro	3.3	[66]

PA, plasminogen activator; PLGA, poly-(lactide-co-glycolic) acid; PEG, polyethylene glycol; PLA-PEG, poly(D,L-lactide)-co-poly(ethylene glycol); PAA, polyacrylic acid; BSA, bovine serum albumin; SP, superparamagnetic; P, paramagnetic; M, permanently magnetic; PM, permanent magnet; AC, alternating current.

1.8 Outlook

Table 1.3 provides a summary of the advantages and disadvantages of the different approaches to engineered fibrinolytic particles reviewed here. The external actuation of PA particles using ultrasound and magnetic fields is a promising direction, but several challenges must be overcome to translate these approaches into clinical practice. Ultrasound actuation has received positive results in small clinical trials but further characterization is needed on microbubble dosage [63], size, and composition, especially at lower frequencies [91]. Most studies of magnetic field actuation to date have been in preclinical models.

A promising feature of magnetic approaches is the ability to both localize and concentrate fibrinolytic particles near a thrombus, reducing the effective circulating concentration of PA, helping to minimize side effects, and potentially broadening the indications for PA therapy. The scale-up of the hardware required for magnetic control in humans will have to overcome several technical obstacles: (i) the generation of sufficient magnetic forces in deep tissues, (ii) particle navigation in the complex, three-dimensional vasculature, (iii) combining actuation with imaging, and (iv) achieving translation across or against flowing blood. Nonetheless, the development of fibrinolytic particles has produced encouraging results. Some of the most recent work has made it clear that combining PA encapsulation with magnetic localization, ultrasound, and hyperthermia may produce lysis rates up to an order-of-magnitude faster than those achievable using free PA. Engineered particles also allow for the delivery of two or more agents, which could be exploited to couple PA with other emerging thrombolytic targets including von Willebrand factor [92–94], neutrophil extracellular traps [95], and thrombin-activatable fibrinolysis inhibitor (TAFI) and PAI-1 [96].

Table 1.3: Summary of approaches to engineered fibrinolytic macromolecules and particles

Method	Advantages	Disadvantages
Macromolecules		
Polymer coatings	Increased half-life FDA approved materials available	Reduced activity Low specificity Low mobility in occluded vessels
Dendrimers	Increased half-life Reduced adsorption Variable loading	Low specificity Low mobility in occluded vessels
Modified blood cells and cell mimics		
Targeting	Targets components of thrombi Reduced bleeding risk	Low mobility in occluded vessels
Prophylaxis	Preventive Triggered release Degrades clot from inside out	Requires presence in blood before vessel occlusion Complicated preparation/synthesis
Shear-activated release	Reduced bleeding risk Triggered release	No shear in fully occluded vessel Requires presence in blood before vessel occlusion
Liposomes and polymer particles		
PA Encapsulation	Increased half-life Controlled release Reduces adsorption to fibrin	Low specificity Difficult to control stability Low mobility in occluded vessels
PA Immobilization	Increased half-life Decreased PA inhibition Increased clot penetration Used in other clinical applications	Reduced activity Low mobility in occluded vessels
Actuation		
Sonic actuation	Enhanced lysis Locally induced flows Successful phase II clinical trials	Limited mobility in occluded vessels Limited targeting/specificity
Magnetic actuation	Compatible with most engineered particles High mobility, targeting Local hyperthermia High local concentration	Early stages of development (preclinical) Challenging scale-up

1.9 References

- 1 Marder VJ. Historical perspective and future direction of thrombolysis research: The re-

- discovery of plasmin. *J Thromb Haemost* 2011; **9**: 364–73.
- 2 Sandercock P, Wardlaw JM, Lindley RI, Dennis M, Cohen G, Murray G, Innes K, Venables G, Czlonkowska A, Kobayashi A, Ricci S, Murray V, Berge E, Slot KB, Hankey GJ, Correia M, Peeters A, Matz K, Lyrer P, Gubitz G, et al. The benefits and harms of intravenous thrombolysis with recombinant tissue plasminogen activator within 6 h of acute ischaemic stroke (the third international stroke trial [IST-3]): A randomised controlled trial. *Lancet* Elsevier Ltd; 2012; **379**: 2352–63.
 - 3 Emberson J, Lees KR, Lyden P, Blackwell L, Albers G, Bluhmki E, Brott T, Cohen G, Davis S, Donnan G, Grotta J, Howard G, Kaste M, Koga M, Von Kummer R, Lansberg M, Lindley RI, Murray G, Olivot JM, Parsons M, et al. Effect of treatment delay, age, and stroke severity on the effects of intravenous thrombolysis with alteplase for acute ischaemic stroke: A meta-analysis of individual patient data from randomised trials. *Lancet* 2014; **384**: 1929–35.
 - 4 Levy DE, Brott TG, Haley EC, Marler JR, Sheppard GL, Barsan W, Broderick JP. Factors Related to Intracranial Hematoma Formation in Patients Receiving Tissue-Type Plasminogen Activator for Acute Ischemic Stroke. *Stroke* 1994; **25**: 291–7.
 - 5 Abu R, Nassar T, Yarovoi S, Rayan A, Lamensdorf I, Karakoveski M, Vadim P, Jammal M, Cines DB, Higazi AA. Neuropharmacology Blood e brain barrier permeability and tPA – mediated neurotoxicity. *Neuropharmacology* Elsevier Ltd; 2010; **58**: 972–80.
 - 6 Goyal M, Menon BK, Eesa M, Barber PA, Morrish WF, Demchuk AM, Kamal NR, Ryckborst KJ, Coutts SB, Smith EE, Subramaniam S, Mitha AP, Wong JH, Sajobi TT, Hill MD, Lowerison MW, Rempel JL, Shuaib A, Roy D, et al. Randomized assessment of rapid endovascular treatment of ischemic stroke. *N Engl J Med* 2015; **372**: 1019–30.
 - 7 Campbell BCV, Yassi N, Yan B, Oxley TJ, Wu TY, Davis SM, Mitchell PJ, Dowling RJ, Churilov L, Donnan GA, Kleinig TJ, Scroop R, Dewey HM, Brooks M, Simpson MA, Parsons MW, Miteff F, Levi CR, et al. Endovascular therapy for ischemic stroke with perfusion-imaging selection. *N Engl J Med* 2015; **372**: 1009–18.
 - 8 Tomasello A, Castaño C, Blasco J, Aja L, Dorado L. Thrombectomy within eight hours after symptom onset in ischemic stroke. *Turk Noroloji Derg* 2016; **22**: 36.
 - 9 Saver JL, Goyal M, Bonafe A, Diener H-C, Levy EI, Pereira VM, Albers GW, Cognard C, Cohen DJ, Hacke W, Jansen O, Jovin TG, Mattle HP, Nogueira RG, Siddiqui AH, Yavagal DR, Baxter BW, Devlin TG, Lopes DK, Reddy VK, et al. Stent-Retriever Thrombectomy after Intravenous t-PA vs. t-PA Alone in Stroke. *N Engl J Med* 2015; **372**: 2285–95.
 - 10 Campbell BCV, Mitchell PJ, Churilov L, Yassi N, Kleinig TJ, Dowling RJ, Yan B, Bush SJ, Dewey HM, Thijs V, Scroop R, Simpson M, Brooks M, Asadi H, Wu TY, Shah DG, Wijeratne T, Ang T, Miteff F, Levi CR, et al. Tenecteplase versus Alteplase before

- Thrombectomy for Ischemic Stroke. *N Engl J Med* 2018; **378**: 1573–82.
- 11 Cesarman-Maus G, Hajjar KA. Molecular mechanisms of fibrinolysis. *Br J Haematol* 2005; **129**: 307–21.
 - 12 Miller DJ, Simpson JR, Silver B. Safety of Thrombolysis in Acute Ischemic Stroke : A Review of Complications , Risk Factors , and Newer Technologies. 2011; **1**: 138–47.
 - 13 Van De Werf F, Barron H V., Armstrong PW, Granger CB, Beriali S, Barbash G, Pehrsson K, Verheugt FWA, Meyer J, Betriu A, Califf RM, Li X, Fox NL. Incidence and predictors of bleeding events after fibrinolytic therapy with fibrin-specific agents: A comparison of TNK-tPA and rt-PA. *Eur Heart J* 2001; **22**: 2253–61.
 - 14 Daley MJ, Murthy MS, Peterson EJ. Bleeding risk with systemic thrombolytic therapy for pulmonary embolism: Scope of the problem. *Ther Adv Drug Saf* 2015; **6**: 57–66.
 - 15 Bundhun PK, Janoo G, Chen M-H. Bleeding events associated with fibrinolytic therapy and primary percutaneous coronary intervention in patients with STEMI. *Medicine (Baltimore)* 2016; **95**: e3877.
 - 16 von Kummer R. Early Major Ischemic Changes on Computed Tomography Should Preclude Use of Tissue Plasminogen Activator. *Stroke* 2003; **34**: 820–1.
 - 17 Kim SH, Han SW, Kim EH, Kim DJ, Lee KY, Kim DI, Heo JH. Plasma Fibrinolysis Inhibitor Levels in Acute Stroke Patients with Thrombolysis Failure. *J Clin Neurol* 2009; **1**: 142.
 - 18 Lew AS, Neer T, Rodriguez L, Geft IL, Shah PK, Ganz W. Clinical failure of streptokinase due to an unsuspected high titer of antistreptokinase antibody. *J Am Coll Cardiol* 1984; **4**: 183–5.
 - 19 Rijken DC, Sakharov D V. Molecular transport during fibrin clot lysis. *Fibrinolysis and Proteolysis* 2000; **14**: 98–113.
 - 20 Blinc A, Francis CW. Transport Processes in Fibrinolysis and Fibrinolytic Therapy. *Thromb Haemost* 1996; **76**: 481–91.
 - 21 El-Sherbiny IM, Elkholi IE, Yacoub MH. Tissue plasminogen activator-based clot busting: Controlled delivery approaches. *Glob Cardiol Sci Pract* 2014; **2014**: 336–49.
 - 22 Greineder CF, Howard MD, Carnemolla R, Cines DB, Muzykantov VR. Review Article Advanced drug delivery systems for antithrombotic agents. *Blood J* 2016; **122**: 1565–76.
 - 23 Absar S, Gupta N, Nahar K, Ahsan F. Engineering of plasminogen activators for targeting to thrombus and heightening thrombolytic efficacy. *J Thromb Haemost* 2015; **13**: 1545–56.

- 24 Vaidya B, Agrawal GP, Vyas SP. Functionalized carriers for the improved delivery of plasminogen activators. *Int J Pharm Elsevier B.V.*; 2012; **424**: 1–11.
- 25 Liu S, Feng X, Jin R, Li G. HHS Public Access. 2018; **15**: 173–84.
- 26 Kandadai MA, Meunier JM, Hart K, Holland CK, Shaw GJ. Plasmin-Loaded Echogenic Liposomes for Ultrasound-Mediated Thrombolysis. *Transl Stroke Res* 2014; **6**: 78–87.
- 27 Ganguly K, Krasik T, Medinilla S, Bdeir K, Cines DB, Muzykantov VR, Murciano JC. Blood clearance and activity of erythrocyte-coupled fibrinolytics. *The Journal of pharmacology and experimental therapeutics*. 2005; **312**: 1106-13.
- 28 Korin N, Kanapathipillai M, Matthews BD, Crescente M, Brill A, Mammoto T, Ghosh K, Jurek S, Bencherif SA, Bhatta D, Coskun AU, Feldman CL, Wagner DD, Ingber DE. Shear-Activated Nanotherapeutics for Drug Targeting to Obstructed Blood Vessels. *Science (80-)* 2012; **337**: 738–42.
- 29 Huang Y, Yu L, Ren J, Gu B, Longstaff C, Hughes AD, Thom SA, Xu XY, Chen R. An activated-platelet-sensitive nanocarrier enables targeted delivery of tissue plasminogen activator for effective thrombolytic therapy. *J Control Release* 2019; **300**: 1–12.
- 30 Bader KB, Bouchoux G, Holland CK. Sonothrombolysis. *Adv Exp Med Biol*. 2016; **889**: 339-62.
- 31 Rajagopalan S, Gonias SL, Pizzo S V. A nonantigenic covalent streptokinase-polyethylene glycol complex with plasminogen activator function. *J Clin Invest* 1985; **75**: 413–9.
- 32 Sakuragawa N, Shimizu K, Kondo K, Kondo S, Niwa M. Studies on the effect of PEG-modified urokinase on coagulation-fibrinolysis using beagles. *Thromb Haemost* 1986; **41**: 627–35.
- 33 Berger Jr H, Pizzo S V. Preparation of Polyethylene Glycol-Tissue Plasminogen Activator Adducts That Retain Functional Activity: Characteristics and Behavior in Three Animal Species. *Blood* 1988; **71**: 1641–7.
- 34 Absar S, Kwon YM, Ahsan F. Bio-responsive delivery of tissue plasminogen activator for localized thrombolysis. *J Control Release Elsevier B.V.*; 2014; **177**: 42–50.
- 35 Wang X, Inapagolla R, Kannan S, Lieh-Lai M, Kannan RM. Synthesis, characterization, and in vitro activity of dendrimer- streptokinase conjugates. *Bioconjug Chem* 2007; **18**: 791–9.
- 36 Ramos Fernandes EG, Alencar De Queiroz AA, Abraham GA, San Román J. Antithrombogenic properties of bioconjugate streptokinase-polyglycerol dendrimers. *J*

- Mater Sci Mater Med* 2006; **17**: 105–11.
- 37 Mukhametova LI, Aisina RB, Zakharyan EM, Karakhanov EA, Gershkovich KB, Varfolomeyev SD. Thrombolytic and fibrinolytic properties of bioconjugate streptokinase-polyamidoamine dendrimers in vitro. *Thromb Res* 2017; **154**: 50–2.
 - 38 Bode C, Meinhardt G, Runge MS, Freitag M, Nordt T, Arens M, Newell JB, Kübler W, Haber E. Platelet-targeted fibrinolysis enhances clot lysis and inhibits platelet aggregation. *Circulation* 1991; **84**: 805–13.
 - 39 Chen H, Mo W, Zhang Y, Su H, Ma J, Yao R, Zhang S, Ge J, Song H. Functional properties of a novel mutant of staphylokinase with platelet-targeted fibrinolysis and antiplatelet aggregation activities. *Eur J Pharmacol* 2007; **566**: 137–44.
 - 40 Nguyen PD, O’Rear EA, Johnson AE, Lu R, Fung BM. Thrombolysis Using Liposomal-Encapsulated Streptokinase: An In Vitro Study. *Exp Biol Med* 1989; **192**: 261–9.
 - 41 Chung TW, Wang SS, Tsai WJ. Accelerating thrombolysis with chitosan-coated plasminogen activators encapsulated in poly-(lactide-co-glycolide) (PLGA) nanoparticles. *Biomaterials* 2008; **29**: 228–37.
 - 42 Leach JK, Patterson E, O’Rear EA. Improving thrombolysis with encapsulated plasminogen activators and clinical relevance to myocardial infarction and stroke. *Clin Hemorheol Microcirc* 2004; **30**: 225–8.
 - 43 Kim IS, Choi HG, Choi HS, Kim BK, Kim CK. Prolonged systemic delivery of streptokinase using liposome. *Arch Pharm Res* 1998; **21**: 248–52.
 - 44 Pawlowski CL, Li W, Sun M, Ravichandran K, Hickman DS, Kos C, Kaur G, Sen Gupta A. Platelet microparticle-inspired clot-responsive nanomedicine for targeted fibrinolysis. *Biomaterials Elsevier Ltd*; 2017; **128**: 94–108.
 - 45 Zalewski A, Macphee C. Role of lipoprotein-associated phospholipase A2 in atherosclerosis: Biology, epidemiology, and possible therapeutic target. *Arterioscler Thromb Vasc Biol* 2005; **25**: 923–31.
 - 46 Murciano JC, Medinilla S, Eslin D, Atochina E, Cines DB, Muzykantov VR. Prophylactic fibrinolysis through selective dissolution of nascent clots by tPA-carrying erythrocytes. *Nat Biotechnol* 2003; **21**: 891–6.
 - 47 Gersh KC, Zaitsev S, Cines DB, Muzykantov V, Weisel JW. Brief report Flow-dependent channel formation in clots by an erythrocyte-bound fibrinolytic agent. 2015; **117**: 4964–8.
 - 48 Colasuonno M, Palange AL, Aid R, Ferreira M, Mollica H, Palomba R, Emdin M, Del Sette M, Chauvierre C, Letourneur D, Decuzzi P. Erythrocyte-Inspired Discoidal Polymeric Nanoconstructs Carrying Tissue Plasminogen Activator for the Enhanced Lysis

- of Blood Clots. *ACS Nano* 2018; **12**: 12224–37.
- 49 Modery-Pawlowski CL, Tian LL, Ravikumar M, Wong TL, Gupta A Sen. In vitro and in vivo hemostatic capabilities of a functionally integrated platelet-mimetic liposomal nanoconstruct. *Biomaterials* Elsevier Ltd; 2013; **34**: 3031–41.
- 50 Bertram JP, Williams CA, Robinson R, Segal SS, Flynn NT, Lavik EB. Synthetic Platelets: Nanotechnology to Halt Bleeding. *Sci Transl Med* 2009; **1**: 11ra22.
- 51 Nandi S, Brown AC. Platelet-mimetic strategies for modulating the wound environment and inflammatory responses. *Exp Biol Med* 2016; **241**: 1138–48.
- 52 Brown AC, Stabenfeldt SE, Ahn B, Hannan RT, Dhada KS, Herman ES, Stefanelli V, Guzzetta N, Alexeev A, Lam WA, Lyon LA, Barker TH. Ultrasoft microgels displaying emergent platelet-like behaviours. *Nat Mater* 2014; **13**: 1108–14.
- 53 Doshi N, Orje JN, Molins B, Smith JW, Mitragorti S, Ruggeri ZM. Platelet Mimetic Particles for Targeting Thrombi in Flowing Blood. *Advanced Materials* 2013; **24**: 3864–9.
- 54 Tiukinhoy-Laing SD, Huang S, Klegerman M, Holland CK, McPherson DD. Ultrasound-facilitated thrombolysis using tissue-plasminogen activator-loaded echogenic liposomes. *Thromb Res* 2007; **119**: 777–84.
- 55 Shaw GJ, Meunier JM, Huang SL, Lindsell CJ, McPherson DD, Holland CK. Ultrasound-enhanced thrombolysis with tPA-loaded echogenic liposomes. *Thromb Res* Elsevier Ltd; 2009; **124**: 306–10.
- 56 Laing ST, Moody MR, Kim H, Smulevitz B, Huang SL, Holland CK, McPherson DD, Klegerman ME. Thrombolytic efficacy of tissue plasminogen activator-loaded echogenic liposomes in a rabbit thrombus model. *Thromb Res* Elsevier Ltd; 2012; **130**: 629–35.
- 57 Francis CW, Blinc A, Lee S, Cox C. Ultrasound accelerates transport of recombinant tissue plasminogen activator into clots. *Ultrasound Med Biol* 1995; **21**: 419–24.
- 58 Chen X, Leeman JE, Wang J, Pacella JJ, Villanueva FS. New insights into mechanisms of sonothrombolysis using ultra-high-speed imaging. *Ultrasound Med Biol* 2014; **40**: 258–62.
- 59 Sakharov D V., Hekkenberg RT, Rijken DC. Acceleration of Fibrinolysis by High-frequency Ultrasound : The Contribution of Acoustic Streaming and Temperature Rise. *Thromb Res* 2000; **100**: 333–40.
- 60 Hernot S, Klivanov AL. Microbubbles in ultrasound-triggered drug and gene delivery. *Adv Drug Deliv Rev* 2008; **60**: 1153–66.
- 61 Bader KB, Gruber MJ, Holland CK. Shaken and Stirred: Mechanisms of Ultrasound-

- Enhanced Thrombolysis. *Ultrasound Med Biol* 2014; **41**: 187–96.
- 62 Molina CA, Ribo M, Rubiera M, Montaner J, Santamarina E, Delgado-Mederos R, Arenillas JF, Huertas R, Purroy F, Delgado P, Alvarez-Sabín J. Microbubble administration accelerates clot lysis during continuous 2-MHz ultrasound monitoring in stroke patients treated with intravenous tissue plasminogen activator. *Stroke* 2006; **37**: 425–9.
- 63 Molina CA, Barreto AD, Tsivgoulis G, Sierzenski P, Malkoff MD, Rubiera M, Gonzales N, Mikulik R, Pate G, Ostrem J, Singleton W, Manvelian G, Unger EC, Grotta JC, Schellinger PD, Alexandrov A V. Transcranial ultrasound in clinical sonothrombolysis (TUCSON) trial. *Ann Neurol* 2009; **66**: 28–38.
- 64 Alexandrov A V., Mikulik R, Ribo M, Sharma VK, Lao AY, Tsivgoulis G, Sugg RM, Barreto A, Sierzenski P, Malkoff MD, Grotta JC. A pilot randomized clinical safety study of sonothrombolysis augmentation with ultrasound-activated perflutren-lipid microspheres for acute ischemic stroke. *Stroke* 2008; **39**: 1464–9.
- 65 Sharma PK, Guha SK. Transmission of time varying magnetic field through body tissue. *J Biol Phys* 1975; **3**: 95–102.
- 66 Tasci TO, Disharoon D, Schoeman RM, Rana K, Herson PS, Marr DWM, Neeves KB. Enhanced Fibrinolysis with Magnetically Powered Colloidal Microwheels. *Small* 2017; **1700954**: 1–11.
- 67 Jeong U, Teng X, Wang Y, Yang H, Xia Y. Superparamagnetic colloids: Controlled synthesis and niche applications. *Adv Mater* 2007; **19**: 33–60.
- 68 Bobo D, Robinson KJ, Islam J, Thurecht KJ, Corrie SR. Nanoparticle-Based Medicines: A Review of FDA-Approved Materials and Clinical Trials to Date. *Pharm Res Pharmaceutical Research*; 2016; **33**: 2373–87.
- 69 Arami H, Khandhar A, Liggitt D, Krishnan KM. In vivo delivery, pharmacokinetics, biodistribution and toxicity of iron oxide nanoparticles. 2016; **25**: 289–313.
- 70 Yang HW, Hua MY, Lin KJ, Wey SP, Tsai RY, Wu SY, Lu YC, Liu HL, Wu T, Ma YH. Bioconjugation of recombinant tissue plasminogen activator to magnetic nanocarriers for targeted thrombolysis. *Int J Nanomedicine* 2012; **7**: 5159–73.
- 71 Tadayon A, Jamshidi R, Esmaeili A. Delivery of tissue plasminogen activator and streptokinase magnetic nanoparticles to target vascular diseases. *Int J Pharm Elsevier B.V.*; 2015; **495**: 428–38.
- 72 Bi F, Zhang J, Su Y, Tang YC, Liu JN. Chemical conjugation of urokinase to magnetic nanoparticles for targeted thrombolysis. *Biomaterials Elsevier Ltd*; 2009; **30**: 5125–30.

- 73 Heid S, Unterweger H, Tietze R, Friedrich RP, Weigel B, Cicha I, Eberbeck D, Boccaccini AR, Alexiou C, Lyer S. Synthesis and Characterization of Tissue Plasminogen Activator — Functionalized Superparamagnetic Iron Oxide Nanoparticles for Targeted Fibrin Clot Dissolution. *Int J Mol Sci* 2017; **18**: 1–21.
- 74 Chen JP, Yang PC, Ma YH, Wu T. Characterization of chitosan magnetic nanoparticles for in situ delivery of tissue plasminogen activator. *Carbohydr Polym* Elsevier Ltd.; 2011; **84**: 364–72.
- 75 Chen JP, Yang PC, Ma YH, Tu SJ, Lu YJ. Targeted delivery of tissue plasminogen activator by binding to silica-coated magnetic nanoparticle. *Int J Nanomedicine* 2012; **7**: 5137–49.
- 76 Drozdov AS, Vinogradov V V., Dudanov IP, Vinogradov V V. Leach-proof magnetic thrombolytic nanoparticles and coatings of enhanced activity. *Sci Rep* Nature Publishing Group; 2016; **6**: 1–8.
- 77 Xie Y, Kaminski MD, Torno MD, Finck MR, Liu X, Rosengart AJ. Physicochemical characteristics of magnetic microspheres containing tissue plasminogen activator. *J Magn Magn Mater* 2007; **311**: 376–8.
- 78 Ma YH, Wu SY, Wu T, Chang YJ, Hua MY, Chen JP. Magnetically targeted thrombolysis with recombinant tissue plasminogen activator bound to polyacrylic acid-coated nanoparticles. *Biomaterials* Elsevier Ltd; 2009; **30**: 3343–51.
- 79 Inada Y, Ohwada K, Yoshimoto T, Kojima S, Takahashi K, Kodera Y, Matsushima A, Saito Y. Fibrinolysis by Urokinase Endowed with Magnetic Property. *Biochem Biophys Res Commun* 1987; **148**: 392–6.
- 80 Yoshimoto T, Ohwada K, Takahashi K, Matsushima A, Saito Y, Inada Y. Magnetic Urokinase: Targeting of Urokinase to Fibrin Clot. *Biochem Biophys Res Commun* 1988; **152**: 739–43.
- 81 Prilepskii AY, Fakhardo AF, Drozdov AS, Vinogradov V V., Dudanov IP, Shtil AA, Bel’Tyukov PP, Shibeko AM, Koltsova EM, Nechipurenko DY, Vinogradov V V. Urokinase-Conjugated Magnetite Nanoparticles as a Promising Drug Delivery System for Targeted Thrombolysis: Synthesis and Preclinical Evaluation. *ACS Appl Mater Interfaces* American Chemical Society; 2018; **10**: 36764–75.
- 82 Friedrich RP, Zaloga J, Schreiber E, Tóth IY, Tombácz E, Lyer S, Alexiou C. Tissue Plasminogen Activator Binding to Superparamagnetic Iron Oxide Nanoparticle—Covalent Versus Adsorptive Approach. *Nanoscale Res Lett* Nanoscale Research Letters; 2016; **11**: 1–11.
- 83 Hu J, Huang W, Huang S, ZhuGe Q, Jin K, Zhao Y. Magnetically active Fe₃O₄ nanorods loaded with tissue plasminogen activator for enhanced thrombolysis. *Nano Res* 2016; **9**:

- 2652–61.
- 84 Gravanis I, Tsirka SE. tPA as a therapeutic target in stroke. *Expert Opin Ther Targets* 2008; **12**: 1-18.
- 85 Torno MD, Kaminski MD, Xie Y, Meyers RE, Mertz CJ, Liu X, O'Brien WD, Rosengart AJ. Improvement of in vitro thrombolysis employing magnetically-guided microspheres. *Thromb Res* 2008; **121**: 799–811.
- 86 Huang L, ZhuGe Q, Cheng R, Zhao Y, Mao L, Yang B, Jin K, Huang W. Acceleration of Tissue Plasminogen Activator-Mediated Thrombolysis by Magnetically Powered Nanomotors. *ACS Nano* 2014; **8**: 7746–54.
- 87 Sitti M, Khalil ISM, Mahdy D, Sadek K, Tabak AF, Hamdi N. Rubbing Against Blood Clots Using Helical Robots: Modeling and In Vitro Experimental Validation. *IEEE Robot Autom Lett IEEE*; 2017; **2**: 927–34.
- 88 Voros E, Cho M, Ramirez M, Palange AL, De Rosa E, Key J, Garami Z, Lumsden AB, Decuzzi P. TPA Immobilization on Iron Oxide Nanocubes and Localized Magnetic Hyperthermia Accelerate Blood Clot Lysis. *Adv Funct Mater* 2015; **25**: 1709–18.
- 89 de Saint Victor M, Barnsley LC, Carugo D, Owen J, Coussios CC, Stride E. Sonothrombolysis with Magnetically Targeted Microbubbles. *Ultrasound Med Biol* 2019; **45**: 1151–63.
- 90 Nilsson M, Lasič S, Drobnjak I, Topgaard D, Westin CF. Resolution limit of cylinder diameter estimation by diffusion MRI: The impact of gradient waveform and orientation dispersion. *NMR Biomed* 2017; **30**: 1–13.
- 91 Rubiera M, Ribo M, Delgado-Mederos R, Santamarina E, Maisterra O, Delgado P, Montaner J, Alvarez-Sabín J, Molina CA. Do Bubble Characteristics Affect Recanalization in Stroke Patients Treated with Microbubble-Enhanced Sonothrombolysis? *Ultrasound Med Biol* 2008; **34**: 1573–7.
- 92 De Lizarrondo SM, Gakuba C, Herbig BA, Repessé Y, Ali C, Denis C V., Lenting PJ, Touzé E, Diamond SL, Vivien D, Gauberti M. Potent thrombolytic effect of N-acetylcysteine on arterial thrombi. *Circulation* 2017; **136**: 646–60.
- 93 Denorme F, Desender L, Vandenbulcke A, Deckmyn H, Vanhoorelbeke K, De Meyer SF, Langhauser F, Kleinschnitz C, Rottensteiner H, Plaimauer B, Scheiflinger F, François O, Andersson T. ADAMTS13-mediated thrombolysis of t-PA-resistant occlusions in ischemic stroke in mice. *Blood* 2016; **127**: 2337–45.
- 94 Bustamante A, Ning MM, García-Berrocso T, Penalba A, Boada C, Simats A, Pagola J, Ribó M, Molina C, Lo E, Montaner J. Usefulness of ADAMTS13 to predict response to recanalization therapies in acute ischemic stroke. *Neurology* 2018; **90**: e995–1004.

- 95 Ducroux C, Di Meglio L, Loyau S, Delbosc S, Boisseau W, Deschildre C, Maacha M Ben, Blanc R, Redjem H, Ciccio G, Smajda S, Fahed R, Michel JB, Piotin M, Salomon L, Mazighi M, Ho-Tin-Noe B, Desilles JP. Thrombus neutrophil extracellular traps content impair tPA-induced thrombolysis in acute ischemic stroke. *Stroke* 2018; **49**: 754–7.
- 96 Wyseure T, Peeters M, Gils A, Declerck PJ, Rubio M, De Lizarrondo SM, Vivien D, Denorme F, De Meyer SF. Innovative thrombolytic strategy using a heterodimer diabody against TAFI and PAI-1 in mouse models of thrombosis and stroke. *Blood* 2015; **125**: 1325–32.

CHAPTER 2

ASSEMBLY AND CONTROL OF MAGNETIC MICROWHEELS: A BRIEF SUMMARY

2.1 Introduction

The most promising strategy for achieving rapid targeted fibrinolysis is via magnetic tissue plasminogen activator (tPA) carriers (Table 1.2, 1.3). Our lab has developed magnetic microwheels (μ wheels) suitable for this task which can translate at velocities $>100 \mu\text{m/s}$ [1]. A μ wheel is a disc-shaped construction of (super)paramagnetic colloids which assembles spontaneously under a rotating magnetic field. What follows is background information regarding μ wheel assembly and translation.

2.2 Magnetic field generation and microwheel assembly

We generate a rotating magnetic field by passing periodic current through two pairs of Helmholtz coils arranged perpendicular to each other on the xy -plane [1,2]. The in-plane field components are

$$B_x = B_0 \cos(\omega_f t + \phi_x) \quad (2.1)$$

and

$$B_y = B_0 \cos(\omega_f t + \phi_y) \quad (2.2)$$

Here, $\omega_f = 2\pi f$ where f is the frequency of the magnetic field, and ϕ_x and ϕ_y are phase angles such that $\phi_y - \phi_x = \pi/2$. Superparamagnetic colloids under influence of the field experience induced dipole interactions and arrange in minimum energy configurations. In a static magnetic field, colloids tend to arrange in chains [3]; however, viscous drag on chains aligning with a rotating magnetic field results in disc-like structures that spin in the xy -plane (Fig 2.1A) [4]. A fifth coil on the z axis introduces a third component,

$$B_z = B_{z0} \cos(\omega_f t + \phi_z) \quad (2.3)$$

which reorients the axis of rotation (Fig 2.1B) [1]. Spinning μ wheels inclined relative to a nearby surface such as a glass slide behave as tires and roll because of wet friction. The phase angle ϕ_z determines the directional orientation of the field, and therefore the heading direction for μ wheels.

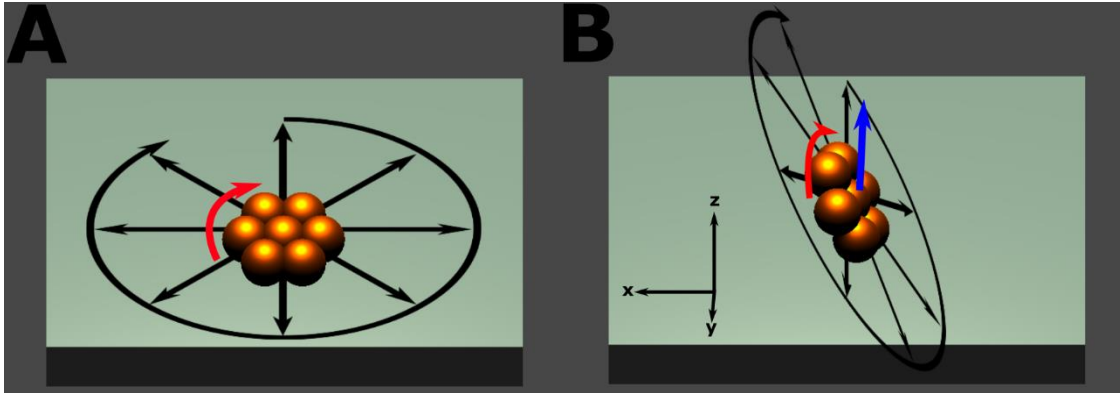


Figure 2.1 A) A μ wheel in a rotating magnetic field (black arrows) in the xy -plane spins (red arrow) but does not translate. B) When a z component is added to the magnetic field (black arrows), the μ wheel rolls (red arrow) along the surface and translates (blue arrow).

2.3 Microwheel translation

The translational velocity can be predicted from the magnitude and frequency of the magnetic field by performing a set of force balances. The forces on the z axis are the load and normal forces (Fig 2.2A).

$$\sum F_z = L - N = 0 \quad (2.4)$$

Balancing the equation yields

$$L = N = mng \cos(\theta_c) \quad (2.5)$$

where m is the mass of a spherical particle, n is the number of particles in the μ wheel, g is the gravitational constant, and θ_c is the camber angle, defined as offset from the z axis (Fig 2.2B).

The camber angle can be calculated as

$$\theta_c = \tan^{-1} \frac{B_0}{B_{z0}} \quad (2.6)$$

The forces on the x axis are the frictional force, which propels the μ wheel forward, and the drag force.

$$\sum F_x = F_F - F_D = 0 \quad (2.7)$$

The frictional force is

$$F_F = \mu_k L \quad (2.8)$$

where μ_k is the coefficient of wet friction, and the drag on a disc is [5]:

$$F_D = 32\eta RV/3. \quad (2.9)$$

Here, η is the liquid viscosity, R is the radius of the disc, and V is the translational velocity.

The wet friction coefficient can be approximated by balancing the frictional torque with the torque required to shear the liquid layer between the disc and the wall [6]. The shear stress of the liquid layer approximately scales as the wheel edge velocity V^* over the gap width h :

$$\tau \sim \eta(V^*/h). \quad (2.10)$$

The torque required to shear a liquid layer with contact area A is

$$T_s = \tau AR, \quad (2.11)$$

and the frictional torque is the product of the frictional force with the wheel radius,

$$T_F = \mu_k LR. \quad (2.12)$$

Equating the torques to solve for the friction coefficient yields

$$\mu_k = \eta V^*/hP. \quad (2.13)$$

where $P = L/A$ is the pressure in the gap. Finally, substituting all terms into the force balance (Eqn 2.7) gives an expression for the translational velocity:

$$V = \frac{3nmg}{32hP} \omega \cos(\theta_c) \quad (2.14)$$

where ω is the rotational frequency of the disc.

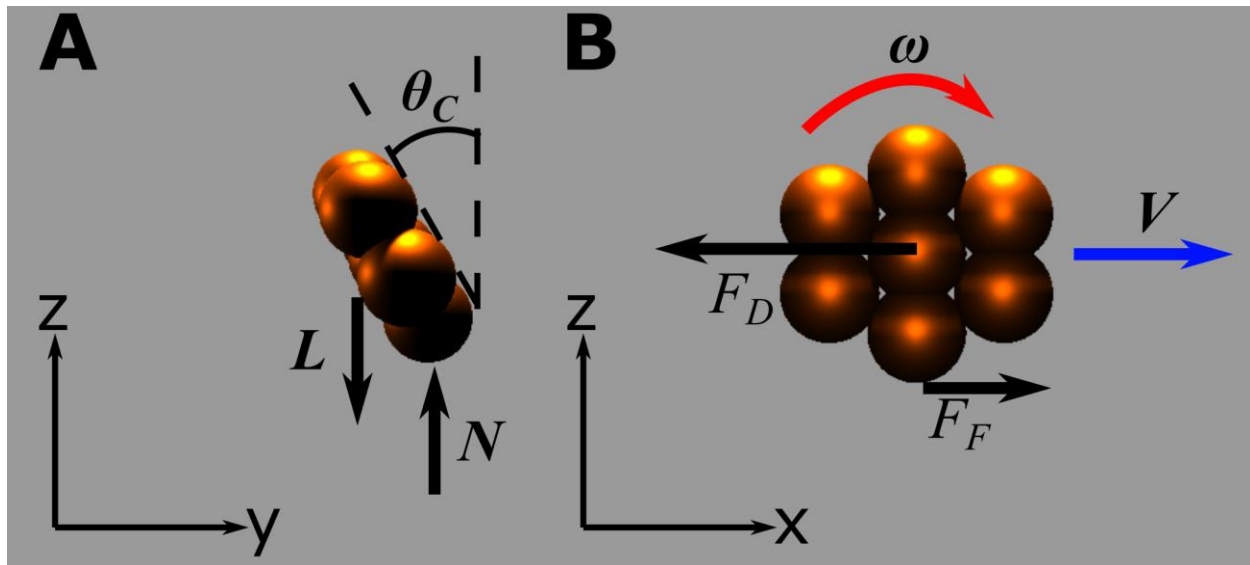


Figure 2.2: Free body diagram of a μ wheel at camber angle θ_c , rotating at angular frequency ω , and translating at velocity V . A) The forces on the z axis are the load and normal forces. B) Friction and drag are the forces on the x axis.

2.4 Conclusions

A primary obstacle to overcome in developing actuated thrombolytic technologies is navigating the 3D vasculature in the presence of high-shear blood flow. Controlling μ wheel velocity will be an essential technology. From Eqn 2.14, it is readily apparent that velocity scales with rotational frequency and μ wheel size. It is less obvious how velocity changes relative to gap width as a decrease in h also causes an increase in lubrication pressure P . In Chapter 3, we quantify the gap width and explore strategies to control it.

2.5 References

- 1 Tasci TO, Herson PS, Neeves KB, Marr DWM. Surface-enabled propulsion and control of colloidal microwheels. *Nat Commun* Nature Publishing Group; 2016; **7**: 10225.
- 2 Roth EJ, Zimmermann CJ, Disharoon D, Tasci TO, Marr DWM, Neeves KB. An experimental design for the control and assembly of magnetic microwheels. *Rev Sci Instrum* AIP Publishing, LLC; 2020; **91**.
- 3 Yuan B, Cademartiri L. Flexible One-Dimensional Nanostructures: A Review. *J Mater Sci Technol* Elsevier Ltd; 2015; **31**: 607–15.

- 4 Faraudo J, Camacho J. Cooperative magnetophoresis of superparamagnetic colloids: Theoretical aspects. *Colloid Polym Sci* 2010; **288**: 207–15.
- 5 Tanzosh JP, Stone HA. Transverse motion of a disk through a rotating viscous fluid. *J Fluid Mech* 1995; **301**: 295–324.
- 6 Szeri A. Fluid Film Lubrication: Theory and Design. Cambridge: Cambridge University Press; 1998.

CHAPTER 3

AC/DC MAGNETIC FIELDS FOR ENHANCED TRANSLATION OF COLLOIDAL MICROWHEELS

This chapter is adapted with permission from

*Langmuir*⁵

Dante Disharoon⁶, David W.M. Marr⁷, and Keith B. Neeves⁸

3.1 Abstract

Microscale devices must overcome fluid reversibility to propel themselves in environments where viscous forces dominate. One approach, used by colloidal microwheels consisting of superparamagnetic particles assembled and powered by rotating AC magnetic fields, is to employ a nearby surface to provide friction. Here, we used total internal reflection microscopy to show that individual 8.3 μm particles roll inefficiently with significant slip due to a particle-surface fluid gap of 20-80 nm. We determined that both gap width and slip increase with increasing particle rotation rate when the load force is provided by gravity alone, thus providing an upper bound on translational velocity. By imposing an additional load force with a DC magnetic field gradient superimposed on the AC field we were able to decrease the gap width and thereby enhance translation velocities. For example, an additional load force of 0.2 F_g provided by a DC field gradient increased translational velocity from 40 to 80 $\mu\text{m/s}$ for a 40 Hz

⁵ Reprinted with permission from: Disharoon D, Neeves KB, Marr DWM. Ac/dc Magnetic Fields for Enhanced Translation of Colloidal Microwheels. *Langmuir* American Chemical Society; 2019; **35**: 3455–60. Copyright 2019, American Chemical Society.

⁶ Primary author, Colorado School of Mines

⁷ Colorado School of Mines

⁸ Colorado School of Mines, University of Colorado School of Medicine

rotation rate. Translation velocity increases with decreasing gap width whether the gap is varied by DC field gradient induced load forces or by reducing the Debye length with salt. These results present a strategy to accelerate surface-enabled rolling of microscale particles and open the possibility of high speed μ wheel rolling independent of gravitational field.

3.2 Introduction

Colloidal materials can be used as microscale bots capable of translation [1-8] and cargo delivery [9-14]. Methods to power and direct them include electric [15], optical [16], magnetic [17-19], or chemical [20,21] gradients, self-propelling particles [22-24], various motile structures including rotors [25], micro-worms [26] and swarms [27,28], and particle geometries that break symmetry [29-31]. Our previous work has focused on the use of colloidal building blocks that can be assembled in-situ using alternating current (AC) magnetic fields to create rotating microwheels (μ wheels) that translate by rolling on nearby surfaces [32,33]. While we have shown that μ wheels can move at speeds up to $\sim 100 \mu\text{m/s}$, they are inefficient rollers. Their translational velocity is $\sim 10\%$ of their maximum due to slip caused by the fluid-filled gap between rotating μ wheels and the associated surface [32]. In such small gaps under translation, lubrication forces, in addition to colloidal forces, play an important role in controlling gap width [34]. It is this gap that determines the wet friction coefficient μ_k and the resulting friction force $F_f = \mu_k L$, with L the load, propelling rotating μ wheels forward [32]. For particles under a load force provided by gravity alone, this force can be expressed as $F_f = \frac{\eta}{hP} \Omega a (\rho - \rho_f) V g$, where a is the particle radius, h is the gap width, Ω is the rotation rate, η is the viscosity of the medium, P is the pressure in the gap, ρ is the particle density, ρ_f is the fluid density, V is the particle volume and g is the gravitational acceleration [32]. From this, we expect that reducing the gap width will

increase wet friction and seek here to develop strategies to manipulate the gap for enhanced μ wheel translation.

While wet friction and slip determine the efficiency of movement, a load force is required to provide contact between μ wheel and surface. Relying solely on gravity is limiting because it is fixed in magnitude and direction, reducing the effective load L when the rolling surface is not normal to gravity. To address this, an alternative or supplemental load force can be provided with direct current (DC) magnetic field gradients. In this study, we use DC field gradients superimposed on AC fields to provide forces of order 60 fN, or $\sim 1/5^{\text{th}}$ the load for single particles provided by gravity and then use total internal reflection microscopy (TIRM) to measure gap width because of its sensitivity and nanometer scale resolution [35-37]. The accuracy of TIRM for slightly-absorbing colloids with magnetic domains has been previously verified [38], and we apply it here to characterize μ wheels during translation where models based on diffusion such as Stokes-Einstein cannot be applied [39]. We then show that gradient-based load forces can vary the distance between μ wheel and surface and investigate the role of gap width on translation speed.

3.3 Experimental Section

3.3.1 Superparamagnetic particles

A double-sided gasket cut from 3M tape (467MP with 200MP adhesive, Maple, MN) of 0.5 cm inner diameter was affixed to the top surface of a Dove prism (ThorLabs, PS991, Newton, NJ). A 10 μ L sample of 8.3 μ m superparamagnetic spheres (COMPEL COOH Glacial Blue, UMGB003-UMC4f, Fishers, IN) of density 1.1-1.2 g/ml suspended in deionized water, resistivity = 18.2 m Ω /cm, was injected into the gasket well and sealed with a coverslip. These particles were chosen for their large size, which minimizes the contribution of Brownian

fluctuations on the measured gap width. To determine particle surface roughness, particle suspensions were dried on glass slides and an AFM (Asylum Research, Santa Barbara, CA) was used in air tapping mode with a silicon probe with a resonant frequency of 190 kHz and a spring constant of 48 N/m (Tap190E-G, Budget Sensors, Sofia, Bulgaria). Zeta potential was measured with a ZetaPALS zeta potential analyzer (Brookhaven Instruments, Long Island, NY).

3.3.2 Magnetic field application

A rotating AC magnetic field was generated using five 50 mm ID air-cored solenoids with 400 turns. An analog output card (National Instruments (NI), NI-9623, Austin, TX) controlled by Matlab generated a current that was subsequently amplified (Behringer, EP2000, Willich, Germany). The final current passed through each coil, measured using an analog input card (NI-USB-6009), was 2 A, resulting in a field strength of 4.5 mT at the sample. The frequency of the rotating field was varied between 4 and 100 Hz. Additional coils positioned above or below the sample were used to generate DC load forces of magnitude $F_x = V\chi_p(B_x dB_x/dx)/\mu_o$ where $\chi_p = 0.96$ is the particle susceptibility and μ_o is the permeability of free space. The fields were determined along the coil axis via $B_x = \mu_o R^2 I / [2(x^2 + R^2)]^{3/2}$ where R is the coil radius and I is the current, summed over the coil windings, including a 50 mm ID, 400 turn coil, a 25 mm ID 200 turn coil, and a 100 mm 400 turn coil (Appendix A, Fig A.1). Videos were recorded using custom-developed BFCam software using a camera (EPIX, SV643M, New York City, NY) at 200 fps through a 40X objective (Olympus, Plan Ach NA = 0.65, Center Valley, PA). Video processing and data analysis were performed using custom Matlab code (Matlab File Exchange ID# 69646).

3.3.3 Total Internal Reflection Microscopy

In TIRM, colloids scatter an evanescent wave with an intensity that depends on the location of the colloid relative to the surface: $I = I_0 e^{-\beta h}$. Here, I is the scattered light intensity,

I_0 is the scattered intensity at the glass-water interface and β^{-1} is the evanescent wave penetration depth. TIRM experiments were performed on an Olympus BX40 microscope using a 532 nm laser (Spectra Physics, Millennia V, Mountain View, CA) emitting at 0.25 W. The laser beam passed through the 10 mm Dove prism at a 42° incident angle (Fig. 3.1). To calibrate measured scatter intensity, we identified a stuck particle in intimate surface contact and used the scattered intensity as our baseline, I_0 . Prior to each experiment, the prism was washed in 1:1 12M HCl and MeOH for 45 min before being rinsed in filtered DI water for 5 min in triplicate. The samples and the scattered light were imaged using an Epix SV 643M camera calibrated for intensity measurements with an optical power meter (Newport, Model 835, Irvine, CA) equipped with a photosensor assembly (Newport, Model 818-SL) with a detection range of gap widths between $0 \leq h \leq 400$ nm (Appendix A, Fig A.1).

3.3.4 Preparation of Janus sphere

Measuring the rotation frequency of individual particles requires labeling and, to do so, we sputtered 49 ± 3 nm thick silver hemispheres onto particles for contrast (Appendix A, Fig. A.2, Video 3.S1). 10 μ L of a solution of 8.3 μ m beads (Glacial Blue, COMPEL, Fishers, IN) at a concentration of $3.3 * 10^6$ beads/ μ L were deposited onto a glass coverslip. A permanent magnet was used to spread the solution evenly across the coverslip before the sample was dried. Sputtering was performed in an AJA Sputter System using a 99.99% purity silver target (Kurt J. Lesker, Jefferson Hills, PA). The bead sample was brought to a base pressure of 0.38 mTorr before argon was injected to a working pressure of 5 mTorr and a 50 W RF power supply was used to apply 46 V DC for 4.5 min. The thickness of the silver film was measured with profilometry (Dektak 3030, Veeco, Plainview, NY). Composition of the silver caps was verified using an EDAX energy dispersive X-ray spectroscopy system (EDAX, Draper, UT). Janus

spheres were recovered by washing the glass slide with DI water while physically wiping the coverslip with a swab. Janus spheres were used to build standard curves (Appendix A, Fig A.3) of rotation rate versus applied field frequency but, because of additional evanescent-wave scattering induced by the metal coating, were not used in measurements of gap width.

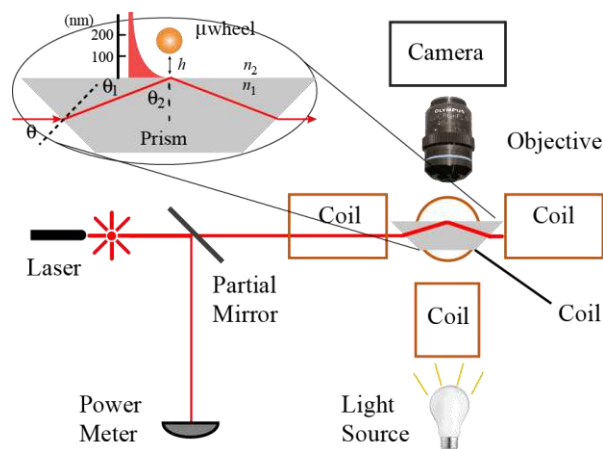


Figure 3.1: Experimental apparatus. Coils generate an AC or AC/DC magnetic field that cause μ wheels to roll near a prism surface, scattering an evanescent wave created by a laser passing through the prism. Laser power is measured continuously via power meter. Scattered intensity is measured using a calibrated camera and normalized by laser output. Inset: $\theta = 42^\circ$, $\theta_1 = 70.1^\circ$, $\theta_2 = 25.1^\circ$, $n_1 = 1.52$ and $n_2 = 1.33$.

3.4 Results and Discussion

3.4.1 Gap width measurement for rolling spheres

We measured that spheres with a zeta potential of -68 ± 10 mV under Brownian motion centered on average 21 ± 6 nm from the wall ($n > 100$, where n is the number of measurements), in accord with other studies using TIRM experiments under similar conditions [40-42]. Note that this gap is much smaller than the particle diameter, indicating that the spheres are in a regime where wall effects, including increased viscous drag and hindered mobility on rotating and translating spheres, are significant [43, 44].

Upon application of an AC magnetic field, particles rotate, translate, and move away from the surface (Fig 3.2A). Particle rotation rate and AC field frequency are equivalent up to a

field frequency of 40 Hz (Appendix A, Fig. A.3). The observed movement of the particles away from the wall is attributed to lubrication forces that arise during translation. We note that gap width and translation velocity v_t increase with increasing particle rotational frequency from 10-30 Hz (Fig. 3.2B); however, for rotation rates greater than 30 Hz there is no observable increase in velocity or gap width.

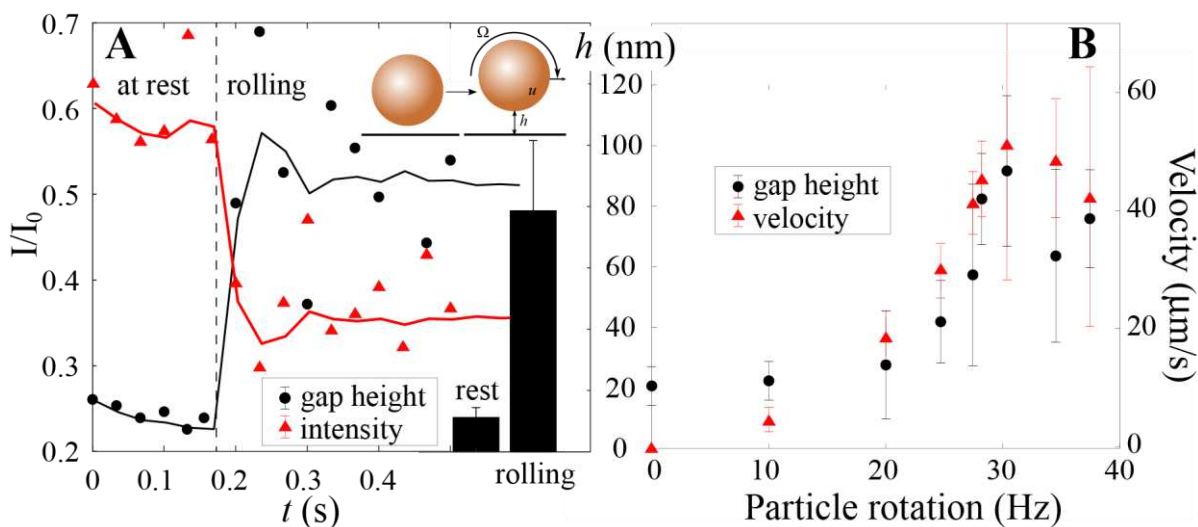


Figure 3.2: A) Normalized intensity in TIRM and calculated gap width for a single sphere transitioning from Brownian to rolling. The dotted line indicates the time when the AC field is turned on. The field strength is 4.5 mT and $\Omega = 30$ Hz. *The lines represent moving averages.* B) Gap width and velocity as a function of particle rotation rate [Video 3.S2]. Both velocity and gap width measurements at higher rotation rates are subject to large experimental error. Sources of error include variable particle density, magnetic doping, surface roughness, sphericity and size. Data represent the mean and standard deviation of $n = 25$ -450 particles.

As wet friction is inversely proportional to gap, increasing the load force should result in enhanced translation. To test this, we applied a DC field gradient load force equal to $\pm 0.2 F_g$ ($F_g = 0.3$ pN); a DC load in the direction of gravity (+) pulls spheres closer to the surface while a force applied against gravity (-) pushes them farther away. Gap width decreases with increasing load and increases with decreasing load (Fig. 3.3A; Video 3.S3). We measured a

corresponding behavior in translational velocity; as gap width decreases, velocity increases. A 22% increase in gap width reduces velocity by 27%, but a corresponding decrease in gap width doubles it; therefore, velocity is very sensitive to particle proximity to the wall. In addition, the frequency dependence of both gap width and translational velocity is preserved in the presence of a DC load force (Fig 3.3A). An alternative approach to reducing the gap width is to manipulate the Debye length λ_D by adding salt (Fig 3.3B inset) as described by DLVO theory [45, 46]. At these separations, DLVO interactions are dominated by charge-charge repulsions between the carboxyl groups on the particle surface and the hydroxyl groups on the glass slide. Addition of NaCl resulted in expected trends, gap width decreases at higher salt concentrations [42] while velocity increases (Fig 3.3B). It is important to note that this data represents values for those particles that remained mobile. At higher salt concentrations, most particles stuck to the wall with ~50% stuck at a salt concentration of 0.001M and >95% at 0.1M. While added salt is an effective method for reducing gap width, controlling gap via magnetic forces avoids most sticking in our system and provides enhanced velocities compared to load forces by gravitational fields alone (Fig. 3.3C).

To describe the relationship between velocity and gap width, we equate the frictional force $F_f = \frac{\eta}{hP} \Omega a (\rho - \rho_f) V g$ with the drag force $F_D = 6\pi\eta a v_t$. Assuming constant pressure in the gap under steady-state translation, we expect $v_t \propto \Omega L/h$ (Fig. 3.3D) and the velocity to increase as the gap width decreases because of increased wet friction. To quantify rolling efficiency, we define slip as $s = 1 - \frac{v_t}{v_r}$ where $v_r = 2\Omega a$ is the rotation velocity [47]. At $s = 1$, there is complete slip and no translation; at $s = 0$, the translational velocity is equal to the rotation velocity. With this, a corresponding scaling for slip is $(1 - s) \propto L/h$ as provided in Fig 3.4A.

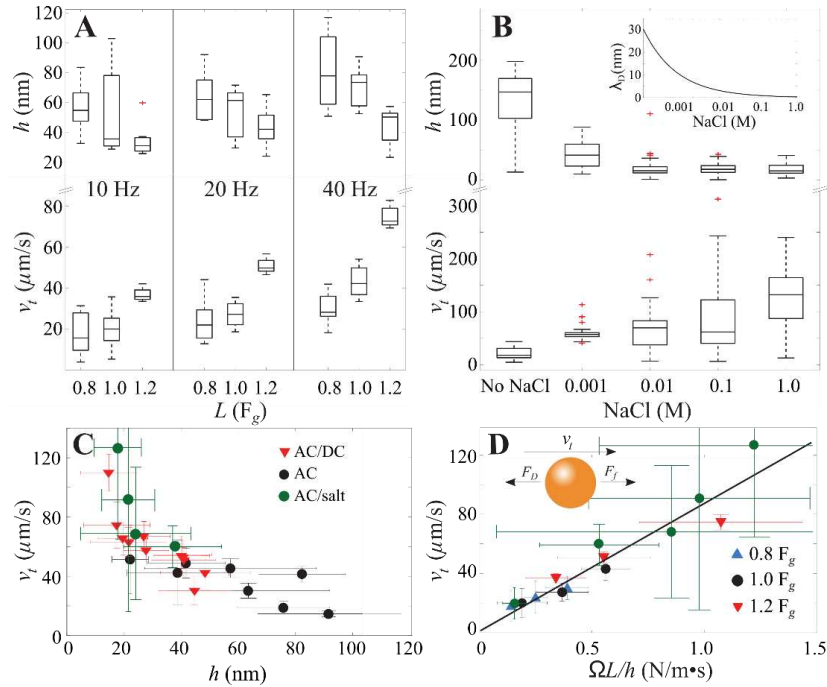


Figure 3.3 Varying gap with DC-induced load force or screening electrostatic repulsion A) The load force is varied $\pm 0.2 F_g$ using a 2.5 mT DC magnetic field. Velocity and gap width are shown at field frequencies of 10, 20, and 40 Hz. B) NaCl concentration is varied to manipulate the Debye length (inset) for a field frequency of 40 Hz. Note that the data provided here is for non-sticking particles only. For A and B, $n = 250$ -1250 measurements. C) Translational velocity as a function of gap width for particle rotation rates of $10 < \Omega < 40$. For AC/DC samples (red triangles), load force is $1.2 F_g$. Data represent averages and standard deviation of $n = 25$ -450 measurements. D) A force balance between frictional force F_f and drag force F_D provides a linear relationship between the translational velocity and experimental parameters. Error bars calculated from propagation of error in experimental measurements of v_b , Ω , and h .

The relationship between slip and gap width for all experimental conditions shows two regimes (Fig. 3.4B). In the first, there is a significant increase in slip with increasing gap width up to ~ 20 nm. In the second, there is a more modest increase in slip at larger gap widths. The transition between these two regions is equivalent to the average particle surface roughness (~ 20 nm) as measured by AFM (Fig 3.4C), suggesting asperities on the particle may influence interactions with the rolling surface. This is congruent with the observation that particle motion appears to have a stick-slip type motion and translate faster in the small gap regime (Fig. 3.4D). At gap widths larger than 20 nm the motion is smoother, suggesting colloids roll primarily by a

wet friction mechanism. Even with an increased load force of $1.2 F_g$, the minimum slip we observe is 0.79, suggesting there is room for larger enhancements in translational velocity if sufficient torques are available to overcome increased friction.

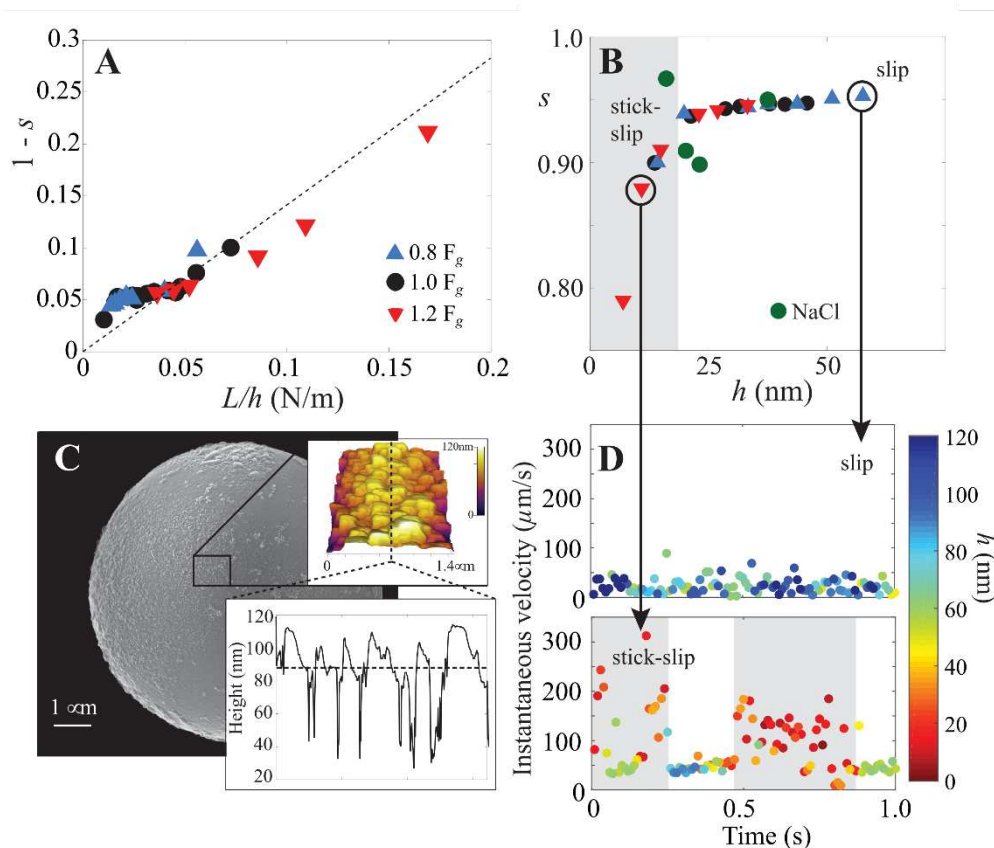


Figure 3.4: A) The traction coefficient ($1-s$) follows the predicted scaling (dotted line) for all experimental conditions. B) A transition in slip is observed at a gap width of ~ 20 nm. Data summarizes experiments across all rotation frequencies and field conditions. C) Electron micrograph of a single colloidal particle and representative AFM image and surface roughness profile insets (corrected for curvature). Dashed line is the average height corrected for curvature. D) Instantaneous velocity measurements from representative data in B show stick-slip behavior at length scales less than or equal to the particle surface roughness (Video 3.S4).

3.5 Summary and Conclusions

Using TIRM, we have measured the gap width of AC magnetic field-induced rolling of colloidal spheres. Compared to resting spheres under the influence of Brownian motion, rolling spheres lift away from the surface to a gap width that dictates slip and translational efficiency.

We have shown that adjusting gap width with DC magnetic load forces on the order of $0.2 F_g$ facilitates enhanced translational velocity. Similarly, we showed that adjusting the gap by decreasing the double layer thickness also yields enhanced translational velocity. Taken together, these observations suggest that the gap width directly impacts wet friction between μ wheels and the surface. Scaling arguments based on balancing frictional and drag forces demonstrate an inverse relationship between translation velocity and gap width. For small gaps, spheres translate via stick-slip behavior where particle surface features increase the frictional force and enhance translation. Future studies could consider higher DC field gradients such that particles translate exclusively in the “stick” regime, where our data indicates translation speeds are fivefold larger than in the “slip” regime. The technique of combining AC and DC fields to drive μ wheels could also be particularly useful when the gravitational load is reduced, for example in translation on non-horizontal and curved surfaces.

3.6 References

- 1 Moran JL, Posner JD. Phoretic Self-Propulsion. *Annu Rev Fluid Mech* 2017; **49**: 511–40.
- 2 Illien P, Golestanian R, Sen A. “Fuelled” motion: Phoretic motility and collective behaviour of active colloids. *Chem Soc Rev* Royal Society of Chemistry; 2017; **46**: 5508–18.
- 3 Ng WM, Che HX, Guo C, Liu C, Low SC, Chieh Chan DJ, Mohamud R, Lim J. Artificial Magnetotaxis of Microbot: Magnetophoresis versus Self-Swimming. *Langmuir* American Chemical Society; 2018; **34**: 7971–80.
- 4 Chen XZ, Jang B, Ahmed D, Hu C, De Marco C, Hoop M, Mushtaq F, Nelson BJ, Pané S. Small-Scale Machines Driven by External Power Sources. *Adv Mater* 2018; **30**: 1–22.
- 5 Wang W, Chiang TY, Velegol D, Mallouk TE. Understanding the efficiency of autonomous nano- and microscale motors. *J Am Chem Soc* 2013; **135**: 10557–65.
- 6 Ahmed D, Baasch T, Jang B, Pane S, Dual J, Nelson BJ. Artificial Swimmers Propelled by Acoustically Activated Flagella. *Nano Lett* 2016; **16**: 4968–74.
- 7 Dreyfus R. Flexible Magnetic Microswimmers. *Microbiorobotics*. Elsevier Inc.; 2012.

- 8 Du D, Hilou E, Biswal SL. Reconfigurable paramagnetic microswimmers: Brownian motion affects non-reciprocal actuation. *Soft Matter* 2018; **14**: 3463–70.
- 9 Erkoç P, Yasa IC, Ceylan H, Yasa O, Alapan Y, Sitti M. Mobile Microrobots for Active Therapeutic Delivery. *Adv Ther* 2019; **2**: 1800064.
- 10 Zhang L, Petit T, Lu Y, Kratochvil BE, Peyer KE, Pei R, Lou J, Nelson BJ. Controlled Propulsion and Cargo Transport of Rotating Nickel Nanowires near a Patterned Solid Surface. *ACS Nano* 2010; **4**: 6228–34.
- 11 Gao W, Kagan D, Pak O, Clawson C. Cargo-Towing Fuel-Free Magnetic Nanoswimmers for Targeted Drug Delivery. *Small* 2012; **8**: 460–7.
- 12 Wang J. Cargo-towing synthetic nanomachines: Towards active transport in microchip devices. *Lab Chip* 2012; **12**: 1944–50.
- 13 Sundararajan S, Sengupta S, Ibele ME, Sen A. Drop-off of colloidal cargo transported by catalytic Pt-Au nanomotors via photochemical stimuli. *Small* 2010; **6**: 1479–82.
- 14 Sitti M, Ceylan H, Hu W, Giltinan J, Turan M, Yim S, Diller E. Biomedical Applications of Untethered Mobile Milli/Microrobots. *Proc IEEE Inst Electr Electron Eng* 2015; **103**: 205–24.
- 15 Ma F, Wang S, Wu DT, Wu N. Electric-field-induced assembly and propulsion of chiral colloidal clusters. *Proc Natl Acad Sci* 2015; **112**: 6307–12.
- 16 Weibel DB, Garstecki P, Ryan D, DiLuzio WR, Mayer M, Seto JE, Whitesides GM. Microoxen: Microorganisms to move microscale loads. *Proc Natl Acad Sci U S A* 2005; **102**: 11963–7.
- 17 Benelmekki M, Martinez LM, Andreu JS, Camacho J, Faraudo J. Magnetophoresis of colloidal particles in a dispersion of superparamagnetic nanoparticles: Theory and experiments. *Soft Matter* 2012; **8**: 6039–47.
- 18 Watarai H, Suwa M, Iiguni Y. Magnetophoresis and electromagnetophoresis of microparticles in liquids. *Anal Bioanal Chem* 2004; **378**: 1693–9.
- 19 Faraudo J, Camacho J. Cooperative magnetophoresis of superparamagnetic colloids: Theoretical aspects. *Colloid Polym Sci* 2010; **288**: 207–15.
- 20 Ebbens SJ, Gregory DA. Catalytic Janus Colloids: Controlling Trajectories of Chemical Microswimmers. *Acc Chem Res* American Chemical Society; 2018; **51**: 1931–9.
- 21 Paxton WF, Kistler KC, Olmeda CC, Sen A, St. Angelo SK, Cao Y, Mallouk TE, Lammert PE, Crespi VH. Catalytic nanomotors: Autonomous movement of striped

- nanorods. *J Am Chem Soc* 2004; **126**: 13424–31.
- 22 Hong Y, Blackman NMK, Kopp ND, Sen A, Velegol D. Chemotaxis of nonbiological colloidal rods. *Phys Rev Lett* 2007; **99**: 1–4.
- 23 Han K, Shields CW, Velev OD. Engineering of Self-Propelling Microbots and Microdevices Powered by Magnetic and Electric Fields. *Adv Funct Mater* 2018; **28**: 1–14.
- 24 Singh AK, Dey KK, Chattopadhyay A, Mandal TK, Bandyopadhyay D. Multimodal chemo-magnetic control of self-propelling microbots. *Nanoscale* 2014; **6**: 1398–405.
- 25 Tierno P, Golestanian R, Pagonabarraga I, Sagués F. Controlled swimming in confined fluids of magnetically actuated colloidal rotors. *Phys Rev Lett* 2008; **101**: 1–4.
- 26 Martinez-Pedrero F, Ortiz-Ambriz A, Pagonabarraga I, Tierno P. Colloidal Microworms Propelling via a Cooperative Hydrodynamic Conveyor Belt. *Phys Rev Lett* 2015; **115**: 1–5.
- 27 Driscoll M, Delmotte B, Youssef M, Sacanna S, Donev A, Chaikin P. Unstable fronts and motile structures formed by microrollers. *Nat Phys* 2017; **13**: 375–9.
- 28 Bricard A, Caussin JB, Desreumaux N, Dauchot O, Bartolo D. Emergence of macroscopic directed motion in populations of motile colloids. *Nature* Nature Publishing Group; 2013; **503**: 95–8.
- 29 Gong D, Cai J, Celi N, Feng L, Jiang Y, Zhang D. Bio-inspired magnetic helical microswimmers made of nickel-plated *Spirulina* with enhanced propulsion velocity. *J Magn Magn Mater* 2018; **468**: 148–54.
- 30 Kümmel F, Ten Hagen B, Wittkowski R, Buttinoni I, Eichhorn R, Volpe G, Löwen H, Bechinger C. Circular motion of asymmetric self-propelling particles. *Phys Rev Lett* 2013; **110**: 1–5.
- 31 Yang T, Tasci TO, Neeves KB, Wu N, Marr DWM. Magnetic Microlasos for Reversible Cargo Capture , Transport , and Release. *Langmuir* 2017; **33**: 5932–7.
- 32 Tasci TO, Herson PS, Neeves KB, Marr DWM. Surface-enabled propulsion and control of colloidal microwheels. *Nat Commun* Nature Publishing Group; 2016; **7**: 10225.
- 33 Tasci TO, Disharoon D, Schoeman RM, Rana K, Herson PS, Marr DWM, Neeves KB. Enhanced Fibrinolysis with Magnetically Powered Colloidal Microwheels. *Small* 2017; : 1–11.
- 34 Honig CDF, Ducker WA. Thin film lubrication for large colloidal particles: Experimental test of the no-slip boundary condition. *J Phys Chem C* 2007; **111**: 16300–12.

- 35 Huang P, Breuer KS. Direct measurement of anisotropic near-wall hindered diffusion using total internal reflection velocimetry. *Phys Rev E - Stat Nonlinear, Soft Matter Phys* 2007; **76**: 1–4.
- 36 Oetama RJ, Walz JY. A new approach for analyzing particle motion near an interface using total internal reflection microscopy. *J Colloid Interface Sci* 2005; **284**: 323–31.
- 37 Walz JY, Suresh L. Study of the sedimentation of a single particle toward a flat plate. *J Chem Phys* 1995; **103**: 10714–25.
- 38 Blickle V, Babič D, Bechinger C. Evanescent light scattering with magnetic colloids. *Appl Phys Lett* 2005; **87**: 1–4.
- 39 Eloul S, Compton RG. General Model of Hindered Diffusion. *J Phys Chem Lett* 2016; **7**: 4317–21.
- 40 Prieve DC. Measurement of colloidal forces with TIRM. *Adv Colloid Interface Sci* 1999; **82**: 93–125.
- 41 Bevan MA, Prieve DC. Hindered diffusion of colloidal particles very near to a wall: revisited. *J Chem Phys* 2000; **113**: 1228–36.
- 42 Suresh L, Walz JY. Direct measurement of the effect of surface roughness on the colloidal forces between a particle and flat plate. *J Colloid Interface Sci* 1997; **196**: 177–90.
- 43 Goldman AJ, Cox RG, Brenner H. Slow viscous motion of a sphere parallel to a plane wall—I Motion through a quiescent fluid. *Chem Eng Sci* 1967; **22**: 637–51.
- 44 Liu Q, Prosperetti A. Wall effects on a rotating sphere. *J Fluid Mech* 2010; **657**: 1–21.
- 45 Derjaguin B, Landau LD. Theory of the Stability of Strongly Charged Lyophobic Sols and of the Adhesion of Strongly Charged Particles in Solutions of Electrolytes. *Acta Physicochim URSS* 1941; **14**: 633–62.
- 46 Israelachvili JN. Intermolecular and Surface Forces: Third Edition. *Intermolecular and Surface Forces: Third Edition*. 2011.
- 47 Fujii K, Fujimoto H. Traction control based on slip ratio estimation without detecting vehicle speed for electric vehicle. *Fourth Power Convers Conf PCC-NAGOYA 2007 - Conf Proc* 2007; : 688–93.

CHAPTER 4

ENHANCED FIBINOLYSIS WITH MAGNETICALLY POWERED COLLOIDAL MICROWHEELS

The remainder of this thesis relies heavily on work published in 2017. Because the article appeared as part of the author's master's thesis, it is included as Appendix B rather than in the main body.

In Appendix B, microwheels (μ wheels) are functionalized with tissue plasminogen activator (tPA- μ wheels) and driven towards a fibrin gel formed in a microfluidic channel. tPA- μ wheels efficiently translate to the gel and localize at concentrations 2 to 3 orders of magnitude higher than diffusing tPA. The degradation of the fibrin gel is measured as a function of time, and experiments are characterized by fibrinolysis rate. tPA- μ wheels carrying an active concentration of 3.6 $\mu\text{g/mL}$ lyse clots at rates equivalent to 10 $\mu\text{g/mL}$ of free tPA. We also develop a strategy to achieve mechanical penetration of tPA- μ wheels into the fibrin gel. In this, the directional orientation of the rotating magnetic field changes such that tPA- μ wheels follow a corkscrew trajectory. Corkscrew penetration improves the fibrinolysis rates of tPA- μ wheels by two- to fourfold.

CHAPTER 5

BREAKING THE FIBRINOLYTIC SPEED LIMIT WITH MICROWHEEL CO-DELIVERY OF TISSUE PLASMINOGEN ACTIVATOR AND PLASMINOGEN

5.1 Abstract

Fibrinolysis is the enzymatic degradation of fibrin, the biopolymer that gives blood clots their mechanical integrity. To reestablish blood flow in vessels occluded by clots, tissue plasminogen activator (tPA) can be used; however, its efficacy is limited by transport to and into a clot and by the depletion of its substrate, plasminogen. To overcome these rate limitations, we design a platform to co-deliver tPA and plasminogen based on microwheels (μ wheels), wheel-like assemblies of superparamagnetic colloidal beads that roll along surfaces at high speeds and carry therapeutic payloads in applied magnetic fields. By experimentally measuring fibrinolysis of plasma clots at varying concentrations of tPA and plasminogen, the biochemical speed limit was first determined. These data, in conjunction with measurements of μ wheel translation, activity of immobilized tPA on beads, and plasminogen release kinetics from magnetic mesoporous silica nanoparticles (mMSN), were used in a mathematical model to identify the optimal tPA:plasminogen ratio and guide the coupling of plasminogen-loaded mMSN to tPA-functionalized superparamagnetic beads. Once coupled, particle-bead assemblies form into a co-delivery vehicle that rolls to plasma clot interfaces and lyses them at rates comparable to the biochemical speed limit. With the addition of mechanical action provided by rotating μ wheels to penetrate clots, this barrier was exceeded by rates 40-fold higher lysis by 50 nM tPA. This co-delivery of an immobilized enzyme and its substrate via a microbot capable of mechanical work

has the potential to target and rapidly lyse clots that are inaccessible by mechanical thrombectomy devices or recalcitrant to systemic tPA delivery.

5.2 Introduction

Microbots are promising therapeutic vehicles because of their potential to target drug delivery to disease-afflicted sites within the body [1]. Their propulsion can be achieved using applied magnetic [2,3], electric [4], optic [5], and acoustic fields [6,7]. Of these strategies, magnetic field-based propulsion approaches are particularly well suited for in vivo applications because magnetic fields do not attenuate in tissue [8] and are not harmful to the human body. As a result, magnetically-controlled microbots have been proposed for the treatment of cancer [9,10], ocular surgery [11], and tissue damage [12] where targeted drug delivery could provide substantial benefit. Building on these studies, we have recently shown that microbots can not only deliver drug but also impart mechanical action to aid in drug efficacy, specifically in the targeting of blood clots for the treatment of stroke [13].

Fibrinolysis is the biochemical breakdown of fibrin, which is the biopolymer that gives clots their mechanical integrity [14]. It can be used to reestablish blood flow in various types of thrombosis including myocardial infarction [15], deep vein thrombosis [16], pulmonary embolism [17], ischemic stroke [18,19], and limb ischemia [20]. Recombinant tissue plasminogen activators (tPAs) are the only currently Food and Drug Administration approved thrombolytic drug. They work by binding to and converting the zymogen plasminogen to the enzyme plasmin, an interaction that is greatly accelerated in the presence of its co-factor fibrin [21]. Plasmin in turn cleaves lysyl and arginyl bonds at many different sites to transect cross-linked fibrin fibers producing several different fragments [22].

The rate of fibrinolysis by tPA is limited by both transport processes and biochemical reactions [23]. The transport of tPA to the clot periphery can be the rate limiting step in intravenous delivery because it is diffusion-dominated in occluded vessels with low or no blood flow (Fig. 5.1A) [24,25]. tPA (alteplase) has a half-life of minutes in blood due to inactivation by its endogenous inhibitors plasminogen activator inhibitors 1 and 2 and thus is often eliminated before it reaches the thrombus [26,27]. These limitations can be partially overcome by catheter directed intraarterial delivery, however only 20% of stroke patients have large artery occlusions that are accessible to catheters [28]. Tenecteplase is an engineered tPA that is less susceptible to endogenous inhibitors and has a higher affinity for fibrin [29], but it has not shown superior performance to alteplase in clinical trials for ischemic stroke [30]. Even once delivered, penetration of tPA is limited by its high binding affinity to fibrin fibers which localizes it to the first few micrometers of the thrombus interface [31,32]. Acting as an effective affinity filter, this leads to surface erosion with little penetration of tPA into the clot. While a direct strategy of increasing tPA concentration to overcome slow diffusion rates would seem desirable, this is bounded by the bleeding risks associated with degradation of fibrinogen, plasminogen, and α -antiplasmin, lysis of hemostatic clots, and tPA neurotoxicity [33,34].

Counterintuitively, the speed of fibrinolysis does not increase monotonically with tPA concentration. Rather, a bell-shaped curve has been reported with a maximum lysis rate occurring at ~20 nM tPA for compacted plasma clots [35]. This is surprising because the plasma concentration of plasminogen (~2 μ M) is much higher than the therapeutic tPA concentration (5-50 nM), an observation explained by consumption of *local* plasminogen due its high affinity binding to partially degraded fibrin and subsequent conversion to plasmin [36–39]. Supplemental plasminogen and platelet derived plasminogen enhance the fibrinolysis rates [40,41] suggesting

that plasminogen is the limiting factor in the presence of high plasminogen activator concentrations (Fig. 5.1B).

The functionalization of micro- and nanoparticles with tPA overcomes some of the transport and kinetic limitations of fibrinolysis by protecting tPA from inhibition and using targeting moieties to platelets and fibrin that localize particles on a clot while maintaining low circulating concentrations [42]. Microparticles manipulated by external fields, or microbots, offer further advantages of not relying on blood flow for delivery [43,44]. For example, tPA functionalized magnetic particles pulled towards a clot with a magnetic field gradient improves thrombolytic outcomes in mice [45] and rats [46–48] models of thrombosis compared to free tPA. Rotating magnetic microbots can also act as local mixers, reducing concentration gradients near the interface of a clot to accelerate tPA-mediated thrombolysis [44].

In previous work with assemblies of superparamagnetic microparticles functionalized with tPA (tPA- μ wheels), we have shown that actuation using rotating magnetic fields enables both delivery at high concentrations and mechanical disruption of clots, ultimately leading to an inside-out bulk erosion (Fig. 5.1C) [13]. However, while we were able to achieve local tPA concentrations that were three orders-of-magnitude higher than those by diffusive delivery of tPA, this resulted in only a one order-of-magnitude increase in fibrinolysis speed. Based on these results it appears that fibrinolysis using tPA- μ wheels is plasminogen limited as reported in other studies of fibrinolysis at high tPA concentrations [49]. To overcome this limitation and further enhance lysis speed, we develop here a μ wheel-based strategy of delivering both tPA and plasminogen using tPA- μ wheels coupled with mesoporous silica nanoparticles (MSN), which we have previously used to achieve controlled release of proteins [50–52]. These co-laden μ wheels

break the biochemical speed limit by supplementing fresh plasminogen and burrowing their way into plasma-derived clots (Fig. 5.1D).

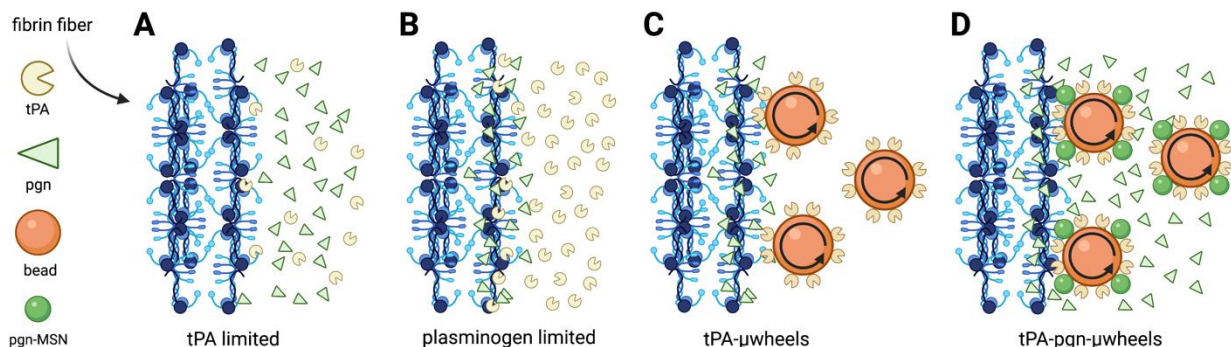


Figure 5.1: A) The rate-limiting steps of fibrinolysis include the transport to a clot and binding of tPA to fibrin fibers at low tPA concentrations. B) At sufficiently high tPA concentrations, its substrate plasminogen (pgn), becomes the limiting factor in fibrinolysis. C) These rate-limiting steps are overcome using magnetically powered μ wheels, superparamagnetic beads (orange spheres) that self-assemble in rotating magnetic fields. When μ wheels are coupled to tPA (tPA- μ wheels) they accumulate at the clot interface leading to high tPA concentrations and plasminogen limited fibrinolysis. D) By attaching plasminogen releasing nanoparticles (green spheres) to μ wheels (tPA-pgn- μ wheels) co-delivery of both enzyme and substrate are achieved yielding fibrinolysis rates that overcome plasminogen-limited fibrinolysis.

5.3 Results

5.3.1 Plasminogen depletion limits fibrinolysis rate at high tPA concentrations

To measure the extent to which fibrinolysis is rate-limited by tPA, we exposed a plasma clot formed with thrombin to varying concentrations of tPA and plasminogen (Fig. 5.2A). For a physiologic plasminogen concentration of 1 μ M, the fibrinolysis rate, defined by the dissolution of the fibrin front over time, increases with increasing tPA concentrations from 50 nM up to 200 nM tPA (Fig. 5.2A, first column). However, at tPA concentrations $>$ 200 nM the lysis rate decreases. Doubling the plasminogen concentration to 2 μ M while holding tPA concentration at 50 nM resulted in a 65% increase in lysis rate and up to a 120% increase in lysis rate at tPA concentrations of 250-800 nM. Note that there is an optimal plasminogen concentration for a

given tPA concentration that yields the maximum lysis rate (Fig. 5.2B). Plasminogen concentrations above this optimum attenuate fibrinolysis suggesting a competition for fibrin binding sites between tPA and plasminogen. Probing further, we measured fibrinolysis rates for a range of tPA:plasminogen ratios and identified accelerated fibrinolysis (AF) zones, defined as regions where lysis rates are within 10% of the maximum, or exceed $13.5 \mu\text{m}/\text{min}$ (Fig. 5.2A). Here, it is apparent that there is a biochemical speed limit in the range to 200-600 nM tPA and 2-4 μM plasminogen, suggesting that a strategy of co-delivering tPA and plasminogen at these concentrations could significantly accelerate fibrinolysis. μ Wheels are well-suited for such a strategy because they are assembled from component, potentially-multifunctional, building blocks and can be driven to and accumulate at the edge of a clot, achieving a high local concentration of both the enzyme and its substrate adjacent to their co-factor.

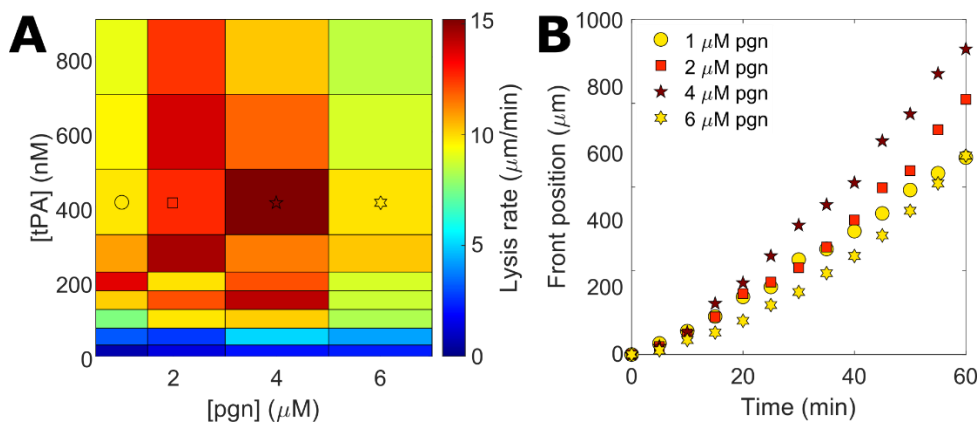


Figure 5.2: Measuring the fibrinolytic speed limit of plasma clots. A) Heat map of lysis rates as a function of tPA and plasminogen (pgn) concentrations. The bold border outlines the accelerated fibrinolysis (AF) zone. Symbols denote data shown in panel B. B) Dissolution of fibrin at 400 nM tPA with endogenous plasma plasminogen concentration (1 μM) and the addition of exogenous plasminogen up to 6 μM total plasminogen concentration.

5.3.2 Synthesis and characterization of plasminogen releasing magnetic colloids

To create tPA- μ wheels, we functionalize streptavidin DynabeadsTM (beads) with biotinylated tPA (tPA-beads) (Fig. 5.3A). These tPA-beads readily assemble into tPA- μ wheels

with application of a magnetic field [13]. To co-deliver plasminogen and tPA, we use mesoporous silica nanoparticles (MSN) with incorporated iron oxide nanoparticles to make them magnetic and increase coupling rate of beads and MSNs. We covalently coupled biotinylated magnetic mesoporous silica nanoparticles (mMSN) to beads to create studded beads, then functionalized the studded beads with tPA (tPA-studded beads) (Fig. 5.3A). Finally, the tPA-studded beads were incubated with plasminogen to load the mMSN to yield a superparamagnetic bead that can release plasminogen and carry immobilized tPA (pgn-tPA-beads) (Fig. 5.3A).

The mMSN were synthesized with an average diameter 161 ± 57 nm and circularity 0.61 ± 0.17 and imaged using transmission electron microscopy (TEM) (Fig. 5.3B). Iron oxide content was measured at 10.5 wt% with 90% confidence using quantitative energy dispersive X-ray spectroscopy (EDS) (Fig. 5.3C). Nitrogen sorption isotherms show adsorption at relative pressures between 0.3 and 1.0 with most hysteresis occurring at $\frac{P}{P_0} = 0.7$ (Fig. 5.3D), indicating the presence of both micro- and mesopores with a wide range of pore sizes. The Barrett-Joyner-Halenda (BJH) method was used to determine an accessible pore volume of $0.4 \text{ cm}^3/\text{g}$ distributed over a wide range of pore sizes with an average of 14.6 ± 5.7 nm. Magnetization curves for the mMSN confirmed that the particles are paramagnetic and amenable to magnetic control (Fig. 5.3E) allowing us to couple them to superparamagnetic beads with long-range magnetic attractions more efficiently than by mixing alone. Coupling between mMSN and beads was verified using scanning electron microscopy (SEM) (Fig. 5.3F).

5.3.3 Designing co-delivery strategy for tPA and plasminogen

A strategy that relies solely on higher tPA concentrations does not necessarily lead to faster lysis (Fig. 5.2B). One of the features of the synthesis approach (Fig. 5.3A) is that the relative concentrations of tPA and plasminogen can be adjusted independently by varying the

ratio of tPA-beads to plasminogen-loaded mMSN. To predict appropriate relative concentrations, we developed a mathematical model (see *Methods*) to estimate the local concentrations of tPA and plasminogen at a fibrin front. The model requires inputs of experimental data, presented below, to calculate μ wheel number density at the clot interface and plasminogen release rate from mMSN.

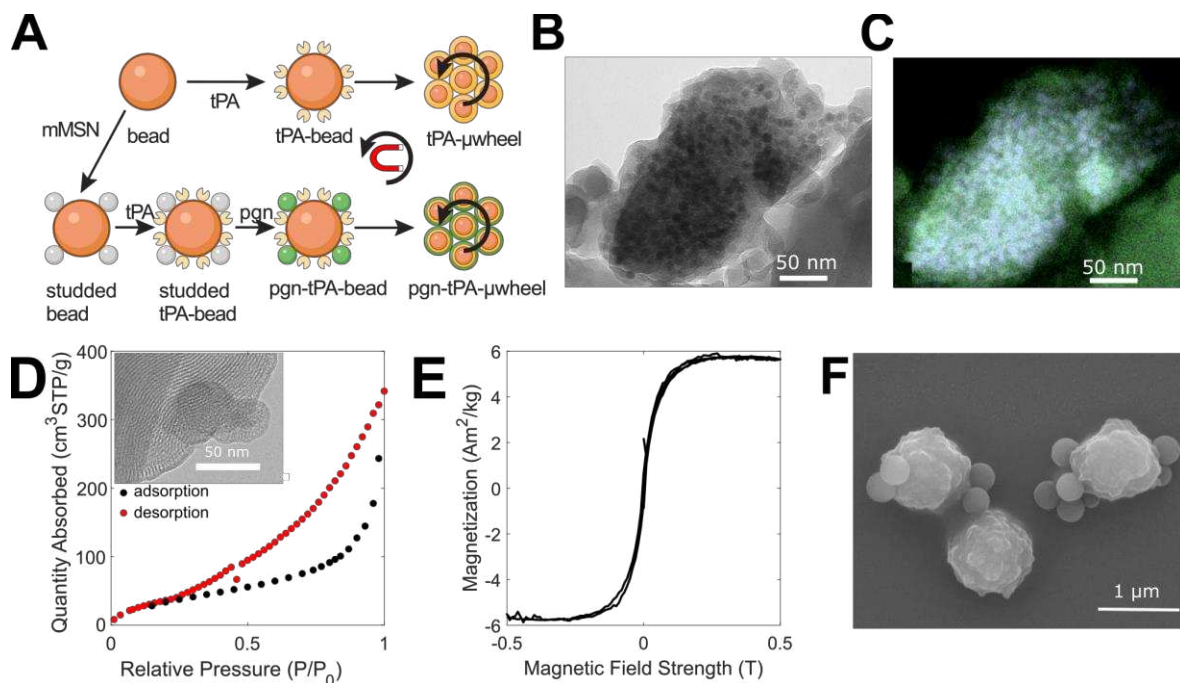


Figure 5.3: Synthesis and characterization of magnetic mesoporous silica nanoparticles (mMSN) and their coupling to superparamagnetic beads. A) Schematic of tPA-functionalization, mMSN-bead coupling, and plasminogen (pgn) loading to create tPA- and tPA-pgn- μ wheels. B) Transmission electron micrograph (TEM) of mMSN. Darker areas are Fe_3O_4 domains incorporated into the silica matrix. C) High-angle annular dark field energy-dispersive X-ray (HAADF-EDS) spectrum showing iron oxide domains (blue) distributed throughout silica matrix (green). D) Representative BJH isotherm data with TEM image of pore structure (inset). E) Magnetization profile for mMSN. F) Scanning electron micrograph (SEM) of studded beads.

Under the influence of rotating magnetic fields, both tPA-beads and pgn-tPA-beads self-assemble into μ wheels. The velocity profiles of μ wheels consisting of various numbers of beads, or ‘-mers’, are shown in Fig. 4A-B. μ Wheels consisting of tPA-beads translate with a lognormal velocity profiles (Eqn 5.2, Fig. 5.4A) and an average velocity of $6.8 \mu\text{m/s}$. Larger tPA- μ wheels

translate faster than smaller tPA- μ wheels as previously reported [53]. μ Wheels consisting of pgn-tPA-beads translate with a negatively skewed Gaussian velocity profile (Eqn 5.3, Fig. 5.4B) and an average velocity of $7.7 \mu\text{m/s}$. Differences here can be ascribed to asperities on the surface of beads that increase their translational velocity [54] and the mMSNs on the pgn-tPA-beads likely perform in a similar fashion.

Plasminogen release kinetics from pgn-mMSN and pgn-tPA-beads were measured by UV absorbance (Fig. 5.4C). Pgn-tPA-beads have a lower loading capacity than pgn-mMSN, likely because some pores are inaccessible when coupled to beads. The amount of plasminogen released from pgn-tPA-beads was $66 \pm 2\%$ of that released from pgn-mMSN for a fixed mMSN number density. The activity of tPA- and pgn-tPA-beads is equivalent to 8 nM tPA , a value not significantly affected by co-functionalization with pgn-mMSN (Fig. 5.4D). We measured the tPA activity on pgn-tPA-beads using a fluorogenic substrate as a function of coverage. As more mMSNs are bound to the beads, the surface available for tPA functionalization decreases as reflected in the decrease of tPA activity with higher coverage (Fig. 5.5A).

Mass action kinetics were used to model the binding of tPA and plasminogen to fibrin, as well as the conversion of plasminogen to plasmin (Eqns 5.6-5.9). The velocity (Fig. 5.4A), plasminogen release (Fig. 5.4C), and tPA activity (Figs 5.4D, 5.5A) data are used to calculate the rate of transport of pgn- and tPA-laden μ wheels to the fibrin front and the local plasminogen and tPA concentrations (Eqns 5.5, 5.7, and 5.9). This model permits the prediction of plasminogen and tPA concentrations over time for a given number of mMSN/bead.

We used the model to calculate the percentage of time during a 60 min experiment in the AF zones defined in Fig. 5.2B as concentration ratios where lysis rates exceed $13.5 \mu\text{m/min}$. Coverage of 10-20 yielded the most favorable results with both species being maintained at

target concentrations for at least 45 min (Fig. 5.5B). The model predicts that lower coverage results in faster plasminogen depletion than replenishment, while high coverage limits the available tPA on the bead surface.

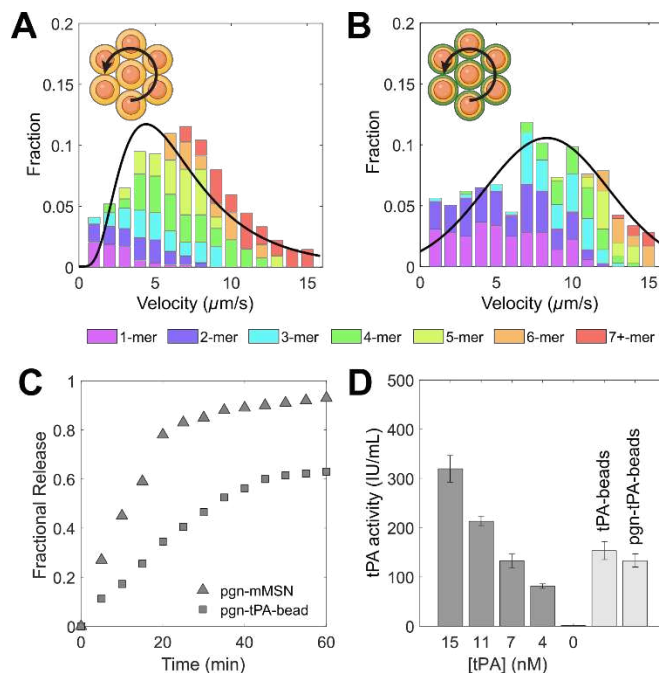


Figure 5.4 Representative velocity profile for tPA-beads (A) and pgn-tPA-beads (B). C) Plasminogen release profile for pgn-mMSN and pgn-tPA-beads at a number density of $10^6/\mu\text{L}$. Fractional release is normalized to the total plasminogen loading as measured by spectrometry. D) Activity of $10^5/\mu\text{L}$ bead populations compared to solvated tPA.

To control the coverage, we varied the mixing time of the streptavidin beads and biotinylated mMSN (Fig. 5.5C). The coverage is 0-2 after 3 hr and 3-5 after 48 hr, a relatively slow association rate likely limited by steric hindrance at the bead surface. To achieve higher coverage, a 4 mT uniform magnetic field was applied across the sample, roughly doubling the coverage ratio for all mixing times (Fig. 5.5C). The distribution of coverage for a mixing time of 24 hr and a 4 mT field is shown in Fig. 5.5D. An average coverage of 8 mMSN/bead was achieved in 48 hr with a 4 mT field, a ratio where μ wheels are predicted to achieve lysis in the

AF zone for at least 40% of 1 hr experiment. This mixing time and magnetic field were used to synthesize pgn-tPA-beads for fibrinolysis experiments.

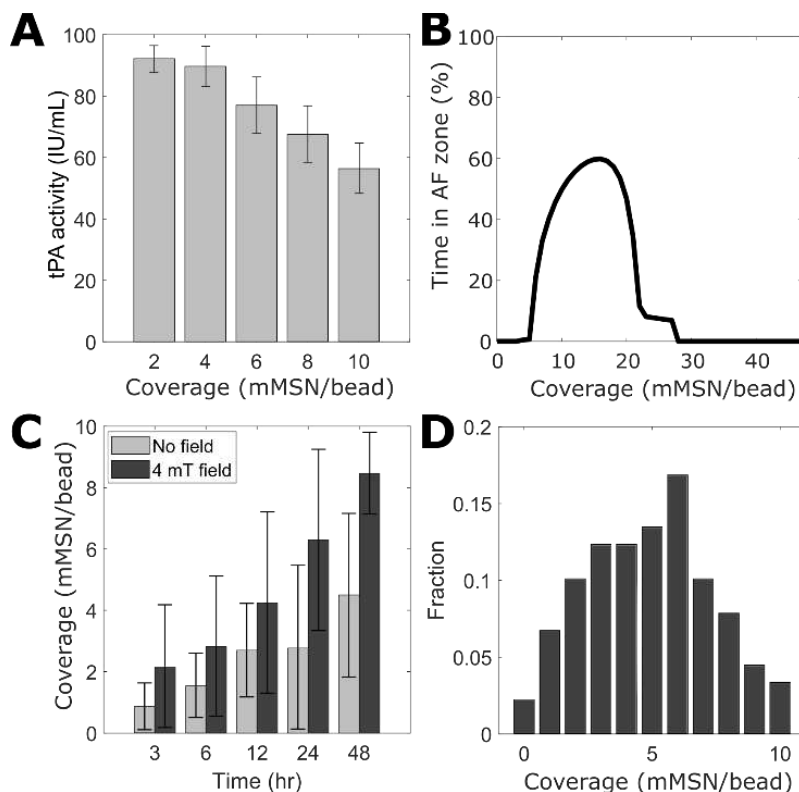


Figure 5.5 A) tPA activity as a function of coverage as measured using a fluorogenic substrate in a plate reader. B) Percentage of a 60 min experiment during which plasminogen concentration is within the accelerated fibrinolysis (AF) zones, defined as regions where lysis exceeds $13.5 \mu\text{m}/\text{min}$ (see Fig. 5.2B). C) Coverage of mMSN to beads as a function of mixing time in the with and without a 4 mT magnetic field. D) Histogram of coverage for $t = 24$ hr in the presence of a 4 mT magnetic field ($n=50$). Data in (A) and (C) expressed as average and standard deviation of $n = 3$ and 25, respectively.

5.3.4 Fibrinolysis with μ wheel co-delivery of tPA and plasminogen

Fibrinolysis experiments were conducted on plasma clots with four formulations: free tPA, tPA-beads, tPA-beads and pgn-mMSN (uncoupled), and pgn-tPA-beads (coupled) (Fig. 5.6A, Video 5.S1). Particles with an initial activity equivalent to 5 nM tPA or free tPA (50 nM) were injected 1 mm from the fibrin front and a rotating magnetic field (6.2 mT, 10 Hz) was used to

roll magnetic particles and their μ wheel assemblies to the fibrin gel front. Free tPA diffused slowly to the fibrin front, resulting in negligible lysis for the first 20 min of the experiment (Fig. 5.6B). Our model estimates that the concentration of tPA at the fibrin front after 60 min is only 15 nM, indicating that transport is the rate-limiting process in this case (Appendix D, Fig. D.1A). Once measurable, lysis proceeded at a linear rate of $0.42 \pm 0.13 \mu\text{m}/\text{min}$ for the duration of the experiment (Fig. 5.6B,C).

Experiments using tPA-beads were characterized by a shorter lag time (~ 10 min) than tPA as μ wheels translate and accumulate at the fibrin front faster than diffusion (Fig. 5.6B). After this lag time, lysis rate accelerates as the accumulation of tPA- μ wheels increases until it reaches a maximum of $2.9 \pm 0.7 \mu\text{m}/\text{min}$ (Fig. 5.6C) and then decreases after ~ 35 min. Our mathematical model estimates that tPA reaches 250 nM in 5 min and that plasminogen is depleted after 40 min (Appendix D, Fig. D.1B) with tPA- μ wheels. When tPA- μ wheels are supplemented with uncoupled pgn-mMSN, the maximum lysis rate increases to $4.5 \pm 1.2 \mu\text{m}/\text{min}$ (Fig. 5.6B). This relatively modest increase compared to tPA-beads alone is due to a limited amount of plasminogen replenishment; after 60 min, the plasminogen concentration is estimated to be $0.3 \mu\text{M}$ at the clot front (Appendix D, Fig. D.1C).

The lysis rate of pgn-tPA- μ wheels reaches a maximum rate of $13.6 \pm 0.9 \mu\text{m}/\text{min}$ (Fig. 5.6C) for the first 30 min of the experiment (Fig. 5.6B), consistent with the measured plasminogen release kinetics (Fig. 5.4C). The lag time is reduced for pgn-tPA- μ wheels because of their increased average translation speed relative to tPA- μ wheels (Fig. 5.4A-B). After 30 min, the pgn-tPA- μ wheel lysis rate approaches the rate of tPA- μ wheels since most plasminogen has been released. Notably, this formulation reaches the biochemical speed limit of $\sim 15 \mu\text{m}/\text{min}$ (Fig. 5.2B) suggesting that both tPA and plasminogen are near their target concentrations. The

mathematical model predicts that tPA reaches 250 nM after 10 min and plasminogen concentration remains above 1 μ M for the duration of the experiment (Appendix D, Fig. D.D1D).

In order to break the biochemical speed limit, we used the magnetic field to manipulate μ wheels along a corkscrew trajectory as we have previously demonstrated that this allows μ wheels to penetrate into clots [13]. Pgn-tPA- μ wheels following a corkscrew trajectory (Video 5.S2) are 40-fold more effective fibrinolytics than 50 nM tPA and reach a maximum lysis rate of $20.3 \pm 1.0 \mu\text{m}/\text{min}$ (Fig. 5.6C). As μ wheels burrow their way into a clot (Video 5.S3), new fibrin fibers are available for binding of tPA and plasmin(ogen) that are not accessible during surface erosion. This mechanical penetration combined with high tPA and plasminogen concentration yields an inside-out lysis pattern that exceeds the maximum lysis rate achieved using only biochemical means (Fig. 5.2B).

5.4 Discussion

The speed of fibrinolysis is governed by a series of rate-limiting transport and biochemical reaction steps. We have attempted to overcome each of those steps with the co-delivery of a fibrinolytic enzyme, tPA, and its substrate, plasminogen, with a magnetically powered microbot. We measured the biochemical speed limit of fibrinolysis using different combinations of tPA and plasminogen concentrations and found that we can break that limit using this co-delivery strategy in combination with mechanical action created through corkscrew motion of μ wheels.

The first rate-limiting step that must be overcome to achieve thrombolysis is the transport of fibrinolytics like tPA to a clot. Systemic delivery of fibrinolytic agents relies on diffusion to reach an impermeable occlusive clot [24], which is slow compared to active modes of transport

or convection. We overcome this transport barrier by immobilizing tPA on magnetic beads which are assembled into μ wheels that roll along a straight path to the clot. Using the active transport reduced the lag time to the start of fibrinolysis. Active transport also provides the opportunity to have a subtherapeutic circulating concentration of tPA immobilized on beads that accumulates at the clot at very high concentration.

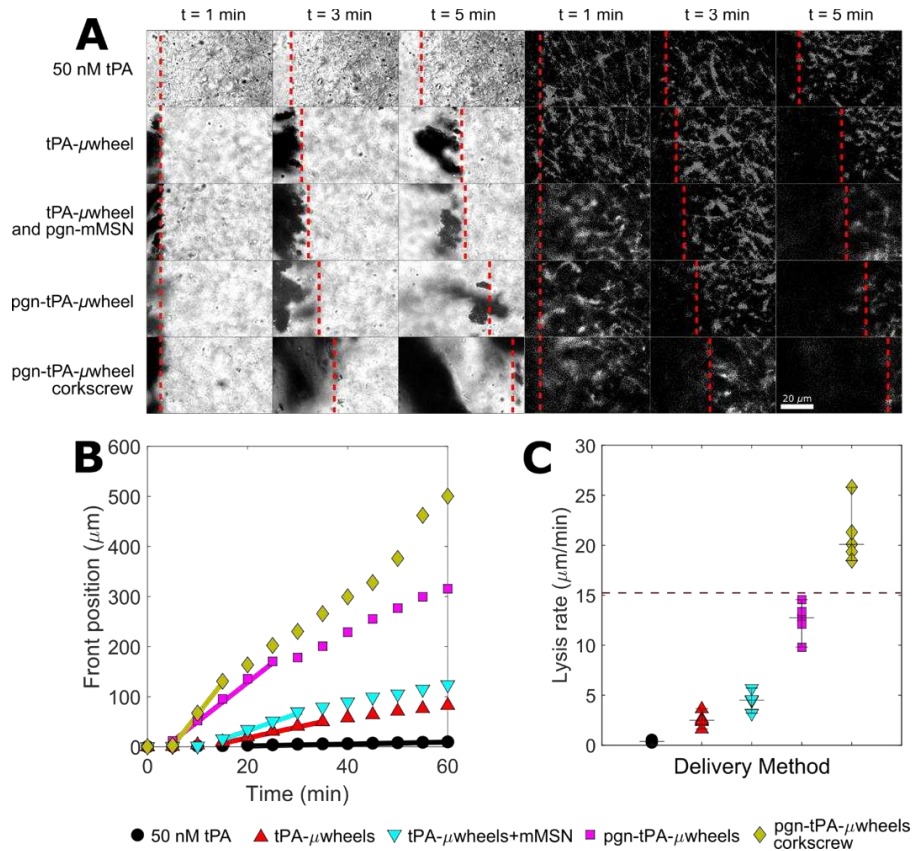


Figure 5.6: A) Time lapse of lysis of plasma clots using different μ wheel formulations. Brightfield at left, and fluorescently labeled fibrin(ogen) at right. Dashed lines indicate the front position. B) Representative lysis curves for each formulation. Lines indicate periods of maximum lysis rates lasting for a minimum of 10 min. C) Maximum lysis rates for each formulation. Corkscrew condition uses pgn-tPA- μ wheels. Dashed line indicates biochemical speed limit (see Fig. 5.2B).

The second rate-limiting step is the binding of tPA to fibrin. This step can be accelerated by increasing the concentration of tPA in systemic or intraarterial delivery. However, this approach is limited by the bleeding risk associated with high systemic concentrations of tPA.

Using a μ wheel delivery strategy offers an alternative solution because μ wheels can be injected at subtherapeutic systemic concentration of tPA and subsequently localize at high concentrations at the clot interface. For example, in this study the tPA activity on our injected tPA-pgn-beads was comparable to 5 nM of free tPA, while the tPA activity of the accumulated μ wheels at the clot interface is > 250 nM. tPA immobilized on microparticles is also less likely to enter the extravascular space due to their size and therefore has the potential to be less neurotoxic in stroke applications.

At sufficiently high tPA concentrations, plasminogen is the limiting factor in fibrinolysis speed [49]. Once the fibrin front is replete with tPA, increasing tPA concentration further inhibits fibrinolysis because tPA both consumes the available plasminogen and competes with plasmin and plasminogen for fibrin binding sites. Here, we demonstrate that this limitation can not only be overcome by co-delivering a plasminogen payload with tPA using a microbot platform but can also approach the biochemical speed limit.

Both tPA and plasminogen have high affinity for fibrin fibers which limits their penetration into a clot leading to surface erosion of a clot with minimal penetration into low permeability clots. Thus, the last rate limiting step to overcome is the number of accessible fibrin binding sites [55]. We have previously shown the potential to access binding sites within the interior of a clot, and a bulk erosion from the inside-out, using a μ wheel corkscrew motion [13]. Here we show that the corkscrew motion, in combination with co-delivery of tPA and plasminogen, breaks the biochemical speed limit by allowing μ wheels to penetrate into the clot.

Using magnetically actuated pgn-tPA- μ wheels, we have overcome each rate limiting step and achieved lysis rates that exceed even suprathreshold concentrations of tPA. Our 40-fold increase in lysis rate over therapeutic concentrations of 50 nM tPA is a larger relative increase

compared to other approaches that use magnetic particles as adjuvants or drug delivery vehicles [42]. For example, using magnetic microparticles to augment tPA penetration into clots approximately doubles thrombolysis rates [56], a rate that can be further enhanced with the addition of ultrasound. Magnetic rod mixers can enhance the mass transfer of tPA such that fibrinolysis at lower concentrations of tPA can approach, but not exceed, that of supratherapeutic concentrations [44]. However, strategies that increase the accessibility of local tPA ultimately run up against the limit of plasminogen availability. Because our approach uses beads encapsulating iron oxide, further enhancement of fibrinolysis rate could be achieved using high frequency magnetic fields to induce local hyperthermia, which has been shown to accelerate fibrinolysis in vitro and in vivo using tPA-functionalized iron oxide nanocubes [45]. Taken together, the combination of multifunctional magnetic particles combined with dynamic magnetic fields has great potential to improve the rate of recanalization of occluded blood vessels, especially in cases like lacunar strokes where clots are not accessible to mechanical thrombectomy devices.

5.5 Materials and Methods

5.5.1 Materials

10 nm (II,III) iron oxide nanoparticles (CAS 900084), cetyltrimethylammonium bromide (CTAB, CAS 57-09-0), sodium dodecyl sulfate (SDS, CAS 151-21-3), sodium borohydride (NaBH_4 , CAS 16940-66-2), bovine serum albumin (BSA, CAS 9048-46-A), fibrinogen from human plasma (CAS 9001-32-5), and human plasminogen (SRP6518) were purchased from Sigma-Aldrich (St. Louis, MO). Ethyl acetate (142-89-2), ammonium hydroxide (1336-21-6) were obtained from Spectrum (New Brunswick, NJ). (Zeba desalting columns (89882), EZ-Link™ Sulfo-NHS-Biotin kits (A39256), Dynabeads™ MyOne™ Streptavidin T1 (65601),

tetraethyl orthosilicate (TEOS, O46174), and Alexa 555 (A20174) were obtained from Thermo Fisher Scientific (Waltham, MA). Normal pooled plasma (NPP) was purchased from George King Bio-Medical, Inc. (Overland Park, KS). Human alpha thrombin was obtained through Enzyme Research Laboratories (South Bend, IN). Recombinant human tPA was purchased from Abcam (Cambridge, UK).

5.5.2 Synthesis of magnetic mesoporous silica nanoparticles (mMSN)

Synthesis of mMSN was adapted from Suteewong et al. [57] where 15 mg of 10 nm iron oxide nanoparticles in chloroform were passivated in 54.8 mM CTAB via 5 min homogenization. The resulting emulsion was heated to 70°C for 10 min to evaporate the chloroform before being diluted 20x in 18.2 M Ω -cm DI water. Ethyl acetate, ammonium hydroxide, and TEOS at 0.062 M, 0.46 M and 0.015 M respectively were allowed to react for 8 min before being neutralized using 2 M HCl. The resulting particles were calcinated at 500 °C for 8 hr to remove the surfactant template before being resuspended in DI water with 0.1 wt% SDS. The entire reaction was carried out in a directional, no-gradient 4 mT magnetic field to bias the orientation of the iron oxide domains and maximize magnetic response. For some samples, mMSN were etched with NaBH₄ for 4 hr to increase pore diameter after neutralization.

5.5.3 Characterization of mMSN

Scanning transmission electron microscopy (STEM) images were captured using a Talos F200X microscope at an accelerating voltage of 200 keV. High-angle annular dark field energy-dispersive X-ray (HAADF-EDS) spectra were also generated. Exposure times were greater than 30 min to allow for estimation of sample composition within a 90% confidence interval. Pore size distribution was measured using a Micromeritics Tristar 3000 sorptometer and calculated

using the Barrett-Joyner-Halenda (BJH) method [58]. Magnetization was characterized in an MPMS3 Quantum Design magnetometer at 25 °C from -0.5 to 0.5 T.

5.5.4 Co-functionalization of Dynabeads™ with tPA and pgn-mMSN

To functionalize mMSN with primary amines, mMSN were incubated in 0.04 M 3-aminopropyltriethoxysilane (APS) in ethanol for 2 hr at room temperature, and then 1 hr at 80 °C [59]. The mMSN were then washed with ethanol 4 times via centrifugation at 1500g for 1 min and finally resuspended in a 1:1 mixture of water and dimethyl sulfoxide (DMSO) (pH = 4.7). Then mMSN at $10^{14}/\mu\text{L}$ were mixed with 2 mL of 0.06M biotin in DMSO under sonication for 2 hr at room temperature. The resulting solution was washed 4 times with tris-buffer solution (pH = 7.4) via centrifugation at 1500g for 1 min. After the final wash cycle, the biotinylated mMSN were resuspended with $10^7/\mu\text{L}$ beads in TBS for 4-48 hr. A magnet was used to separate the beads from the unbound mMSN in four separate washing cycles. Each time, beads with covalently attached mMSN (studded beads) were resuspended in TBS. Biotinylated tPA (200 $\mu\text{g}/\text{mL}$) was added to the solution and the studded beads allowed to incubate for 12 hr at 2 °C before four more wash cycles. Finally, the studded beads were incubated in 10 μM plasminogen in TBS for 12 hr at 4°C. Immediately before use, the resulting beads co-functionalized with tPA and pgn-mMSN (pgn-tPA-beads) were washed three times in TBS to remove excess plasminogen.

5.5.5 Magnetic field induced assembly and translation

Under the influence of a rotating magnetic field, tPA-beads and pgn-mMSN spontaneously assemble into μ wheels [53]. To direct the μ wheels to the fibrin front, a rotating AC magnetic field was generated using five air-cored solenoids (51 mm inner diameter) with 336 turns each. An analog output card (National Instruments (NI), NI-9623, Austin, TX) controlled by Matlab,

generated a current that was subsequently amplified (Behringer, EP2000, Willich, Germany). The final current passing through each coil, measured using an analog input card (NI-USB-6009), was 2 A, resulting in a field strength of 6.2 mT at the sample. The frequency of the rotating field was 10 Hz. For corkscrew experiments, the heading direction and camber angle for each magnetic field were shifted over time such that the beads followed a forward-biased spiral path with a 1 s frequency. μ Wheel velocity was tracked using brightfield microscopy on a Prior Open Stand microscope (Prior Scientific, Cambridge, UK) with a PCO Panda camera (PCO Imaging, Kelheim, Germany).

5.5.6 Loading and release of plasminogen

mMSN ($10^6/\mu\text{L}$) were incubated in a 0.5 mL solution containing 10 μM plasminogen in PBS for 24 hr. Immediately before use, the pgn-mMSN were removed from solution via centrifugation at 5000g for 5 min, washed three times in 0.5 mL PBS, and resuspended in either PBS with 0.1 wt% SDS or plasma with 1 wt% BSA. A standard curve for plasminogen absorbance at 285 nm (A285) in PBS (0-20 μM) was measured with a UV-Vis spectrophotometer (Genesys 10S, ThermoFisher). Pgn-mMSN ($10^5/\mu\text{L}$) were placed in 0.5 mL PBS. Every 5 min for 1 hr, the sample was centrifuged and the supernatant collected into a cuvette. Once the A285 was measured, the supernatant was used to resuspend the pgn-mMSN. A285 measurements were compared against a standard curve to calculate the release of plasminogen over time.

5.5.7 Biotinylation of tPA

Recombinant tPA at 200 $\mu\text{g}/\text{mL}$ was biotinylated with an EZ-Link Sulfo-NHS-Biotin kit and purified in Zeba Spin Desalting Columns according to manufacturer instructions. To prepare tPA functionalized beads (tPA-beads), 5 μL beads were incubated in 20 μL aliquots of 200

$\mu\text{g/mL}$ biotinylated tPA at $4\text{ }^\circ\text{C}$ for 12 hr (tPA-beads). Excess tPA was removed with four washes via centrifugation at 1500 g for 1 minute. tPA-beads were resuspended in TBS with 1 wt% BSA.

5.5.8 Measurement of tPA activity on functionalized beads

tPA (0.25, 0.5, 0.75 and $1\text{ }\mu\text{M}$) and tPA-beads (10^5 and $10^6/\mu\text{L}$) were incubated with excess ($100\text{ }\mu\text{M}$) fluorogenic substrate for tPA (SN-18, Haematologic Technologies Inc., Essex Junction, VT). For solvated tPA experiments, fluorescent intensity was measured in a microplate reader (Biotek Synergy H1, BioTek U.S. Winooski, VT) every minute for 1 hr. For tPA-bead experiments, the solution was rotated on a carousel to prevent bead settling. In 5 min intervals, beads were extracted from solution using a permanent magnet and the fluorescent intensity of the supernatant measured. Beads and supernatant were remixed after each measurement to ensure experimental continuity.

5.5.9 Modeling tPA and plasminogen concentrations at the lysis front

Diffusion of tPA was calculated using Fick's Law for diffusion into a semi-infinite medium (Eqn 5.1):

$$\frac{C(z,t)}{C_0} = 1 - \text{erf}\left(\frac{z}{2\sqrt{Dt}}\right). \quad (5.1)$$

$C(z, t)$ is the concentration at time t and location z of tPA, C_0 is the injected concentration, and D is the diffusion constant ($D = 5 * 10^{-11}\text{ m}^2/\text{s}$) [60]. To predict the concentrations of tPA and plasminogen over time for delivered species, we measured the velocity distribution of drug-laden pgn-tPA- μ wheels as they approached the fibrin front. μ Wheels were driven in a single direction for 60 min under a 6 mT magnetic field at 10 Hz. The velocity of each individual bead was quantified using a macro for the Fiji distribution of ImageJ with the resulting distribution $f(v)$ lognormal (Eqn 5.2) or Gaussian (Eqn 5.3):

$$f(v) = \frac{1}{v\sigma\sqrt{2\pi}} e^{-\frac{(\ln v - \mu)^2}{2\sigma^2}} \quad (5.2)$$

$$f(v) = \frac{1}{\alpha\sigma\sqrt{2\pi}} e^{-\frac{(v-\mu)^2}{2\sigma^2}}. \quad (5.3)$$

Here, μ is the arithmetic mean, σ^2 the variance, and α a parameter that accounts for skew. Given these distribution functions, the probability that μ wheels reach a point z at a given time t is:

$$p(z, t) = 1 - \int_0^{z/t} f(v) dv \quad (5.4)$$

where z is the distance in microns between the fibrin front and bead injection site (1 mm). We define a rectangular control volume encompassing the area within $w = 100 \mu\text{m}$ of the fibrin front. The concentration of beads that accumulate in that region is:

$$\frac{C(z, t)}{C_0} = \frac{1}{\Delta w} \int_L^\infty p(z, t) dz \quad (5.5)$$

where $L = 1000 \mu\text{m}$ is the distance separating the bead injection site from the fibrin front.

Concentrations of tPA and plasminogen are calculated according to the following ordinary differential equations:

$$\frac{d[Pgn^*]}{dt} = 2k_1[Pgn]^2 - k_{-1}[Pgn^*] - k_{tPA}[tPA^*][Pgn^*] \quad (5.6)$$

$$\frac{d[Pgn]}{dt} = -2k_1[Pgn]^2 + k_{-1}[Pgn^*] + A_{Pgn}R_{\mu wheels} \quad (5.7)$$

$$\frac{d[tPA^*]}{dt} = 2k_2[tPA]^2 - k_{-2}[tPA^*] \quad (5.8)$$

$$\frac{d[tPA]}{dt} = A_{tPA}R_{\mu wheels} - 2k_2[tPA]^2 + k_{-2}[tPA^*]. \quad (5.9)$$

Here, $[Pgn]$ is the concentration of free plasminogen, $[Pgn^*]$ is the concentration of plasminogen bound to fibrin, $[tPA]$ is the concentration of free tPA and $[tPA^*]$ is the concentration of tPA bound to fibrin. The rate constants k_1 and k_{-1} are the on and off rates for plasminogen binding to fibrin, and k_2 and k_{-2} are the on and off rates for tPA binding to fibrin.

k_{tPA} is the rate at which tPA converts fibrin bound plasminogen to plasmin. Rate constants have been reported as $k_1 = 1.72 \mu\text{M}^{-1}\text{s}^{-1}$, $k_{-1} = 3.8 \text{ s}^{-1}$ [61] $k_2 = 0.011 \mu\text{M}^{-1}\text{s}^{-1}$, $k_{-2} = 0.0036 \text{ s}^{-1}$ and $k_{tPA} = 0.01 \mu\text{M}^{-1}\text{s}^{-1}$ [62,63]. A_{pgn} and A_{tPA} are coefficients representing the active concentrations of plasminogen released from pgn-mMSN and tPA immobilized on tPA- μ wheels respectively and derived from experimental measurements of plasminogen release and tPA activity as described above. $R_{\mu\text{wheels}}$ is the rate of accumulation of beads at the fibrin front and is the derivative with respect to time of Eqn 5.2. When solved numerically using the Matlab *ode45* solver, these equations can be used to estimate the tPA and plasminogen concentrations over the timescale of the fibrinolysis experiments.

5.5.10 Fabrication of microfluidic devices

A template for the microfluidic channel was 3D printed using a Formlabs Form 3 printer using clear stereolithography resin (RS-F2-GPCL-04, Formlabs, Somerville, MA). The device has two inlets for the central channel ($h = 50 \mu\text{m}$) and two auxiliary inlets for the side chamber ($h = 100 \mu\text{m}$). A polydimethylsiloxane (PDMS) mold was made from the template. The PDMS was prepared using a 10:1 ratio of Sylgard 184 silicone elastomer base to curing agent (Dow Corning Corporation, Midland, MI). The mold was degassed for 1 hr in a vacuum chamber before being cured for 1 hr at 80 °C. Once cured, the mold was washed for 5 min in acetone and 5 min in ethanol in a sonicator before being air-dried. The mold and a glass slide were treated with oxygen plasma (0.2 torr) for 90 s and immediately bonded. The bonded assembly was annealed and then placed in a convection oven at 80 °C for 24 hr.

5.5.11 Fibrinolysis experiments

The geometry for the device is shown in Fig. D.2A (Appendix D). The two auxiliary inputs were plugged to prepare for injection of 30 $\mu\text{g}/\text{mL}$ of Alexa 555 labeled fibrinogen, 20 mM

CaCl₂ and 9 nM thrombin to form a fibrin gel in the right channel. The device was enclosed in a Petri dish for 30 min with a moist Kimwipe to prevent evaporation and to allow full gelation. Next, the auxiliary chamber was filled with NPP and a suspension of tPA-beads and pgn-mMSN was injected 1 mm from the fibrin front. Lysis experiments were recorded using TRITC fluorescence and brightfield microscopy through a PCO Panda camera at 5 min intervals through a 40X objective (NA 0.95, Plan APO).

5.6 References

- 1 Han K, Shields CW, Velev OD. Engineering of Self-Propelling Microbots and Microdevices Powered by Magnetic and Electric Fields. *Adv Funct Mater* 2018; **28**: 1–14.
- 2 Yang T, Tasci TO, Neeves KB, Wu N, Marr DWM. Magnetic Microlasos for Reversible Cargo Capture, Transport, and Release. *Langmuir* 2017; **33**: 5932–7.
- 3 Yang T, Sprinkle B, Guo Y, Qian J, Hua D, Donev A, Marr DWM, Wu N. Reconfigurable microbots folded from simple colloidal chains. *Proc Natl Acad Sci U S A* 2020; **117**: 18186–93.
- 4 Ma F, Wang S, Wu DT, Wu N. Electric-field-induced assembly and propulsion of chiral colloidal clusters. *Proc Natl Acad Sci* 2015; **112**: 6307–12.
- 5 Sen A, Ibele M, Hong Y, Velegol D. Chemo and phototactic nano/microbots. *Faraday Discuss* 2009; **143**: 9–14.
- 6 Aghakhani A, Yasa O, Wrede P, Sitti M. Acoustically powered surface-slipping mobile microrobots. *Proc Natl Acad Sci U S A* 2020; **117**: 3469–77.
- 7 Chen XZ, Jang B, Ahmed D, Hu C, De Marco C, Hoop M, Mushtaq F, Nelson BJ, Pané S. Small-Scale Machines Driven by External Power Sources. *Adv Mater* 2018; **30**: 1–22.
- 8 Challis LJ. Mechanisms for interaction between RF fields and biological tissue. *Bioelectromagnetics* 2005; **26**: 98–106.
- 9 Martel S. Presenting a New Paradigm in Cancer Therapy : Delivering therapeutic agents using navigable microcarriers. *IEEE Pulse* 2014; **5**: 48–55.
- 10 Schmidt CK, Medina-Sánchez M, Edmondson RJ, Schmidt OG. Engineering microrobots for targeted cancer therapies from a medical perspective. *Nat Commun Springer US*; 2020; **11**: 1–18.

- 11 Ullrich F, Bergeles C, Pokki J, Ergeneman O, Erni S, Chatzipirpiridis G, Pané S, Framme C, Nelson BJ. Mobility experiments with microrobots for minimally invasive intraocular surgery. *Investig Ophthalmol Vis Sci* 2013; **54**: 2853–63.
- 12 Li J, Li X, Luo T, Wang R, Liu C, Chen S, Li D, Yue J, Cheng SH, Sun D. Development of a magnetic microrobot for carrying and delivering targeted cells. *Sci Robot* 2018; **3**.
- 13 Tasci TO, Disharoon D, Schoeman RM, Rana K, Herson PS, Marr DWM, Neeves KB. Enhanced Fibrinolysis with Magnetically Powered Colloidal Microwheels. *Small* 2017; : 1–11.
- 14 Weisel JW. Structure of fibrin: Impact on clot stability. *J Thromb Haemost* 2007; **5**: 116–24.
- 15 Van de Werf F, Arnold AER. Intravenous tissue plasminogen activator and size of infarct, left ventricular function, and survival in acute myocardial infarction. *Br Med J* 1988; **297**: 1374–9.
- 16 Goldhaber SZ, Meyerovitz MF, Braunwald E, Green D, Vogelzang RL, Citrin P, Heit J, Sobel M, Brownell Wheeler H, Plante D, Kim H, Hopkins A, Tufte M, Stump D. Randomized controlled trial of tissue plasminogen activator in proximal deep venous thrombosis. *Am J Med* 1990; **88**: 235–40.
- 17 Levine M, Hirsh J, Weitz J, Cruickshank M, Neemeh J, Turpie AG, Gent M. A randomized trial of a single bolus dosage regimen of recombinant tissue plasminogen activator in patients with acute pulmonary embolism. *Chest* 1990; **98**: 1473–9.
- 18 Sandercock P, Wardlaw JM, Lindley RI, Dennis M, Cohen G, Murray G, Innes K, Venables G, Czlonkowska A, Kobayashi A, Ricci S, Murray V, Berge E, Slot KB, Hankey GJ, Correia M, Peeters A, Matz K, Lyrer P, Gubitz G, et al. The benefits and harms of intravenous thrombolysis with recombinant tissue plasminogen activator within 6 h of acute ischaemic stroke (the third international stroke trial [IST-3]): A randomised controlled trial. *Lancet* Elsevier Ltd; 2012; **379**: 2352–63.
- 19 Emberson J, Lees KR, Lyden P, Blackwell L, Albers G, Bluhmki E, Brott T, Cohen G, Davis S, Donnan G, Grotta J, Howard G, Kaste M, Koga M, Von Kummer R, Lansberg M, Lindley RI, Murray G, Olivot JM, Parsons M, et al. Effect of treatment delay, age, and stroke severity on the effects of intravenous thrombolysis with alteplase for acute ischaemic stroke: A meta-analysis of individual patient data from randomised trials. *Lancet* 2014; **384**: 1929–35.
- 20 Byrne RM, Taha AG, Avgerinos E, Marone LK, Makaroun MS, Chaer RA. Contemporary outcomes of endovascular interventions for acute limb ischemia. *J Vasc Surg* Elsevier Inc.; 2014; **59**: 988–95.
- 21 Hoylaerts M, Rijken DC, Lijnen HR, Collen D. Kinetics of the activation of plasminogen

- by human tissue plasminogen activator. Role of fibrin. *J Biol Chem* © 1982 ASBMB. Currently published by Elsevier Inc; originally published by American Society for Biochemistry and Molecular Biology.; 1982; **257**: 2912–9.
- 22 Francis CW, Marder VJ, Barlow GH. Plasmic degradation of crosslinked fibrin. Characterization of new macromolecular soluble complexes and a model of their structure. *J Clin Invest* 1980; **66**: 1033–43.
 - 23 Diamond SL. Engineering Design of Optimal Strategies for Blood Clot Dissolution. *Annu Rev Biomed Eng* 1999; **1**: 427–61.
 - 24 Labiche LA, Malkoff M, Alexandrov A V. Residual flow signals predict complete recanalization in stroke patients treated with TPA. *J Neuroimaging* 2003; **13**: 28–33.
 - 25 Sabovic M, Blinc A. Biochemical and biophysical conditions for blood clot lysis. *Pflugers Arch Eur J Physiol* 2000; **440**: 134–6.
 - 26 Chandler WL, Alessi MC, Aillaud MF, Henderson P, Vague P, Juhan-Vague I. Clearance of Tissue Plasminogen Activator (TPA) and TPA/Plasminogen Activator Inhibitor Type 1 (PAI-1) Complex. *Circulation* 1997; **96**: 761–8.
 - 27 von Kummer R. Early Major Ischemic Changes on Computed Tomography Should Preclude Use of Tissue Plasminogen Activator. *Stroke* 2003; **34**: 820–1.
 - 28 Henderson SJ, Weitz JI, Kim PY. Fibrinolysis: strategies to enhance the treatment of acute ischemic stroke. *J Thromb Haemost* 2018; **16**: 1932–40.
 - 29 Campbell BCV, Mitchell PJ, Churilov L, Yassi N, Kleinig TJ, Dowling RJ, Yan B, Bush SJ, Dewey HM, Thijs V, Scroop R, Simpson M, Brooks M, Asadi H, Wu TY, Shah DG, Wijeratne T, Ang T, Miteff F, Levi CR, et al. Tenecteplase versus Alteplase before Thrombectomy for Ischemic Stroke. *N Engl J Med* 2018; **378**: 1573–82.
 - 30 Logallo N, Novotny V, Assmus J, Kvistad CE, Alteheld L, Rønning OM, Thommessen B, Amthor KF, Ihle-Hansen H, Kurz M, Tobro H, Kaur K, Stankiewicz M, Carlsson M, Morsund Å, Idicula T, Aamodt AH, Lund C, Næss H, Waje-Andreassen U, et al. Tenecteplase versus alteplase for management of acute ischaemic stroke (NOR-TEST): a phase 3, randomised, open-label, blinded endpoint trial. *Lancet Neurol* 2017; **16**: 781–8.
 - 31 Sakharov D V., Nagelkerkel JF, Rijken DC. Rearrangements of the fibrin network and spatial distribution of fibrinolytic components during plasma clot lysis: Study with confocal microscopy. *J Biol Chem* © 1996 ASBMB. Currently published by Elsevier Inc; originally published by American Society for Biochemistry and Molecular Biology.; 1996; **271**: 2133–8.
 - 32 Longstaff C, Thelwell C, Williams SC, Silva MMCG, Szabó L, Kolev K. The interplay between tissue plasminogen activator domains and fibrin structures in the regulation of

- fibrinolysis: Kinetic and microscopic studies. *Blood* 2011; **117**: 661–8.
- 33 Donnan GA, Davis SM, Parsons MW, Ma H, Dewey HM, Howells DW. How to make better use of thrombolytic therapy in acute ischemic stroke. *Nat Rev Neurol* 2011; **7**: 400–9.
- 34 Wang YF, Tsirka SE, Strickland S, Stieg PE, Soriano SG, Lipton SA. Tissue plasminogen activator (tPA) increase neuronal damage after focal cerebral ischemia in wild-type and tPA-deficient mice. *Nat Med* 1998; **4**: 228–31.
- 35 Sakharov D V, Barrertt-Bergshoeff M, Hekkenberg RT, Rijken DC. Fibrin-specificity of a plasminogen activator affects the efficiency of fibrinolysis and responsiveness to ultrasound: comparison of nine plasminogen activators in vitro. *Thromb Haemost Germany*; 1999; **81**: 605–12.
- 36 Horrevoets AJG, Pannekoek H, Nesheim ME. A steady-state template model that describes the kinetics of fibrin- stimulated [Glu1]- and [Lys78]plasminogen activation by native tissue- type plasminogen activator and variants that lack either the finger or kringle-2 domain. *J Biol Chem* 1997; **272**: 2183–91.
- 37 De Vries C, Veerman H, Koornneef E, Pannekoek H. Tissue-type plasminogen activator and its substrate Glu-plasminogen share common binding sites in limited plasmin-digested fibrin. *J Biol Chem* 1990; **265**: 13547–52.
- 38 Jung He Wu, Diamond SL. Tissue plasminogen activator (tPA) inhibits plasmin degradation of fibrin: A mechanism that slows tPA-mediated fibrinolysis but does not require α 2- antiplasmin or leakage of intrinsic plasminogen. *J Clin Invest* 1995; **95**: 2483–90.
- 39 Kim PY, Tieu LD, Stafford AR, Fredenburgh JC, Weitz JI. A high affinity interaction of plasminogen with fibrin is not essential for efficient activation by tissue-type plasminogen activator. *J Biol Chem* 2012; **287**: 4652–61.
- 40 Onundarson PT, Francis CW, Marder VJ. Depletion of plasminogen in vitro or during thrombolytic therapy limits fibrinolytic potential. *J Lab Clin Med United States*; 1992; **120**: 120–8.
- 41 Baeten KM, Richard MC, Kanse SM, Mutch NJ, Degen JL, Booth NA. Activation of single-chain urokinase-type plasminogen activator by platelet-associated plasminogen: A mechanism for stimulation of fibrinolysis by platelets. *J Thromb Haemost* 2010; **8**: 1313–22.
- 42 Disharoon D, Marr DWM, Neeves KB. Engineered microparticles and nanoparticles for fibrinolysis. *J Thromb Haemost* 2019; **17**: 2004–15.
- 43 Hu J, Huang W, Huang S, ZhuGe Q, Jin K, Zhao Y. Magnetically active Fe₃O₄ nanorods

- loaded with tissue plasminogen activator for enhanced thrombolysis. *Nano Res* 2016; **9**: 2652–61.
- 44 Huang L, ZhuGe Q, Cheng R, Zhao Y, Mao L, Yang B, Jin K, Huang W. Acceleration of Tissue Plasminogen Activator-Mediated Thrombolysis by Magnetically Powered Nanomotors. *ACS Nano* 2014; **8**: 7746–54.
- 45 Voros E, Cho M, Ramirez M, Palange AL, De Rosa E, Key J, Garami Z, Lumsden AB, Decuzzi P. TPA Immobilization on Iron Oxide Nanocubes and Localized Magnetic Hyperthermia Accelerate Blood Clot Lysis. *Adv Funct Mater* 2015; **25**: 1709–18.
- 46 Chen JP, Yang PC, Ma YH, Wu T. Characterization of chitosan magnetic nanoparticles for in situ delivery of tissue plasminogen activator. *Carbohydr Polym* Elsevier Ltd.; 2011; **84**: 364–72.
- 47 Ma YH, Wu SY, Wu T, Chang YJ, Hua MY, Chen JP. Magnetically targeted thrombolysis with recombinant tissue plasminogen activator bound to polyacrylic acid-coated nanoparticles. *Biomaterials* Elsevier Ltd; 2009; **30**: 3343–51.
- 48 Yang HW, Hua MY, Lin KJ, Wey SP, Tsai RY, Wu SY, Lu YC, Liu HL, Wu T, Ma YH. Bioconjugation of recombinant tissue plasminogen activator to magnetic nanocarriers for targeted thrombolysis. *Int J Nanomedicine* 2012; **7**: 5159–73.
- 49 Rijken DC, Sakharov D V. Basic principles in thrombolysis: Regulatory role of plasminogen. *Thromb Res* 2001; **103**: 41–9.
- 50 Deodhar G V., Adams ML, Joardar S, Joglekar M, Davidson M, Smith WC, Mettler M, Toler SA, Davies FK, Williams SKR, Trewyn BG. Conserved Activity of Reassociated Homotetrameric Protein Subunits Released from Mesoporous Silica Nanoparticles. *Langmuir* 2018; **34**: 228–33.
- 51 Martin-Ortigosa S, Peterson DJ, Valenstein JS, Lin VSY, Trewyn BG, Alexander Lyznik L, Wang K. Mesoporous silica nanoparticle-mediated intracellular cre protein delivery for maize genome editing via loxP site excision. *Plant Physiol* 2014; **164**: 537–47.
- 52 Martin-Ortigosa S, Valenstein JS, Lin VSY, Trewyn BG, Wang K. Gold functionalized mesoporous silica nanoparticle mediated protein and DNA codelivery to plant cells via the biolistic method. *Adv Funct Mater* 2012; **22**: 3576–82.
- 53 Tasci TO, Herson PS, Neeves KB, Marr DWM. Surface-enabled propulsion and control of colloidal microwheels. *Nat Commun* Nature Publishing Group; 2016; **7**: 10225.
- 54 Disharoon D, Neeves KB, Marr DWM. Ac/dc Magnetic Fields for Enhanced Translation of Colloidal Microwheels. *Langmuir* American Chemical Society; 2019; **35**: 3455–60.
- 55 Bannish BE, Keener JP, Fogelson AL. Modelling fibrinolysis: A 3D stochastic multiscale

- model. *Math Med Biol* 2014; **31**: 17–44.
- 56 Torno MD, Kaminski MD, Xie Y, Meyers RE, Mertz CJ, Liu X, O'Brien WD, Rosengart AJ. Improvement of in vitro thrombolysis employing magnetically-guided microspheres. *Thromb Res* 2008; **121**: 799–811.
- 57 Suteewong T, Sai H, Lee J, Bradbury M, Hyeon T, Gruner SM, Wiesner U. Ordered mesoporous silica nanoparticles with and without embedded iron oxide nanoparticles: Structure evolution during synthesis. *J Mater Chem* 2010; **20**: 7807–14.
- 58 Barrett EP, Joyner LG, Halenda PP. The Determination of Pore Volume and Area Distributions in Porous Substances. I. Computations from Nitrogen Isotherms. *J Am Chem Soc* 1951; **73**: 373–80.
- 59 Corricelli M, Depalo N, Di Carlo E, Fanizza E, Laquintana V, Denora N, Agostiano A, Striccoli M, Curri ML. Biotin-decorated silica coated PbS nanocrystals emitting in the second biological near infrared window for bioimaging. *R Soc Chem* 2013; **00**: 1–10.
- 60 Weigandt KM, White N, Chung D, Ellingson E, Wang Y, Fu X, Pozzo DC. Fibrin Clot Structure and Mechanics Associated with Specific Oxidation of Methionine Residues in Fibrinogen. *Biophys J* 2012; **103**: 2399–407.
- 61 Wiman B, Collen D. On the mechanism of the reaction between human α 2-antiplasmin and plasmin. *J Biol Chem* 1979; **84**: 573–8.
- 62 Tiefenbrunn AJ, Graor RA, Robison AK, Lucas F V., Hotchkiss A, Sobel BE. Pharmacodynamics of tissue-type plasminogen activator characterized by computer-assisted simulation. *Circulation* 1986; **73**: 1291–9.
- 63 Bannish BE, Chernysh IN, Keener JP, Fogelson AL, Weisel JW. Molecular and Physical Mechanisms of Fibrinolysis and Thrombolysis from Mathematical Modeling and Experiments. *Sci Rep Springer US*; 2017; **7**: 1–11.

CHAPTER 6

CONCLUSION AND RECOMMENDATIONS

6.1 Summary

Thrombolytic therapy has been touted as an effective replacement or complement to thrombectomy; however, despite the prevalence of cardiovascular disease, the only significant advancements in clinical thrombolysis since the 1990's have been the development of alternative recombinant tissue plasminogen activator (tPA) products (alteplase, reteplase, tenecteplase) [1]. Researchers and clinicians have identified the challenges preventing widespread implementation of thrombolytic recanalization: 1) slow transport of tPA to a blood clot, 2) rapid deactivation of exogenous tPA, and 3) risk of hemorrhage [2]. To overcome these challenges, various schemes have been introduced which seek to swiftly target high concentrations of tPA to blood clots while keeping systemic concentrations low to prevent bleeding [2,3]. The most promising approach is to deliver tPA using magnetic-driven drug delivery vehicles. To that end, we develop a drug-delivery strategy using our lab's patented microwheels (μ wheels), which are summarized in Chapter 2.

In Chapter 3, we investigate methods of controlling μ wheel behavior, and find that the separation gap between μ wheels and a surface is an important parameter controlling their rolling velocity [4]. Small changes in load force and zeta potential can affect the gap width and control translation. μ Wheels roll with stick-slip behavior, where they roll faster in the "stick" regime because of moments of contact friction, which serves as a superior propellant compared to the lubrication wet friction of the "slip" regime.

In Chapter 4 (Appendix B), we use the μ wheels to degrade fibrin gels in plasma and find that μ wheels bearing a low concentration of tPA (tPA- μ wheels) degrade fibrin twofold more

quickly than high concentrations of soluble tPA [5]. Moreover, we demonstrate magnetic targeting of tPA- μ wheels. Via targeting, the concentration of tPA is increased fifty-fold over the course of 30 min. We also develop a novel magnetic control strategy which drives tPA- μ wheels along a corkscrew trajectory, helping tPA- μ wheels to penetrate and degrade fibrin clots more quickly. Finally, we demonstrate the lysis of a platelet-rich clot formed from whole blood, establishing the viability of tPA- μ wheels as a thrombolytic agent even in the presence of endogenous tPA inhibitors.

The concentrations of tPA localized in Appendix B are so high that the lysis rates become substrate-limited. Therefore, in Chapter 5 we develop a strategy to co-deliver tPA with its substrate, plasminogen [6]. DynabeadsTM are covalently decorated with mesoporous silica nanoparticles (MSN) which are subsequently loaded with plasminogen. The resulting colloids (pgn-tPA- μ wheels) simultaneously deliver tPA and its substrate. Moreover, by adjusting the ratio of MSN to DynabeadsTM, we tune the biochemical environment to be favorable for rapid fibrinolysis, showing a twenty-fold increase in lysis rates relative to therapeutic concentrations of free tPA. This has potential impact in the field of drug delivery, as it offers a modular and tunable method to deliver multiple molecules without increasing complexity.

The work presented in this thesis highlights the early development of a technology that is many years from clinical implementation. What follows is a list of recommendations for future studies which will facilitate the translation of this work to animal models and beyond.

6.2 Outlook and recommendations

6.2.1 Modular co-delivery for different clot morphologies

A powerful feature of the co-delivery vehicles used in Chapter 5 is their versatility and adaptability. MSN with various pore sizes could be developed to co-deliver tPA with molecules

other than plasminogen. Moreover, different populations of tPA- μ wheels decorated with MSN containing distinct molecules could be mixed to control the concentrations of three or more drugs. Such polydispersions could be used to treat blood clots that resist lysis by tPA alone.

6.2.1.1 Remediating exclusion of plasminogen from retracted clots

Arterial blood clots that form as the result of platelet activation retract and can shrink by as much as 90% [17]. Retraction is initiated by platelets and propagated through the fibrin network. During retraction, erythrocytes and plasma within the clot are excluded, resulting in a clot composed primarily of fibrin and platelets [18]. This kind of clot is highly resistant to fibrinolytic therapy. One explanation is that the center of the clot is stabilized by platelets which cannot be removed by tPA. An alternative hypothesis is that clot retraction excludes almost all plasminogen internal to the clot, preventing the initiation and propagation of fibrinolysis by tPA [19,20]. The co-delivery strategy presented in Chapter 5 could provide an effective approach to treating such clots.

6.2.1.2 μ Wheels targeted to platelets

Blood clots typically form in phases, beginning as “white clots” composed primarily of fibrin and platelets and transitioning over time to “red clots” proliferated by erythrocytes [7]. tPA and its derivatives achieve recanalization in 30% of patients whose clots are characterized as fibrin-rich [8], but only 6% of patients with platelet-rich clots [9]. Platelet-rich thrombi have been shown to resist reperfusion via IV tPA in beagles and rabbits [10], whereas erythrocyte-rich clots are more susceptible to lysis by tPA [11].

Platelet-rich thrombi resist tPA lysis because they are stabilized in part by von Willebrand factor (VWF), a protein that promotes platelet aggregation [12]. Two drugs in particular are efficient at degrading VWF bonds: ADAMTS13, a peptide that cleaves VWF

directly [13–15], and N-acetylcysteine (NAC), which reduces the disulfide bonds that chain VWF molecules together [16]. The MSN developed in Chapter 5 could be modified to contain ADAMTS13, NAC, or both. Then, different cocktails of tPA, plasminogen, NAC, and ADAMTS13 could conceivably be delivered to treat different types of blood clots.

6.2.1.3 μ Wheels targeted to deoxyribonucleic acid (DNA)

Platelet activation can interact with the immune system to create neutrophil extracellular traps (NETs), which have antimicrobial effects but can also cause clotting via thrombin activation [17]. NETs can provide additional structural stabilization in older clots like deep vein thrombi [18] and hematomas [19], but have also been observed in acute ischemic stroke [20]. Fibrinolysis is inhibited by NETs, and it has been shown that DNA-ase, an enzyme that degrades DNA, delivered in conjunction with tPA restores effective lysis [19,20]. This is another potential indication for thrombolytic co-delivery.

6.2.2 Materials design

6.2.2.1 Biocompatibility

Whether a material is biocompatible depends on several factors, including its size, surface chemistry, its injection and target sites within the anatomy, and the length of time surrounding tissues will be exposed to it [21]. For drug delivery vehicles, the nature and concentration of the drug and the concentration of particles must also be considered. The materials used for μ wheels were polystyrene and silica. Polystyrene is mostly benign, but sub-micron spheres have nonetheless been shown to induce minor cellular immune responses [22]. Similarly, silica in MSN is considered nonharmful but can be toxic depending on size, concentration, and surface chemistry [23]. Endocrinologic and pharmacokinetic studies will be essential in determining the biocompatibility of tPA- μ wheels. One popular approach at

improving the biocompatibility of materials is to coat them in poly-ethylene glycol (PEG), which reduces their interactions with cells. For tPA- μ wheels, this approach would have the additional benefit of protecting the tPA from deactivation.

6.2.2.2 Ternary complex between immobilized tPA, plasminogen and fibrin

To some extent, it is surprising that the surface immobilization of tPA does not significantly impair its ability to activate plasminogen. Liquid-phase tPA is an inefficient enzyme until it forms a ternary complex with plasminogen and fibrin [24,25], where its activity increases by two to three orders of magnitude [26]. It seems likely that fixing tPA to the surface of colloids would inhibit its ability to complex with plasminogen and fibrin. However, immobilizing tPA on the surface of micro- and nanoparticles has become common practice in the literature [27–32] with most papers reporting that immobilized tPA retains >70% of its enzymatic activity. More surprising still is that covering the tPA with a layer of dextran, PEG, polyacrylic acid, or poly(lactic-co-glycolic acid) (PLGA) to “stealth” the tPA, or protect it from deactivation by PAI-1 and PAI-2, does not significantly decrease its activity [33–36]. Berger and Pizzo even reported that PEGylating tPA increased its activity relative to the solvated enzyme in mouse, rat, and beagle blood [37].

In our work, we fix tPA to the surface of colloids using biotin, which covalently binds to primary amines in lysine residues. tPA is a good candidate for biotinylation because its only lysine binding site occurs on the Kringle 2 domain [38], which is distal from the serine proteolytic domain that activates plasminogen [39,40]. Using this strategy, we find that immobilized tPA retains 53-74% of its activity as quantified using a fluorogenic substrate. If tPA cannot bind to fibrin because of its association with μ wheels, then the activity should decrease to as little as 1%. It remains unclear why the activity is so moderately affected by immobilization.

One possible explanation is that the tPA on the surface of tPA- μ wheels binds with fibrin degradation products (FDPs). When delivering tPA- μ wheels, we observe a lag time before lysis rates accelerate to maximum speeds at the beginning of experiments. We have attributed this to the time it takes to accumulate large concentrations of tPA near the clot, but it may also occur because tPA works inefficiently at the beginning of experiments when it cannot readily bind to FDPs. Once fibrinolysis has been initiated and FDPs are plentiful, tPA converts plasmin more rapidly, and lysis rates increase.

An alternative hypothesis is that tPA always acts as an inefficient enzyme when fixed to μ wheel surfaces, and that fibrinolysis only proceeds so rapidly because μ wheel-targeting results in such high local concentrations of tPA. Yet a third possible explanation is that plasminogen adsorbs to tPA- μ wheel surfaces and co-localizes with tPA. From this perspective, the μ wheel surface performs the same role as fibrin as the scaffolding for the ternary complex, but with less efficiency. This is especially likely for pgn-tPA- μ wheels, where the plasminogen is being released locally at high concentrations. Understanding the exact nature of the interactions between immobilized tPA, plasminogen, FDPs and fibrin would help optimize delivery strategies.

6.2.2.3 Controlled release

The pores of MSN have been capped by chemically cleavable bonds to control the release of genes and therapeutics [41,42]. Separately, a plasmin-cleavable peptide has also been engineered to control the release of morphogenes [43]. To control the delivery of fibrinolytics, it would be extremely useful to develop MSN with plasmin-cleavable caps. Since plasmin is almost immediately inhibited by antiplasmin in the blood [44], the plasmin-cleavable caps would only be removed at the site of fibrinolysis, where tPA is actively creating plasmin. Thus the

control and yield of drugs delivered in conjunction with tPA- μ wheels could be dramatically improved.

6.2.3 Hyperthermia

Voros et al. demonstrated lysis rates three orders of magnitude faster than free tPA by inducing magnetic hyperthermia in nanocubes [45]. While such impressive lysis rates have never been reproduced, the potential for accelerating fibrinolysis using magnetic hyperthermia is clearly evident. Given that the delivery of tPA- μ wheels decorated with plasminogen-loaded MSN (p_{gn}-tPA- μ wheels) in Chapter 5 approaches the limit of what is achievable with fibrinolytic agents, it will become necessary to combine biochemical and mechanical approaches to further enhance lysis rates. Hyperthermia could also be used to trigger or accelerate the release of plasminogen (or other molecules) from MSN.

6.3 Conclusion

μ Wheels offer a tunable and modular co-delivery strategy that degrades fibrin clots thirty-fold faster than free tPA. The technique is adaptable and creates opportunities to develop therapies for clot morphologies recalcitrant to tPA such as retracted, platelet-rich, and NET-stabilized clots. Combining biological and mechanical action via corkscrew manipulation, hyperthermia, or sonothrombolysis is the way to enhance lysis moving forward. In ischemic environments where tissue can become necrotic within minutes, every second counts.

6.4 References

- 1 Bivard A, Lin L, Parsons MW. Review of Stroke Thrombolytics. *J Stroke* 2013; **15**: 90.
- 2 Disharoon D, Marr DWM, Neeves KB. Engineered microparticles and nanoparticles for fibrinolysis. *J Thromb Haemost* 2019; **17**: 2004–15.
- 3 Absar S, Gupta N, Nahar K, Ahsan F. Engineering of plasminogen activators for targeting to thrombus and heightening thrombolytic efficacy. *J Thromb Haemost* 2015; **13**: 1545–56.

- 4 Disharoon D, Neeves KB, Marr DWM. Ac/dc Magnetic Fields for Enhanced Translation of Colloidal Microwheels. *Langmuir* American Chemical Society; 2019; **35**: 3455–60.
- 5 Tasci TO, Disharoon D, Schoeman RM, Rana K, Herson PS, Marr DWM, Neeves KB. Enhanced Fibrinolysis with Magnetically Powered Colloidal Microwheels. *Small* 2017; **1700954**: 1–11.
- 6 Disharoon D, Trewyn BG, Herson PS, Marr DWM, Neeves KB. Breaking the fibrinolytic speed limit with microwheel co-delivery of tissue plasminogen activator and plasminogen. *BioRxiv* 2021.
- 7 Simons N, Mitchell P, Dowling R, Gonzales M, Yan B. Thrombus composition in acute ischemic stroke: A histopathological study of thrombus extracted by endovascular retrieval. *J Neuroradiol* Elsevier Masson SAS; 2015; **42**: 86–92.
- 8 Bhatia R, Hill MD, Shobha N, Menon B, Bal S, Kochar P, Watson T, Goyal M, Demchuk AM. Low Rates of Acute Recanalization With Intravenous Recombinant Tissue Plasminogen Activator in Ischemic Stroke. *Stroke* 2010; **41**: 2254–8.
- 9 Pikijsa S, Magdic J, Trkulja V, Unterkreuter P, Mutzenbach JS, Novak HF, Weymayr F, Hauer L, Sellner J. Intracranial thrombus morphology and composition undergoes time-dependent changes in acute ischemic stroke: A CT densitometry study. *Int J Mol Sci* 2016; **17**: 1–12.
- 10 Yasuda T, Gold HK, Leinbach RC, Saito T, Guerrero JL, Jang IK, Holt R, Fallon JT, Collen D. Lysis of plasminogen activator-resistant platelet-rich coronary artery thrombus with combined bolus injection of recombinant tissue-type plasminogen activator and antiplatelet GPIIb/IIIa antibody. *J Am Coll Cardiol* 1990; **16**: 1728–35.
- 11 Jang IK, Gold HK, Ziskind AA, Fallon JT, Holt RE, Leinbach RC, May JW, Collen D. Differential sensitivity of erythrocyte-rich and platelet-rich arterial thrombi to lysis with recombinant tissue-type plasminogen activator. A possible explanation for resistance to coronary thrombolysis. *Circulation* 1989; **79**: 920–8.
- 12 Buchtele N, Schwameis M, Gilbert JC, Schörghofer C, Jilma B. Targeting von Willebrand Factor in Ischaemic Stroke : Focus on Clinical Evidence. 2018; .
- 13 Aponte-Santamaría C, Lippok S, Mittag JJ, Obser T, Schneppenheim R, Baldauf C, Gräter F, Budde U, Rädler JO. Mutation G1629E Increases von Willebrand Factor Cleavage via a Cooperative Destabilization Mechanism. *Biophys J* 2017; **112**: 57–65.
- 14 Denorme F, Desender L, Vandenbulcke A, Deckmyn H, Vanhoorelbeke K, De Meyer SF, Langhauser F, Kleinschnitz C, Rottensteiner H, Plaimauer B, Scheiflinger F, François O, Andersson T. ADAMTS13-mediated thrombolysis of t-PA-resistant occlusions in ischemic stroke in mice. *Blood* 2016; **127**: 2337–45.

- 15 Bustamante A, Ning MM, García-Berrocso T, Penalba A, Boada C, Simats A, Pagola J, Ribó M, Molina C, Lo E, Montaner J. Usefulness of ADAMTS13 to predict response to recanalization therapies in acute ischemic stroke. *Neurology* 2018; **90**: e995–1004.
- 16 De Lizarrondo SM, Gakuba C, Herbig BA, Repessé Y, Ali C, Denis C V., Lenting PJ, Touzé E, Diamond SL, Vivien D, Gauberti M. Potent thrombolytic effect of N-acetylcysteine on arterial thrombi. *Circulation* 2017; **136**: 646–60.
- 17 Zucoloto AZ, Jenne CN. Platelet-Neutrophil Interplay: Insights Into Neutrophil Extracellular Trap (NET)-Driven Coagulation in Infection. *Front Cardiovasc Med* 2019; **6**: 1–8.
- 18 Fuchs TA, Brill A, Wagner DD. Neutrophil extracellular trap (NET) impact on deep vein thrombosis. *Arterioscler Thromb Vasc Biol* 2012; **32**: 1777–83.
- 19 Tan Q, Guo P, Zhou J, Zhang J, Zhang B, Lan C, Xian J, Ge M, Feng H, Chen Z. Targeting neutrophil extracellular traps enhanced tPA fibrinolysis for experimental intracerebral hemorrhage. *Transl Res* Elsevier Inc.; 2019; **211**: 139–46.
- 20 Laridan E, Denorme F, Desender L, François O, Andersson T, Deckmyn H, Vanhoorelbeke K, De Meyer SF. Neutrophil extracellular traps in ischemic stroke thrombi. *Ann Neurol* 2017; **82**: 223–32.
- 21 Williams DF. On the mechanisms of biocompatibility. *Biomaterials* 2008; **29**: 2941–53.
- 22 Hwang J, Choi D, Han S, Jung SY, Choi J, Hong J. Potential toxicity of polystyrene microplastic particles. *Sci Rep* 2020; **10**: 1–12.
- 23 Asefa T, Tao Z. Biocompatibility of Mesoporous Silica Nanoparticles. *Chem Res Toxicol* 2012; **25**: 2265–84.
- 24 De Vries C, Veerman H, Koornneef E, Pannekoek H. Tissue-type plasminogen activator and its substrate Glu-plasminogen share common binding sites in limited plasmin-digested fibrin. *J Biol Chem* 1990; **265**: 13547–52.
- 25 Hoylaerts M, Rijken DC, Lijnen HR, Collen D. Kinetics of the activation of plasminogen by human tissue plasminogen activator. Role of fibrin. *J Biol Chem* © 1982 ASBMB. Currently published by Elsevier Inc; originally published by American Society for Biochemistry and Molecular Biology.; 1982; **257**: 2912–9.
- 26 Horrevoets AJG, Pannekoek H, Nesheim ME. A steady-state template model that describes the kinetics of fibrin- stimulated [Glu1]- and [Lys78]plasminogen activation by native tissue- type plasminogen activator and variants that lack either the finger or kringle-2 domain. *J Biol Chem* 1997; **272**: 2183–91.

- 27 Heid S, Unterweger H, Tietze R, Friedrich RP, Weigel B, Cicha I, Eberbeck D, Boccaccini AR, Alexiou C, Lyer S. Synthesis and Characterization of Tissue Plasminogen Activator — Functionalized Superparamagnetic Iron Oxide Nanoparticles for Targeted Fibrin Clot Dissolution. *Int J Mol Sci* 2017; **18**: 1–21.
- 28 Chen JP, Yang PC, Ma YH, Wu T. Characterization of chitosan magnetic nanoparticles for in situ delivery of tissue plasminogen activator. *Carbohydr Polym* Elsevier Ltd.; 2011; **84**: 364–72.
- 29 Chen JP, Yang PC, Ma YH, Tu SJ, Lu YJ. Targeted delivery of tissue plasminogen activator by binding to silica-coated magnetic nanoparticle. *Int J Nanomedicine* 2012; **7**: 5137–49.
- 30 Tadayon A, Jamshidi R, Esmaeili A. Delivery of tissue plasminogen activator and streptokinase magnetic nanoparticles to target vascular diseases. *Int J Pharm* Elsevier B.V.; 2015; **495**: 428–38.
- 31 Hu J, Huang W, Huang S, ZhuGe Q, Jin K, Zhao Y. Magnetically active Fe₃O₄ nanorods loaded with tissue plasminogen activator for enhanced thrombolysis. *Nano Res* 2016; **9**: 2652–61.
- 32 Friedrich RP, Zaloga J, Schreiber E, Tóth IY, Tombácz E, Lyer S, Alexiou C. Tissue Plasminogen Activator Binding to Superparamagnetic Iron Oxide Nanoparticle—Covalent Versus Adsorptive Approach. *Nanoscale Res Lett* Nanoscale Research Letters; 2016; **11**: 1–11.
- 33 Torno MD, Kaminski MD, Xie Y, Meyers RE, Mertz CJ, Liu X, O’Brien WD, Rosengart AJ. Improvement of in vitro thrombolysis employing magnetically-guided microspheres. *Thromb Res* 2008; **121**: 799–811.
- 34 Yang HW, Hua MY, Lin KJ, Wey SP, Tsai RY, Wu SY, Lu YC, Liu HL, Wu T, Ma YH. Bioconjugation of recombinant tissue plasminogen activator to magnetic nanocarriers for targeted thrombolysis. *Int J Nanomedicine* 2012; **7**: 5159–73.
- 35 Drozdov AS, Vinogradov V V., Dudanov IP, Vinogradov V V. Leach-proof magnetic thrombolytic nanoparticles and coatings of enhanced activity. *Sci Rep* Nature Publishing Group; 2016; **6**: 1–8.
- 36 Ma YH, Wu SY, Wu T, Chang YJ, Hua MY, Chen JP. Magnetically targeted thrombolysis with recombinant tissue plasminogen activator bound to polyacrylic acid-coated nanoparticles. *Biomaterials* Elsevier Ltd; 2009; **30**: 3343–51.
- 37 Berger Jr H, Pizzo S V. Preparation of Polyethylene Glycol-Tissue Plasminogen Activator Adducts That Retain Functional Activity: Characteristics and Behavior in Three Animal Species. *Blood* 1988; **71**: 1641–7.

- 38 Fredriksson L, Li H, Fieber C, Li X, Eriksson U. Tissue plasminogen activator is a potent activator of PDGF-CC. *EMBO J* 2004; **23**: 3793–802.
- 39 Kim HK, Lee SY, Oh HK, Kang BH, Ku HJ, Lee Y, Shin JY, Hong YK, Joe YA. Inhibition of endothelial cell proliferation by the recombinant kringle domain of tissue-type plasminogen activator. *Biochem Biophys Res Commun* 2003; **304**: 740–6.
- 40 Chevilly A, Lesept F, Lenoir S, Ali C, Parcq J, Vivien D. Impacts of tissue-type plasminogen activator(tPA) on neuronal survival. *Front Cell Neurosci* 2015; **9**.
- 41 Lai CY, Trewyn BG, Jeftinija DM, Jeftinija K, Xu S, Jeftinija S, Lin VSY. A mesoporous silica nanosphere-based carrier system with chemically removable CdS nanoparticle caps for stimuli-responsive controlled release of neurotransmitters and drug molecules. *J Am Chem Soc* 2003; **125**: 4451–9.
- 42 Zhao Y, Vivero-Escoto JL, Slowing II, Trewyn BG, Lin VS-Y. Capped mesoporous silica nanoparticles as stimuli-responsive controlled release systems for intracellular drug/gene delivery. *Expert Opin Drug Deliv* Taylor & Francis; 2010; **7**: 1013–29.
- 43 Kader S, Monavarian M, Barati D, Moeinzadeh S, Makris TM, Jabbari E. Plasmin-Cleavable Nanoparticles for On-Demand Release of Morphogens in Vascularized Osteogenesis. *Biomacromolecules* 2019; **20**: 2973–88.
- 44 Banbula A, Zimmerman TP, Novokhatny V V. Blood inhibitory capacity toward exogenous plasmin. *Blood Coagul Fibrinolysis* 2007; **18**.
- 45 Voros E, Cho M, Ramirez M, Palange AL, De Rosa E, Key J, Garami Z, Lumsden AB, Decuzzi P. TPA Immobilization on Iron Oxide Nanocubes and Localized Magnetic Hyperthermia Accelerate Blood Clot Lysis. *Adv Funct Mater* 2015; **25**: 1709–18.

APPENDIX A

SUPPLEMENTARY MATERIALS FOR CHAPTER 3

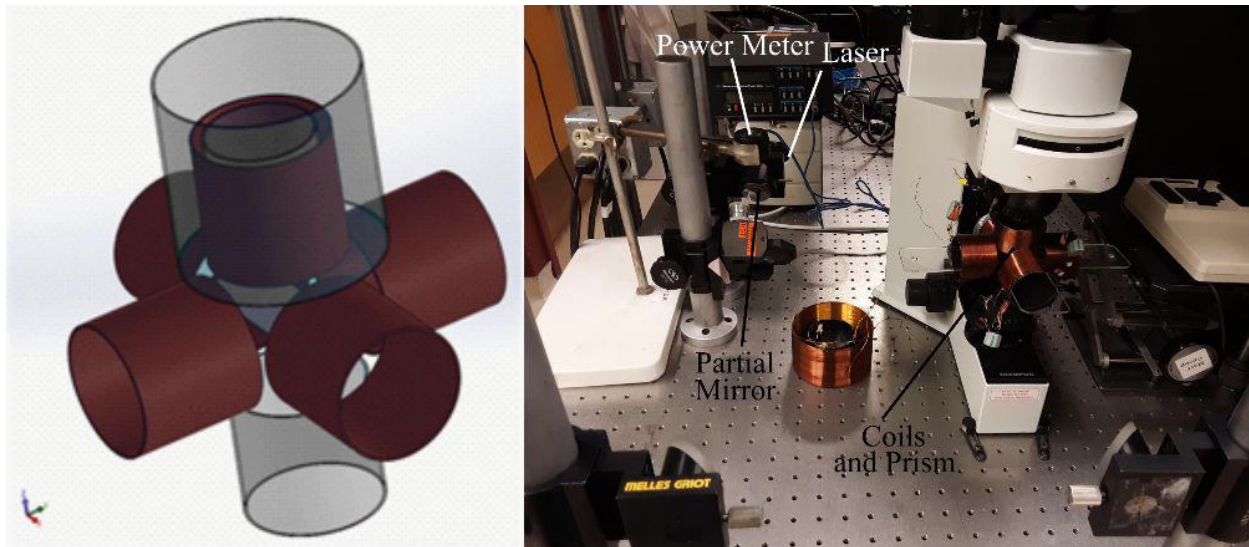


Figure A.1: Left: Schematic of coils used to produce AC and DC magnetic fields. Brown coils produce AC rotating magnetic field while transparent gray coils produce DC fields to vary loads in the direction parallel to the gravitational field. Right: Experimental apparatus.

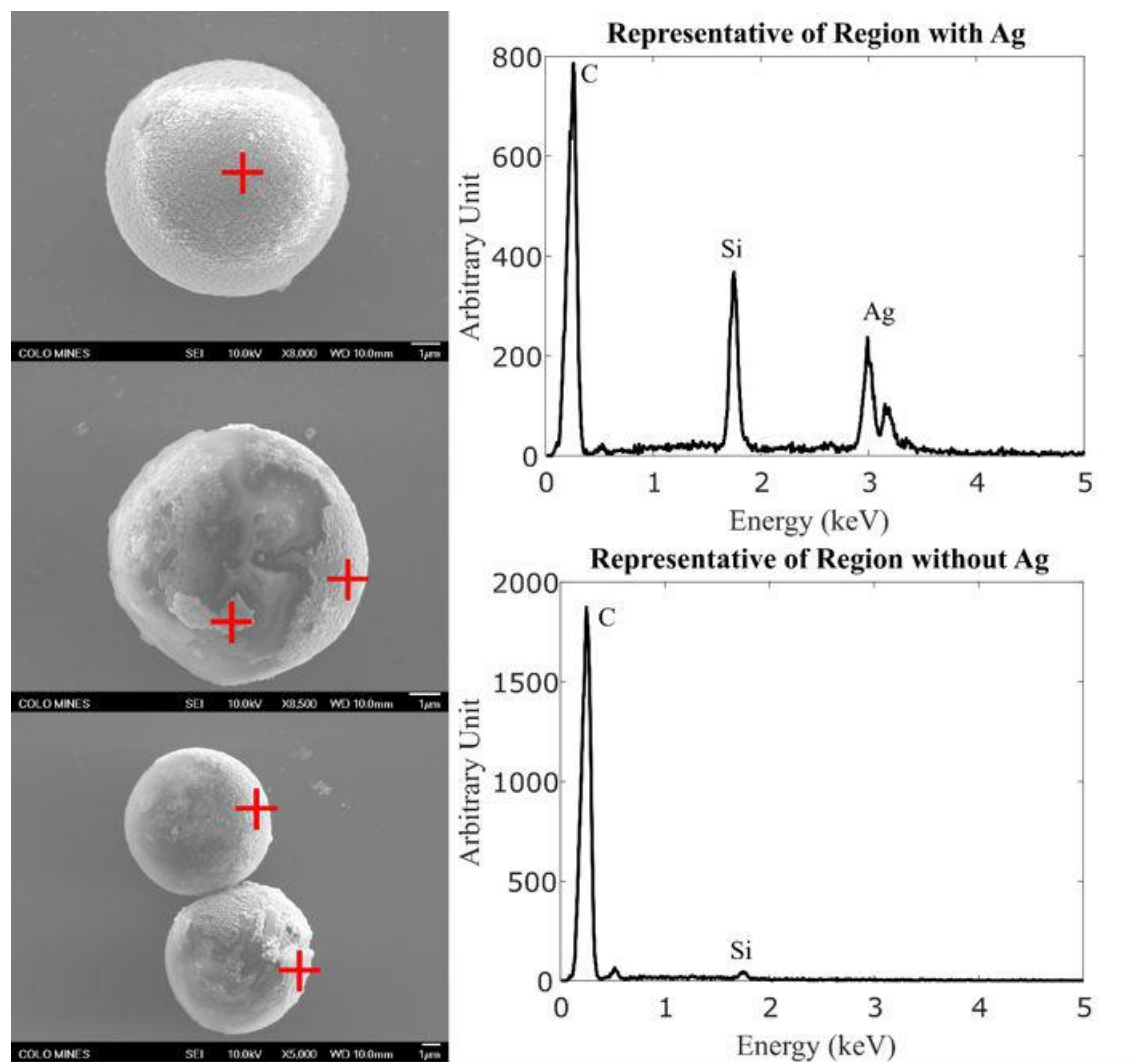


Figure A.2: Electron micrographs of Ag Janus particles. Red crosses indicate regions with Ag. Representative EDX results for Ag and normal hemispheres. The carbon peak comes from the polystyrene and the silicon peak from the wafer substrate.

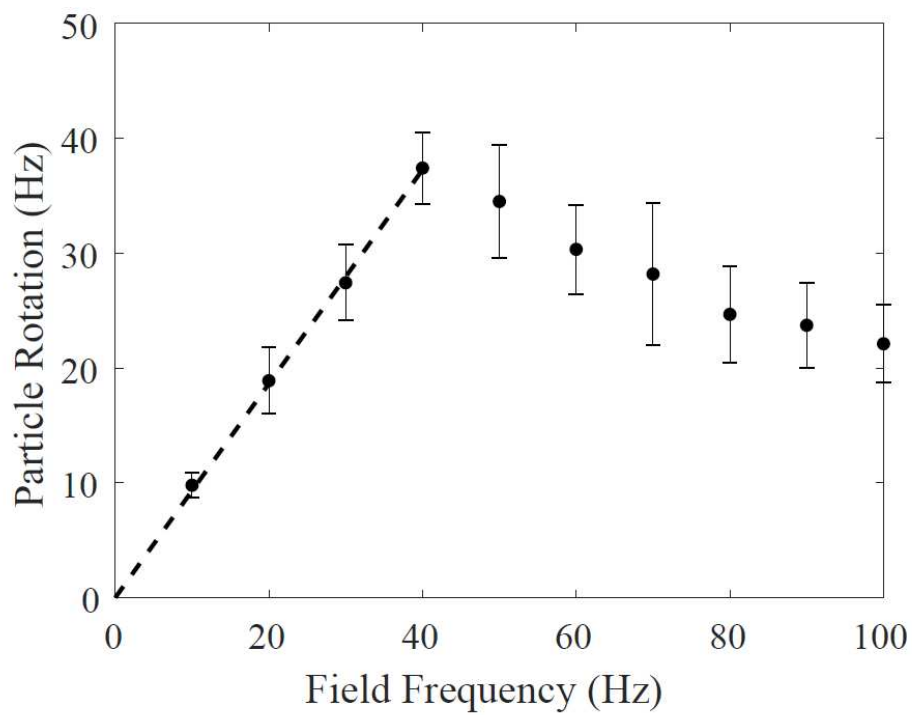


Figure A.3: Particle rotation rate measured on Ag-coated Janus particles as a function of applied AC field frequency. The particle rotation rate equals the field frequency up to ~40 Hz.

APPENDIX B

ENHANCED FIBRINOLYSIS WITH MAGNETICALLY POWERED COLLOIDAL
MICROWHEELS

This appendix is adapted with permission from

*Small*⁹

Tonguc O. Tasci¹⁰, Dante Disharoon¹¹, Rogier M. Schoeman¹², Kuldeepsinh Rana¹³, Paco S.
Herson¹⁴, David W.M. Marr¹⁵, and Keith B. Neeves¹⁶

B.1 Abstract

Thrombi that occlude blood vessels can be resolved with fibrinolytic agents that degrade fibrin, the polymer that forms between and around platelets to provide mechanical stability. Fibrinolysis rates however are often constrained by transport-limited delivery to and penetration of fibrinolytics into the thrombus. Here, these limitations are overcome with colloidal microwheel (μ wheel) assemblies functionalized with the fibrinolytic tissue-type plasminogen activator (tPA) that assemble, rotate, translate, and eventually disassemble via applied magnetic fields. These microwheels lead to rapid fibrinolysis by delivering a high local concentration of tPA to induce surface lysis and, by taking advantage of corkscrew motion, mechanically penetrating into fibrin gels and platelet-rich thrombi to initiate bulk degradation. Fibrinolysis of

⁹ Reprinted with permission from: Tasci TO, Disharoon D, Schoeman RM, Rana K, Herson PS, Marr DWM, Neeves KB. Enhanced Fibrinolysis with Magnetically Powered Colloidal Microwheels. *Small* 2017; **1700954**: 1–11. Copyright 2017, John Wiley & Sons, Inc.

¹⁰ Primary author and researcher. Colorado School of Mines

¹¹ This author and the first author contributed equally to this paper. Colorado School of Mines

¹² Colorado School of Mines

¹³ Colorado School of Mines

¹⁴ University of Colorado School of Medicine

¹⁵ Colorado School of Mines

¹⁶ Colorado School of Mines, University of Colorado School of Medicine

plasma-derived fibrin gels by tPA-microwheels is fivefold faster than with $1 \mu\text{g mL}^{-1}$ tPA. μ Wheels following corkscrew trajectories can also penetrate through $100 \mu\text{m}$ sized platelet-rich thrombi formed in a microfluidic model of hemostasis in ≈ 5 min. This unique combination of surface and bulk dissolution mechanisms with mechanical action yields a targeted fibrinolysis strategy that could be significantly faster than approaches relying on diffusion alone, making it well-suited for occlusions in small or penetrating vessels not accessible to catheter-based removal.

B.2 Introduction

Biochemical dissolution of blood clots, or thrombi, involves systemic or local delivery of plasminogen activators (PA) such as tissue-type plasminogen activator (tPA) and urokinase [1]. These PA convert plasminogen to plasmin, which in turn lyses fibrin fibers, the biopolymer that provides thrombi mechanical stability [2]. The efficacy of fibrinolytic therapy is limited by two transport barriers, the rate of delivery of PA to an occlusive thrombus, and the rate of dissolution. Delivery rates depend on the thrombus location and mode of administration; for example, during intravenous administration the concentration of PA is limited by diffusion to the occlusive thrombi interface when residual blood flow is minimal [3]. The rate of diffusion can be increased with higher systemic concentration, but values are limited by inherent bleeding risks associated with fibrinolytic therapy [4]. For catheter-based delivery, the local concentration can be higher than systemic administration; however, this delivery approach is limited to accessible large arteries. While dissolution rates generally depend on the local PA concentration, the thrombus composition, and the pressure gradient across the thrombus [5], in most cases removal is limited by PA penetration rather than by the kinetics of fibrin degradation [6]. This combined restriction

of transport of drug to and through the thrombus can significantly limit the time to reperfusion using biochemical methods alone.

Drug delivery via PA-functionalized micro- and nanoparticles or blood cells is an alternative approach that can result in higher local concentrations and faster lysis than systemic administration of PA alone [7-9]. When coupled with moieties that recognize fibrin(ogen) or transmembrane proteins on platelets [10], such particles can enhance accumulation at the surface of thrombi or take advantage of the unique fluid dynamics of a stenosed vessel [9]. These approaches however rely on blood flow to deliver particles to the injury site, which requires particles in circulation prior to what is typically an acute and unpredictable thrombotic event. As a result, there is a need for drug delivery strategies that can bring high concentrations of fibrinolytics to the surface of thrombi that does not rely on blood flow or diffusion alone. This is especially critical for occlusions present in vessels not accessible to catheters including deep penetrating cerebral arteries that are sites for lacunar strokes [11]. To deliver PA down such blocked vessels requires an alternative driving force, one that is not dependent on concentration or pressure gradients and yet is rapid enough to function within therapeutic time scales. Electromagnetic field-based approaches are such an alternative and others have used magnetic field gradients to drive PA immobilized on magnetic particles to a thrombus surface [12-15]; however, the field gradients required for rapid translation by magnetophoresis are quite high ($\approx 1 \text{ T m}^{-1}$) and difficult and expensive to implement in a clinical setting. Other field-based approaches to overcome diffusion limitations include enhancing mixing to reduce concentration gradients at the thrombus interface [16] or enhancing fibrinolysis with mechanical forces induced by ultrasound [17, 18]. However, the attenuation of ultrasound in tissues limits its use to superficial or easily accessible vessels.

To address these issues and without employing field gradients, we recently reported the assembly and translation of magnetically powered colloidal microwheels (μ wheels) capable of translation at speeds of over $100 \mu\text{m s}^{-1}$ [19]. In this, superparamagnetic microparticles cluster into wheel-like shapes when subject to a low-strength planar rotating magnetic field [20, 21]. Here, the rotation of the field induces a torque that, when balanced by fluid drag, leads to wheel rotation that depends on field frequency [22, 23]. In these studies, we have shown that, by orienting the field in a normal fashion and exploiting friction between μ wheels and adjacent surfaces, significant μ wheel translation speeds can be achieved. Travel direction can be precisely, rapidly, and readily controlled by simply shifting the applied field phase angle making control both immediate and precise. With both assembly and translation manipulated via weak, order milliTesla, external magnetic fields that do not attenuate in tissue, this method could be well-suited as a drug delivery strategy for obstructed blood vessels far from the body's outer surface.

While directed drug transport to the thrombus site is of significant advantage, rapid thrombus dissolution is also hindered by penetration of fibrinolytic agents into the fibrin network. To overcome this limitation, an approach that enhances μ wheel penetration into the fibrin network once it is delivered is required. Here we recognize that, driven by an applied external rotating field, μ wheel torques are significant and can be used to impose mechanical forces on thrombi. To exploit these forces, we take inspiration from nature and the enhanced transport one can achieve through viscous or solid materials with motions and geometries that are not straight but rather helical in form. Specifically, corkscrew shapes and motions are effective in applications both at microscopic and macroscopic length scales. For example, at the microscale where viscous forces dominate fluid dynamics, bacterial swimmers have only two

approaches available for translation, either corkscrew or flexible flagellar motion [24]. As a result, bacteria such as the genus *Spiroplasma* [25] with helical morphology use a corkscrew motion to swim [26, 27]. At macroscales, corkscrew geometries are used to improve penetration, ranging from the well-known wine bottle opener to even larger scale augers and mixers. In fact, one mechanical thrombectomy device, the MERCI retriever, uses a corkscrew to remove thrombi from large arteries [28]. All of these tools take advantage of a corkscrew geometry's unique ability to bore into a denser or more viscous phase.

We take advantage of the enhanced penetration such a motion can create using the unique ability to quickly and precisely redirect rotating μ wheels. With directional control performed through a simple shift in the applied field phase angle, we can create arbitrary translation patterns without increase in field strength or experimental complexity. Here and to demonstrate this approach, we functionalize μ wheels with tPA and use them to lyse fibrin gels. Compared to soluble tPA that lyses at the gel surface, tPA- μ wheels undergoing a corkscrew motion penetrate into the gel leading to a combined surface and bulk degradation that results in faster lysis. This biomechanical mechanism overcomes diffusion limitations associated with soluble tPA and provides physical action to disrupt gel structure.

B.3 Results and Discussion

μ Wheels were assembled and translated using magnetic fields of magnitude 9 mT rotating at frequencies of 100 Hz oriented away from a surface (Figure B.1). A field vector that traces a circle yields a direct, straight-line motion (Figure B.1A,D). A field vector that traces a helical loop yields a corkscrew motion that still leads to net forward translation (Figure B.1B,E). For the same field strength and rotation frequency the corkscrew motion has an approximately twofold slower linear translation velocity than direct motion (Video B.S1), where specific field

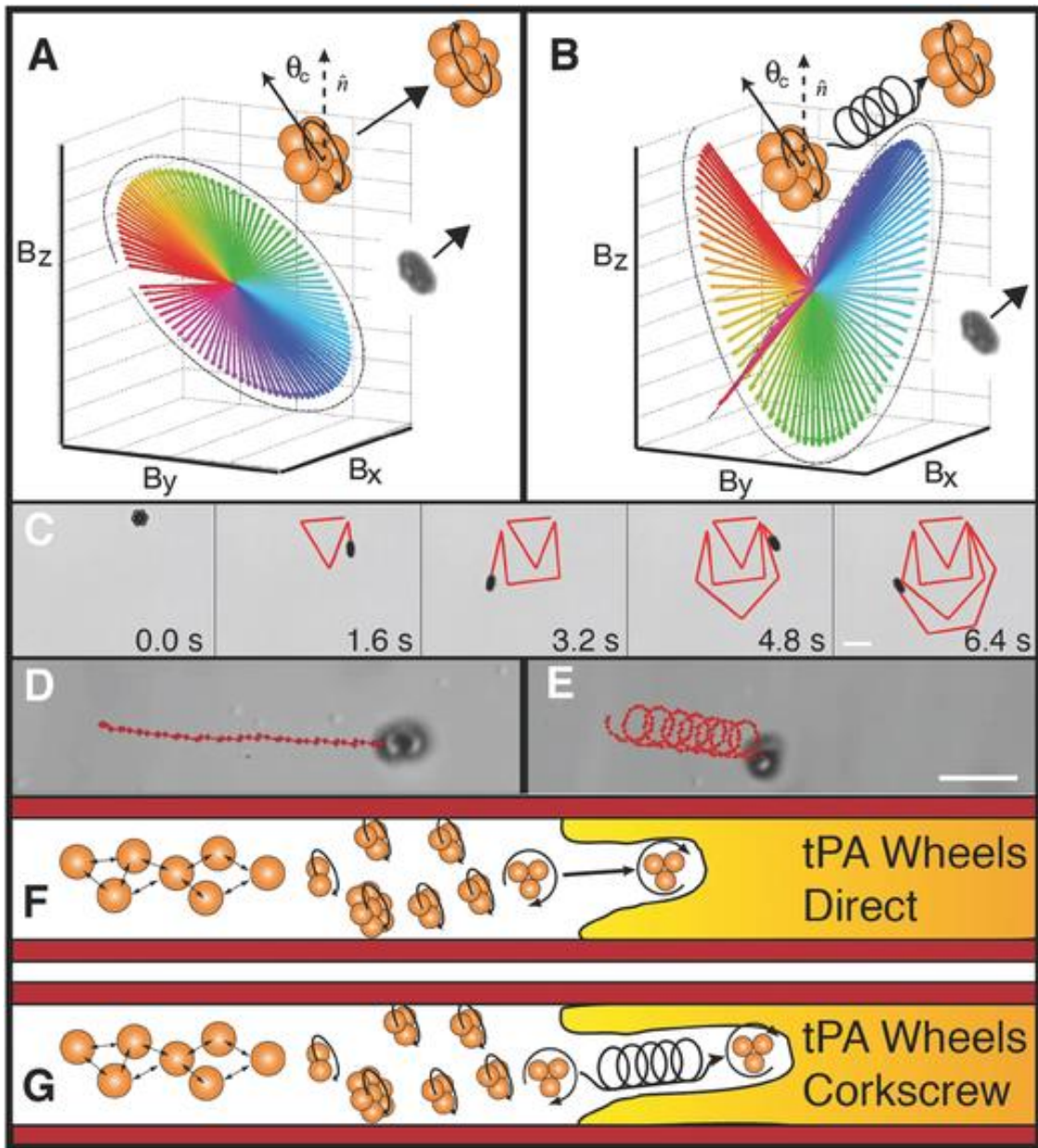


Figure B.1: Approach to tPA- μ wheel-induced reperfusion of occluded channels. A,C,D) With application of a rotating magnetic field, \vec{B} , oriented out of the surface plane at a camber angle θ_c relative to the normal \hat{n} , colloids assemble, “stand up,” and roll along the surface. Color of vector tracing indicates field rotation angle. C) Because field orientation can be instantly changed, μ wheels can be quickly redirected and follow preprogrammed or manually controlled paths. Scale bar = 10 μm . B,E) With a rotating “corkscrew” field, an additional helical component to wheel motion can be induced. Scale bar = 10 μm (Video B.S1). While both modes can be used to assemble μ wheels and do lead to high concentration of μ wheels at the gel interface, F) direct motion based primarily on biochemical dissolution lyses slower than G) helical motion that yields combined mechanical and biochemical action.

conditions and μ wheel size lead to 2.8 vs 1.4 $\mu\text{m s}^{-1}$). Other complex paths are achievable by varying the phase angle of the z -component of the magnetic field (Figure B.1C). We compare the dissolution rate of fibrin gels with and without platelets using these two motions for μ wheels functionalized with tPA and compare them to soluble tPA without μ wheels (Figure B.1F,G).

To first demonstrate enhanced transport down stagnant channels, we compare the delivery of tPA-functionalized μ wheels (tPA- μ wheels) to diffusion of tPA alone (Figure B.2). Figure B.2A shows the experimental geometry where tPA-coated beads were delivered into a stagnant channel, assembled within a rotating magnetic field into μ wheels, and then translation velocities were directly measured. μ Wheels roll and accumulate at the interface of the fibrin gel (Figure B.2A) where, consistent with our previous studies [19], we observe a broad distribution of μ wheel sizes (Figure B.2B) and velocities (Figure B.2C). With μ wheels readily directed down stagnant channels in this manner, we compare tPA- μ wheel drug delivery to free tPA diffusion. Using the measured velocity distribution (Figure B.2C), we compare the concentration of tPA- μ wheels at the gel interface to that of free tPA. In both cases, tPA is introduced at $L = 1$ mm distal of the gel interface at concentration, C_0 . Upon field application, μ wheels translate toward the fibrin gel front while free tPA diffuses. Comparing predicted concentration profiles at the gel surface in Figure B.2D, two significant advantages are immediately apparent. The first is that the transit times of tPA to the interface are significantly decreased; importantly however and because transport is not driven by a concentration gradient, the local concentration of tPA on the μ wheels at the gel is much higher than the initial concentration C_0 . In contrast, for diffusive delivery of free tPA the concentration at the interface can only approach C_0 . This accumulation of μ wheels is readily observed experimentally as shown in Figure B.2E and Video B.S2.

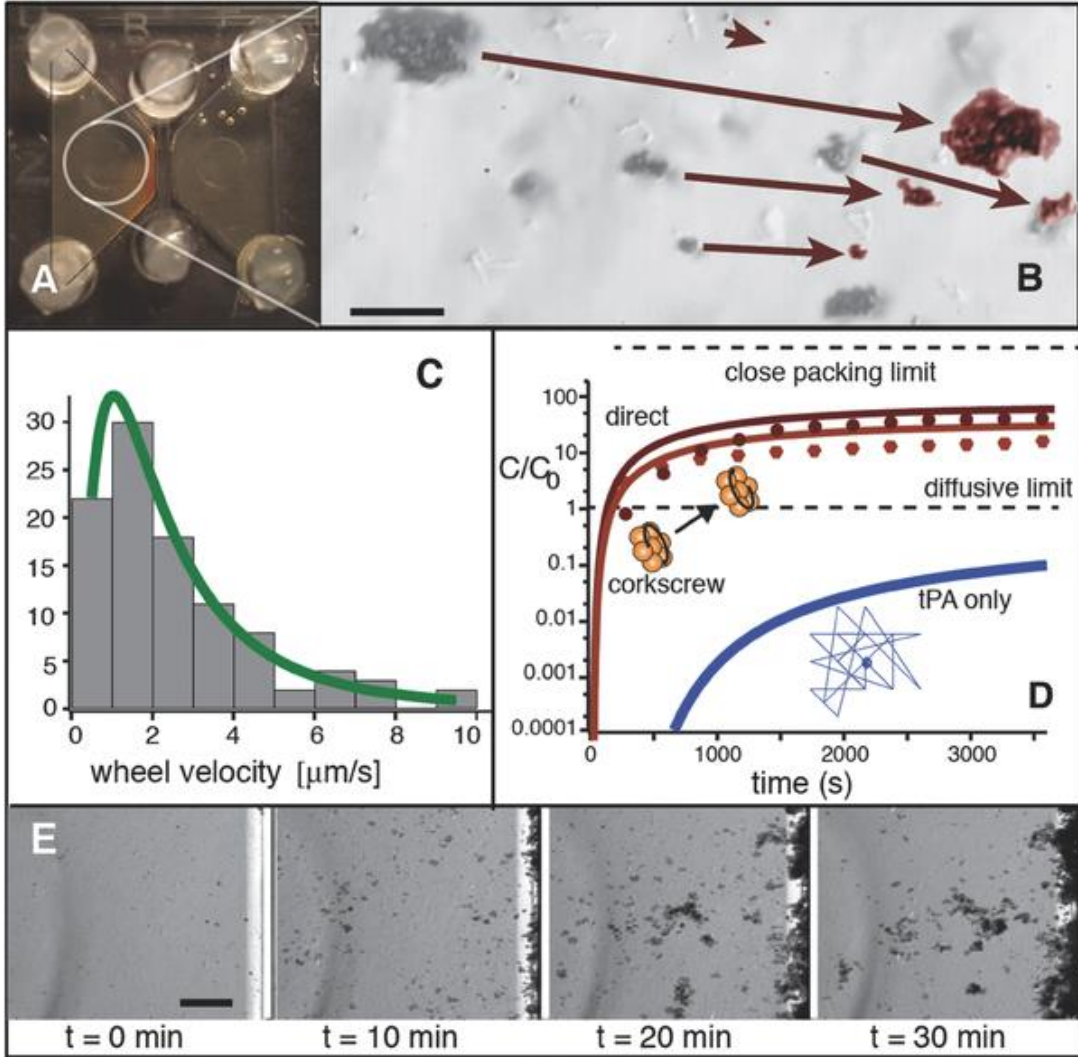


Figure B.2: Wheel-based drug transport overcomes diffusion limitations down stagnant channels. A) Upon application of the magnetic field, tPA- μ wheels accumulate at the front edge of the fibrin gel in a microfluidic device (rust colored region). Note the fibrin gel is present in the region separating the two reservoirs (see also Figure 3A). B) Larger μ wheels translate faster than smaller μ wheels as shown in red overlay ($\Delta t = 10$ s, scale bar = $10 \mu\text{m}$). C) Measured tPA-wheel velocity distribution for direct motion ($N = 102$) with log-normal fit. D) Predicted tPA concentration C/C_0 at the gel front for $L = 1$ mm and both free tPA and μ wheel-bound tPA (see the Experimental Section). Corresponding measurements of μ wheel concentration at the interface shown as data points. Note that μ wheel concentration quickly exceeds the maximum concentration achievable via tPA diffusion alone. E) Driven by wheel rolling only, μ wheel accumulation at the gel front (right) is easily observed at low resolution (Video B.S2, scale bar = $200 \mu\text{m}$).

To demonstrate the relative lysing effectiveness of tPA- μ wheels compared to soluble tPA, we form fibrin gels using thrombin and normal pooled plasma (NPP) with a height $70 \mu\text{m}$

and length 800 μm between two reservoirs of NPP in a microfluidic device (Figure B.2A and illustrated in Figure B.3A). Note that because all three compartments are filled with plasma or a plasma-derived fibrin gel, the endogenous inhibitors of tPA and plasmin, plasminogen activator inhibitor1 (PAI-1) and α_2 -antiplasmin, are present at physiologic concentrations.

For quantification, the gel degradation front was monitored by optical microscopy as a function of time for two concentrations of tPA, 1 and 10 $\mu\text{g mL}^{-1}$, and two tPA- μ wheel motions, direct and corkscrew (Figure B.3B–D). Biotinylated tPA was immobilized on 1 μm streptavidin-coated superparamagnetic particles. These tPA-functionalized particles at a concentration of $1.5 \times 10^6 \mu\text{L}^{-1}$ have a tPA mass concentration of 9 $\mu\text{g mL}^{-1}$ and an activity of 930 IU mL^{-1} , which is comparable in activity to 3.6 $\mu\text{g mL}^{-1}$ soluble tPA (Figure B.3E). The roughly one-third reduced activity of the immobilized tPA compared to soluble tPA is expected because tPA molecules bind to particles in varying orientations, likely with some fraction bound with their enzymatic domains inaccessible to plasminogen. Note that we performed experiments both above and below the high end of systemic tPA concentration ($\approx 3 \mu\text{g mL}^{-1}$) following intravenous injection [5].

For direct motion, a rotating magnetic field canted off the surface at 43° drives the assembly and translation of tPA- μ wheels. Individual particles and small tPA- μ wheels (2–7 particles) accumulate at the surface of the fibrin gel within the first 10 min and a small fraction of them penetrate into the fibrin gel (Video B.S2). At late times (>20 min) however, μ wheels become larger and larger, growing to discs with diameters as large as 50–100 μm . These larger μ wheels tend to attract smaller μ wheels, resulting in a reduced number of penetrators. Also, because of continuous rotation in one direction, wheels tend to roll tangentially along the liquid–gel interface as opposed to digging into the network.

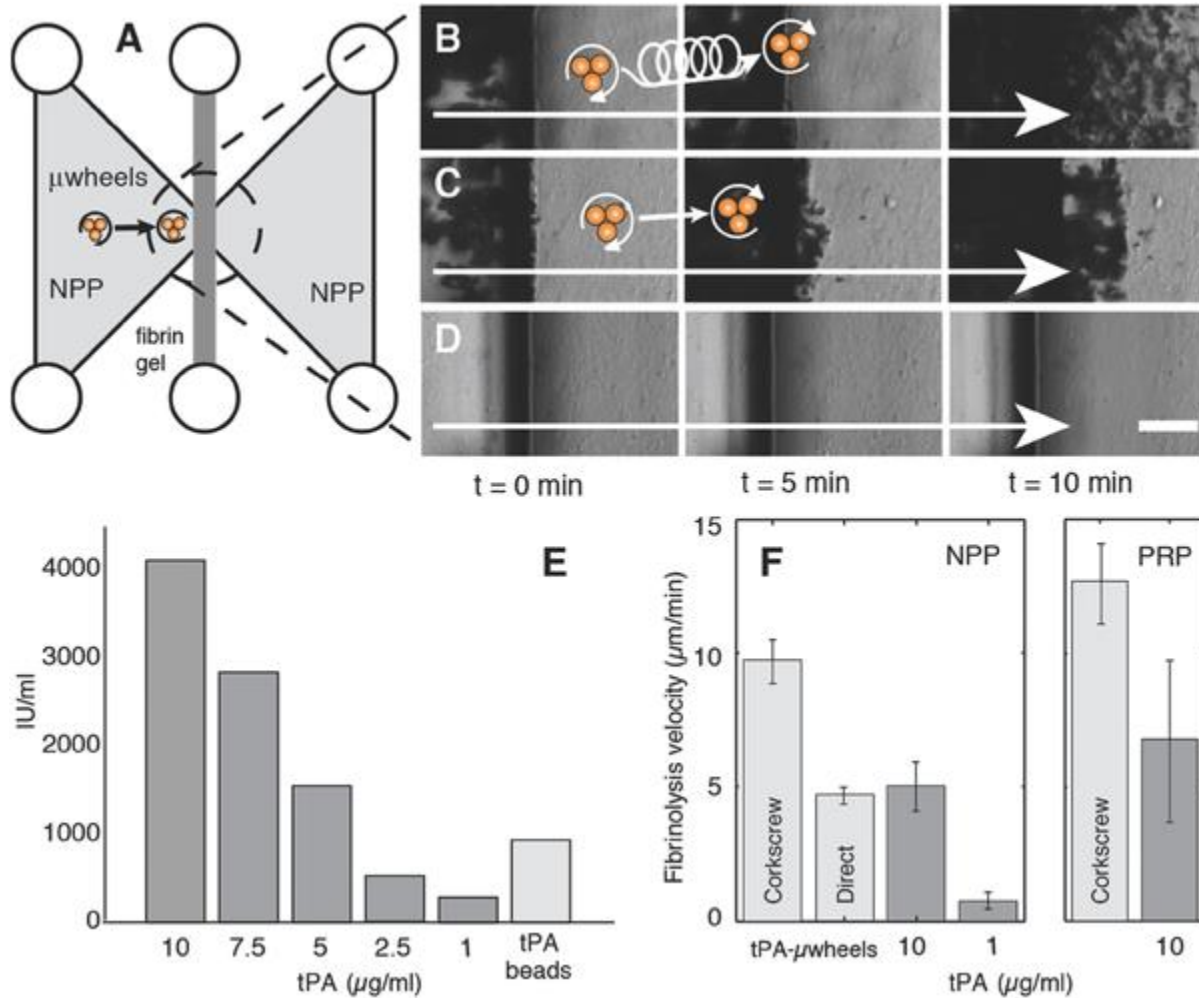


Figure B.3: Faster lysis occurs with tPA-coated beads and addition of corkscrew action. A) Illustration of Figure 2A where a plasma-derived fibrin gel is formed between two normal pooled plasma (NPP) reservoirs. Images and data acquired near the center of the dashed circle region. B) tPA-coated beads (left) penetrating by corkscrew motion into fibrin gel, magnetic field strength = 9 mT, frequency = 100 Hz; C) tPA-coated beads and direct motion; D) soluble tPA alone ($1 \mu\text{g mL}^{-1}$), scale bar = $40 \mu\text{m}$. E) tPA and tPA-coated bead activity measured by cleavage of a fluorogenic substrate. F) Fibrinolysis velocity of tPA versus tPA- μ wheels for plasma-derived fibrin gels and gels formed with platelet rich plasma (PRP) (Video B.S3).

For corkscrew motion, we use identical magnetic field magnitudes and frequencies except now we alter the μ wheel direction angle from -90° to $+90^\circ$ in 45° increments at 0.1 s time steps, achieving a net forward motion bias in the process (Video B.S1). This corkscrew

motion inhibits larger assemblies and maintains μ wheel translation perpendicular to the liquid–gel interface. These features result in a higher number of penetrating μ wheels for the corkscrew motion compared to the direct motion.

tPA-functionalized μ wheels overcome transport limitations facing soluble PA in two ways. First, as shown in Figure B.2, μ wheels accumulate at high density at the fibrin gel front as the translation velocity to the interface is significantly faster than the fibrin gel degradation rate with and without platelets ($4\text{--}13\ \mu\text{m min}^{-1}$) (Figure B.3F, and Video B.S3). As such, local concentration of tPA is orders of magnitude greater than the initial concentration. This is in contrast to soluble tPA where the initial and local concentrations are, at best, equal; however, in practice, local tPA concentration is likely lower because of its adsorption to fibrin and limitations inherent in diffusion down a stagnant channel [29]. Second, and what is particularly unique to this approach, is that μ wheel motion can be directed to penetrate into the fibrin gel, effectively altering the mechanism of degradation.

To frame our interpretation of μ wheel penetration and its effect of fibrinolysis, we appeal to the concepts of surface and bulk erosion used to describe polymer degradation [30, 31], often in the context of degradable drug delivery systems. Surface erosion refers to degradation at the liquid–solid interface, a diffusion-limited process that accurately describes the dissolution of fibrin gels by tPA in solution [32]. Bulk erosion refers to a homogenous inside-out degradation, a reaction-limited process when the transport into a solid matrix is faster than its degradation kinetics. In the case of soluble tPA, the process is dominated by surface erosion as the surface degradation kinetics are faster than diffusion of tPA into the fibrin gel. Our results suggest that this is indeed the case with average velocities of $0.81 \pm .25\ \mu\text{m min}^{-1}$ for the $1\ \mu\text{g mL}^{-1}$ and $5.0 \pm 1.5\ \mu\text{m min}^{-1}$ for the $10\ \mu\text{g mL}^{-1}$ tPA case. In experiments with tPA- μ wheels however, fibrin

dissolution shows significantly enhanced lysis velocities. We measured average velocities of $4.8 \pm 0.3 \mu\text{m min}^{-1}$ for direct motion and $9.6 \pm 1.5 \mu\text{m min}^{-1}$ for corkscrew motion into fibrin gels. Note, a fraction of penetrating tPA- μ wheels translate at speeds faster than the degrading interface such that these lysis velocities underestimate the penetration velocity of some μ wheels through the gel. With direct motion we observe degradation velocities comparable to concentrations at threefold the active tPA ($10 \mu\text{g mL}^{-1}$). For corkscrew motion, we see degradation velocities twofold faster than direct motion. For comparison, μ wheels without immobilized tPA do not induce any lysis, suggesting that the mechanical forces imposed by the μ wheels on the fibrin gel are not sufficient to rupture fibrin fibers. Similar enhancement in degradation rate with corkscrew motion is observed in fibrin gels derived from platelet-rich plasma (PRP, Figure B.3F) and dense fibrin gels (NPP with 10 mg mL^{-1} fibrinogen, Figure C.1, Appendix C). For the dense fibrin gels, the corkscrew motion enhancement is $\approx 50\%$ greater than direct motion. Here, because the gel pore size is comparable to the size of individual particles [33], there is significantly less penetration than observed in NPP (Video B.S4).

The biochemical mechanisms of fibrinolysis by tPA-functionalized μ wheels may vary from soluble tPA. The rate of plasmin generation is enhanced by fibrin because tPA and plasminogen bind to it to form a ternary complex that promotes conformational changes and their interaction [34, 35]. tPA and plasminogen can bind to fibrinogen and produce plasmin [36, 37] but at a reduced rate compared to fibrin [35]. Degradation products including fibrin monomers and D-dimer can also bind tPA and plasminogen and accelerate plasmin generation to rates that are comparable to fibrin [38, 39]. We hypothesize that initial fibrinolysis is mediated by a complex of immobilized tPA-fibrinogen-plasminogen, which may describe the lag time observed prior to observable movement of the fibrin interface (Video B.S3, Supporting Information). As

degradation products are released and μ wheels penetrate into the gel, the rate of fibrinolysis increases.

The combination of biochemical and mechanical action allows tPA- μ wheels to penetrate into the gel, enhancing internal dissolution (Figure B.4A–D) and increasing the velocity with which the surface front degrades. For direct motion, small μ wheels (<4 particles) follow a relatively straight trajectory and penetrate 100–200 μ m into the gel in the first 20 min of lysis (Figure B.4E); however, after this initial transient, the size of penetrating μ wheels increases and, accordingly the depth of penetration decreases. This is a result of large cluster formation at the front interface; big μ wheels tend to grow at the expense of additional monomers and smaller μ wheels (Figure B.4F). With introduction of a corkscrew motion, a near constant penetration depth of 40–60 μ m was observed (Figure B.2G). Here, penetrators are primarily larger μ wheels (>4 particles) and more numerous. Unlike direct motion, corkscrew motion inhibits the formation of the largest assemblies (Video B.S3). In addition, the helical pattern allows μ wheels to sample the fibrin network and probe those weakest regions of the gel while direct motion μ wheels are inhibited by relatively tough fibrin obstacles that are difficult to circumvent. These observations suggest that penetrating μ wheels “soften” the gel by bulk erosion, which in turn results in faster front velocities.

To demonstrate that tPA- μ wheels can also penetrate and degrade platelet-rich thrombi characteristic of arterial thrombosis and emboli, we turn to a previously developed microfluidic model of hemostasis [40]. In this model, collagen-mimetic peptides and tissue factor (TF) are adsorbed to the wall of a horizontal “injury” channel connected by two vertical channels (Figure B.S2). One vertical channel is perfused with blood and the other with a wash buffer. To form a thrombus, blood is directed from the vertical blood channel into the injury channel under a

constant pressure drop. Platelets and fibrin accumulate in the injury channel, forming an occlusive thrombus in ≈ 5 min. Following thrombus formation, we introduce tPA- μ wheels into the wash channel and direct them into the thrombus using the corkscrew motion (Video B.S5, and Figure B.5). It takes ≈ 5 min for the first μ wheels to penetrate through the thrombus along the wall of the injury channel. Over the next 25 min, much of the remaining fibrin is lysed and platelets are displaced as indicated by a reduced fluorescence intensity (Figure B.5). These data show that tPA- μ wheels can penetrate and lyse platelet-rich thrombi.

Experiments in this study using fibrin gels were performed in the absence of pressure gradients and thus any interstitial flow. These conditions are relevant both to deep vein thrombosis where fibrin-rich thrombi several centimeters in length can form, attenuating any pressure difference across the thrombus, as well as in to arterial thrombosis where low permeability platelet-rich thrombi result in very low interstitial flows even for significant pressure gradients [33, 41]. In both cases, heterogeneities in thrombus structure can result in regions that are more permeable and more susceptible to fibrinolysis under pressure-driven flow [42-44]. In our studies, the size of individual colloids and small μ wheels is on the same order of magnitude as dense fibrin gel pores [45] and may benefit from convective transport by either enhancing μ wheel penetration or by conveying plasmin deeper into a thrombus.

With regards to potential biomedical application, we have observed that mechanical forces alone, without available tPA, are insufficient for gel lysis. This is expected as mechanical forces estimated from rotational frequency and wheel size based on fluid torque on a disk, $32\mu a^2\Omega/3$ [35], predict rotational forces of order pN. When one compares this value to the forces required to break up a fibrin network of order 1 mN [46], it is clear that a biochemical component is necessary for enhanced fibrinolysis. These relatively weak mechanical forces

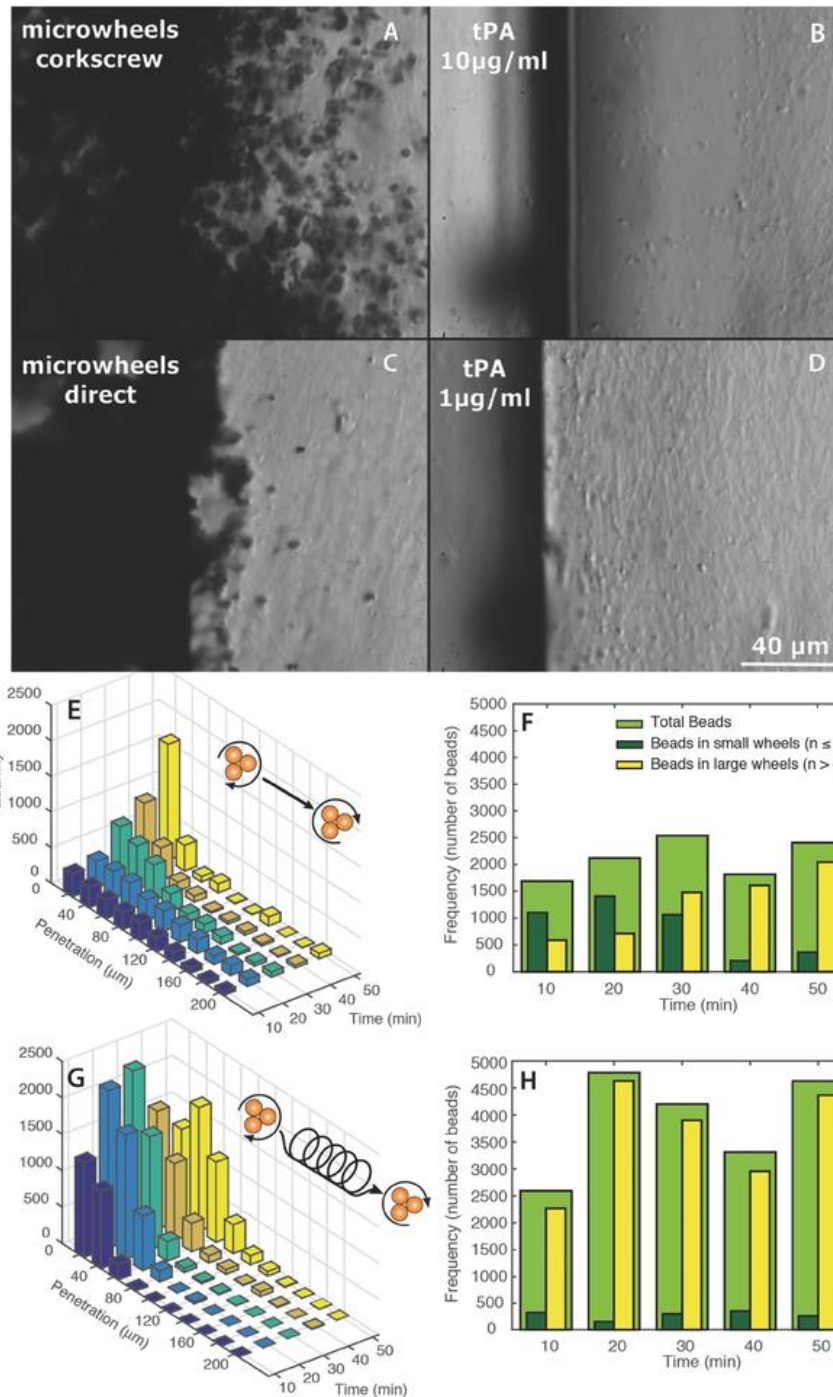


Figure B.4: An increasing volume of tPA- μ wheels penetrate into the gel as time proceeds via direct (biochemical) or corkscrew (biochemical + mechanical) lysis modes. A–D) Snapshot of Video B.S3 ($t = 6$ min) where improved penetration via corkscrew motion is apparent. E) Bead penetration with smaller wheels penetrating deeper. F) Penetrating beads with distribution of large and small wheels for direct motion. G) Corkscrew mode with higher total bead number penetration at shallower depth at short times. H) Penetrating bead distribution for corkscrew motion.

however, sufficient for μ wheel transport, are an advantage for potential biomedical applications as 1 pN is insufficient to damage endothelial cells. In this, forces of $14.9 \pm 1.6 \text{ nN } \mu\text{m}^{-1}$ are required for cell rupture [37], 3–4 orders of magnitude higher than the μ wheel mechanical forces available here. In addition, and because the required field strengths are two to three orders of magnitude less than those required for MRI [38], the surrounding physical infrastructure required is more readily achievable.

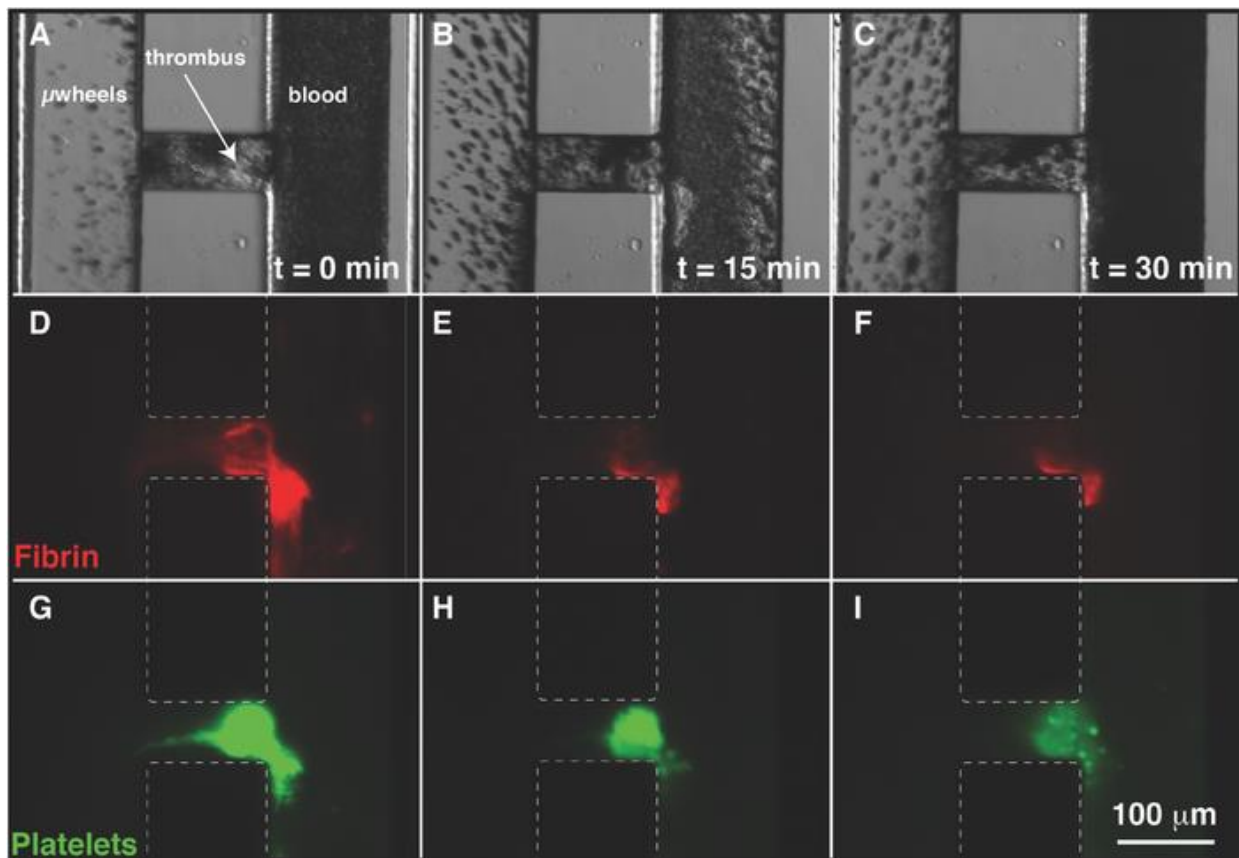


Figure B.5: Fibrinolysis of a platelet-rich thrombus in a microfluidic model of hemostasis by tPA- μ wheels. Snapshots from Video B.S5 (Supporting Information) at 0, 15, and 30 min. The thrombus occludes the horizontal channel coated with collagen-mimetic peptides and tissue factor. Following occlusion, μ wheels are introduced from the left vertical channel with blood present in the right vertical channel. A–C) Brightfield images of μ wheels accumulating at and penetrating into the thrombus. Epifluorescence of D–F) fibrin(ogen) and G–I) platelets.

The field magnitudes are not only significantly lower but also field gradients are not required to induce translational forces, a significant drawback associated with other magnetic-field-based microdevice manipulation approaches [39]. There are several potential strategies for targeting occlusive thrombi in vivo that are compatible with the simple external magnetic fields required for rolling-based translation. If the approximate position of the thrombus is known, then the rotating field can be oriented to drive individual particles and assemblies in that general direction along vessel walls. This strategy would likely work best in occluded vessels where significant shear forces due to blood flow are not present. For particles and μ wheels to escape from a vessel of normal or elevated blood flow into one with reduced or no blood flow, an additional gradient-based field may be required. Such magnetophoretic methods have had success in vivo to help guide catheters for treatment of brain diseases and stroke [47], as well as to guide superparamagnetic particles toward occlusive thrombi [16].

B.4 Conclusions

Biochemical dissolution of fibrin gels and thrombi by therapeutic concentrations of soluble tPA is a diffusion-limited process. Here, we show that a combined biochemical and mechanical lysis strategy can be implemented using directed assembly of colloidal μ wheels functionalized with tPA. In this, dispersed colloidal particles are injected into the system at low density, assemble into μ wheels in situ, and are then rapidly driven to the liquid–gel or liquid–thrombus interface creating a high local concentration of tPA. A unique feature of this approach is that tPA- μ wheels not only accumulate at the surface but also are driven by a field that creates a corkscrew motion leading to penetration into the fibrin network or thrombus and bulk degradation which enhances surface dissolution. Because μ wheels are approximately the same size as blood cells, they have potential application for relieving thrombosis in small vessels

where catheters cannot reach and where systemic delivery of PA is ineffective due to transport limitations.

B.5 Experimental Section

B.5.1 Magnetic Field Setup

Magnetic fields were created using five air cored solenoid coils (50 mm inner diameter, 51 mm length, and 400 turns) [19]. Applied voltages were generated using Matlab (Mathworks, Inc., Natick, MA) and an analog output card (National Instruments, NI-9263). Voltages from the output card were increased using three dual-output amplifiers (Behringer EP2000) before being applied to individual solenoids with currents monitored using an analog input card (National Instruments, NI-USB-6009). The total field strength at the center of the magnetic field system was up to 9 mT at 100 Hz (measured using a VGM Gaussmeter, Alphalab Inc.). For direct motion experiments, the magnetic field was programmed so that particles are constantly traveling in the $+x$ direction (Video B.S1). The corkscrew motion was programmed such that the particles traverse a forward biased spiral path where each cycle was completed in 1 s.

B.5.2 Wheel Assembly and Motion

Rotating magnetic fields were employed in-plane to assemble μ wheels by isotropic interactions with size determined by local colloid concentration [19]. Spinning μ wheels lying flat on a surface have no net motion; to roll, they must be inclined relative to the surface. To induce translation, a normal component was added to the magnetic field to reorient μ wheels to a defined camber angle θ_c . Because rolling velocity is a balance of fluid drag and wet friction with the surface, important parameters are the number of particles comprising the μ wheel and, as wheels rotate, the outer circumferential velocity. With this, we find rolling velocities up to and above

$100 \mu\text{m s}^{-1}$ at field strengths of $\approx 15 \text{ mT}$ with a scaling of $V \sim \omega n \cos(\theta_c)$ where ω is the angular frequency of the μ wheel and n the number of particles in a wheel.

B.5.3 Preparation of tPA Conjugated Beads

Recombinant tissue plasminogen activator (Louisville APL Diagnostics, Inc., Seabrook, TX) was conjugated to biotin using N-hydroxysuccinimide (NHS) activated biotin (Life Technologies Corporation, Carlsbad, CA). Briefly, 50-fold molar excess NHS-biotin was allowed to react with tPA ($200 \mu\text{g mL}^{-1}$) over ice for 4 h. Excess biotin was removed using a desalting column (Life Technologies Corporation, Carlsbad, CA) with a molecular cutoff of 7000 Da. Biotinylated tPA (b-tPA) was stored in $20 \mu\text{L}$ aliquots at $-80 \text{ }^\circ\text{C}$ until use. $5 \mu\text{L}$ of $1 \mu\text{m}$ streptavidin conjugated iron oxide beads (Thermo Fisher Dynabeads MyOne Streptavidin T1) were mixed with b-tPA ($20 \mu\text{L}$) and allowed to sit at $4 \text{ }^\circ\text{C}$ overnight to allow binding of b-tPA to the beads. Beads were then washed five times with $15 \mu\text{L}$ of 2% bovine serum albumin (BSA) in HEPES-buffered saline (HBS) to remove any unbound b-tPA.

B.5.4 Concentration Profiles

Predictions for the diffusion-driven time-dependent concentration of tPA down a stagnant channel were calculated from the 1D solution of Fick's law given a Heaviside step function initial condition and reflection at the fibrin gel boundary $z=L$. Following Crank, the following equation is obtained [40]:

$$\frac{C(z,t)}{C_0} = \frac{1}{2} \left[\text{erfc} \left(\frac{z}{2\sqrt{Dt}} \right) + \text{erfc} \left(\frac{2L-z}{2\sqrt{Dt}} \right) \right] \quad (\text{B.1})$$

and, evaluating $C(z=L,t)$ with $L = 1000 \mu\text{m}$ and $D = 50 \mu\text{m}^2 \text{ s}^{-1}$ provides the time dependent concentration $C(L,t)/C_0$ provided in Figure B.2D. tPA- μ wheel concentrations were predicted from the measured lognormal velocity distribution (Figure B.2C)

$$f(v) = \frac{1}{v\sigma\sqrt{2x}} \exp\left[-\frac{(\ln(v)-\mu)^2}{2\sigma^2}\right]. \quad (\text{B.2})$$

At a given distance z from the fibrin front, the probability p at time t of wheels reaching the front can be expressed as:

$$p(z, t) = 1 - \int_0^{\frac{z}{t}} f(v) dv = \frac{1}{2} \operatorname{erfc}\left[\frac{\ln\left(\frac{z}{t}\right) - \mu}{\sigma\sqrt{2}}\right]. \quad (\text{B.3})$$

Defining a wheel accumulation front width $\Delta w = 100 \mu\text{m}$ allows expression of tPA- μ wheel concentration at the fibrin interface (Figure B.2D) as:

$$\frac{c(t)}{c_0} = \frac{1}{\Delta w} \int_L^\infty p(z, t) dz = \frac{1}{2\Delta w} \left\{ t \exp\left(\mu + \sigma^2/2\right) \operatorname{erfc}\left[\frac{\ln\left(\frac{L}{t}\right) - \mu - \sigma^2}{\sigma\sqrt{2}}\right] - L \operatorname{erfc}\left[\frac{\ln\left(\frac{L}{t}\right) - \mu}{\sigma\sqrt{2}}\right] \right\}. \quad (\text{B.4})$$

To compare to experimental values, beads (bulk concentration $C_0 = 1.5 \times 10^6 \mu\text{L}^{-1}$) were injected 1 cm from the front before being subjected to the rotating magnetic field. Once wheels reached within 1000 μm of the front, data collection was initiated and colloid flux into a control volume of width 100 μm from the front (height = 240 μm , depth = 70 μm) was quantified using ImageJ. Concentration of beads inside the control volume was determined by integrating the influx, assuming a negligible outflux as observed experimentally. Correspondingly for the theoretic curves of Figure B.2D, limits of integration were set from $L = 1000 \mu\text{m}$ to an upper limit of 10 000 μm . The close packed limit was determined by converting experimental values of C_0 to volume fraction and comparing to the hard-sphere random packing limit [48].

B.5.5 Fibrinolysis Experiments

Fibrinolysis experiments were conducted using IBIDI μ slide chemotaxis chips (IBIDI, Martinsried, Germany). These chips consist of one middle channel (6 μL) and two side channels (65 μL). To prepare fibrin gels, NPP was recalcified to CaCl_2 ($20 \times 10^{-3} \text{M}$) and mixed with thrombin (final concentration $4.5 \times 10^{-9} \text{M}$), before being immediately injected into the

observation channel of the chip. To make dense fibrin gels, exogenous human fibrinogen (Enzyme Research Laboratory, South Bend, IN) was added to the NPP to raise the final fibrinogen concentration to $10 \mu\text{g mL}^{-1}$. After injection, the chip was kept in a humid box at room temperature for 1 h, then soluble tPA or the tPA-coated beads were injected in one of the side channels and the other side channel filled with NPP (George King Bio-Medical, Inc., Overland Park, KS). Each fibrinolysis experiment was conducted for 1 h and lysis was monitored and recorded using relief contrast microscopy on an inverted microscope (Olympus IX 70, 40 \times objective, NA 0.75) with camera (Epix SV 643M) operated at 30 frames s^{-1} . To maintain identical conditions between experiments, the magnetic field was applied both during tPA bead experiments and during soluble tPA experiments without beads as well. Solenoid coils were cooled with forced air with the temperature at the middle of the solenoids fixed at 26 $^{\circ}\text{C}$.

B.5.6 tPA Activity Measurements

Activities of soluble tPA and tPA beads were determined using fluorescence measurements with a Biotek Synergy H1 Microplate Reader (BioTek U.S. Winooski, VT). Soluble tPA activities were determined for 1, 2.5, 5, 7.5, and $10 \mu\text{g mL}^{-1}$ tPA using a chromogenic substrate (100×10^{-6} M SN-18, Haematologic Technologies, Inc., Essex Junction, VT) in plasma in 20 μL working volumes. To obtain the tPA coated bead activity, beads were mixed with the substrate and NPP in 0.5 mL vials and then removed each hour using a permanent magnet to take a measurement.

B.5.7 Blood Collection and Preparation

Blood was collected from healthy donors by venipuncture into vacutainer tubes containing 3.2% sodium citrate. Donors had not consumed alcohol within 48 h prior to the blood draw, nor had they taken any prescription or over-the-counter drugs within the previous 10 d

excluding oral contraception. The first tube of blood collected was discarded. All procedures were in accordance with the ethical standards of the responsible committee on human experimentation (University of Colorado, Boulder, CO) and with the Helsinki Declaration of 1975, as revised in 2000. Informed consent was obtained from all subjects for being included in the study. Aliquots of citrated 960 μL blood collected in sodium citrate were combined in tubes with 40 μL of Alexa-555 labeled fibrinogen (final concentration 56 $\mu\text{g mL}^{-1}$) which was added to visualize fibrin deposition. Platelets were labeled with the lipophilic dye DiOC6 (1×10^{-6} M final concentration). Labeled platelets were incubated at 37 °C for 15 min prior to the assay.

B.5.8 Microfluidic Model of Hemostasis

Platelet-rich thrombi were formed in a microfluidic model of hemostasis as previously reported (Figure C.2, Appendix C) [40]. The master template for the device was prepared with photoresists (KMPR 1010 and KMPR 1050) to define a two-layer device with heights of 20 and 50 μm . Polydimethylsiloxane (PDMS) was molded off of these masters and covalently bonded to glass using standard soft lithography procedures. The device was designed in the shape of the letter “H” where the outer two vertical channels represent the vascular and extravascular compartments (10 mm long \times 100 μm wide \times 50 μm high), respectively. The vertical channels were connected by a horizontal channel (150 μm long \times 50 μm wide \times 20 μm high) representing a hole in the vessel wall, which is referred to as the injury channel. A mixture of three triple-helical collagen-mimetic peptides (100 $\mu\text{g mL}^{-1}$, Richard Farndale, University of Cambridge) [49]—a glycoprotein VI agonist collagen-related peptide (CRP-XL), the von Willebrand factor A3 domain binding site on collagen III (VWF-III), and a $\alpha_2\beta_1$ specific binding peptide (GFOGER)—was mixed 1:1 with tissue factor (TF, Dade Innovin) before being adsorbed to the

walls of the injury channel at 4 °C for 12 h. The rest of the device was blocked for 1 h before the experiment with 2% BSA in HEPES buffered saline (HBS, 150×10^{-3} M NaCl, 25×10^{-3} M HEPES, pH 7.4). Pressure was controlled for the blood, recalcification buffer (75×10^{-3} M CaCl₂ and 35×10^{-3} M MgCl₂ in HBS), and wash buffer (3.2% sodium citrate in HBS) independently by applying a pressure to the headspace of their respective reservoirs using a pressure-based flow controller (Fluigent MFCS, Villejuif, France). Blood was recalcified in the ratio of 9:1 (citratated whole blood:recalcification buffer) using a herringbone mixer [50] to final concentrations of 7.5×10^{-3} M CaCl₂ and 3.75×10^{-3} M MgCl₂. The output from the herringbone mixer was connected to the blood channel of the extravascular injury device (Figure C.2). The pressures of the blood and recalcification reservoirs were held constant at 10 kPa. The pressure in the wash buffer was initially set to 3.5 kPa to drive a small amount of wash buffer through the injury channel while the blood channel was filled with recalcified blood driven by 10 kPa of pressure in the blood and recalcification reservoirs. The pressure in the wash reservoir was then reduced to 1.75 kPa so that the blood passes from the blood channel into the injury channel and out into the extravascular channel. After the thrombus formed in the injury channel of the device, all external tubing was removed and tPA-functionalized beads suspended in 2% BSA in HBS were introduced into the extravascular wash channel with a number density of 1.5×10^6 beads μL^{-1} (effective tPA concentration: $3.6 \mu\text{g mL}^{-1}$). The magnetic field was then used to induce corkscrew motion of the beads directed into the thrombus. Thrombus formation and lysis were monitored through an inverted microscope (Olympus, IX81, 20× objective, NA 0.45) equipped with a 16-bit CCD camera (ORCA-R2, Hamamatsu).

B.5.9 Statistical Analysis

Gel front positions were determined from stored video for all conditions investigated. With $N = 3$ measurements for separately prepared samples, averages and standard deviations were determined to perform a power law weighted least squares fit to $x = Aty$ using Igor Pro (Wavemetrics, Inc.). Errors reported to power law fits represent one standard deviation.

B.6 References

- 1 Longstaff C, Kolev K. Basic mechanisms and regulation of fibrinolysis. *J Thromb Haemost* 2015; **13**: S98–105.
- 2 Weisel JW. Structure of fibrin: Impact on clot stability. *J Thromb Haemost* 2007; **5**: 116–24.
- 3 Labiche LA, Malkoff M, Alexandrov A V. Residual flow signals predict complete recanalization in stroke patients treated with TPA. *J Neuroimaging* 2003; **13**: 28–33.
- 4 Gore JM, Sloan M, Price TR, Young Randall AM, Bovill E, Collen D, Forman S, Knatterud GL, Sopko G, Terrin ML. Intracerebral hemorrhage, cerebral infarction, and subdural hematoma after acute myocardial infarction and thrombolytic therapy in the thrombolysis in myocardial infarction study. Thrombolysis in myocardial infarction, Phase II, pilot and clinical trial. *Circulation* 1991; **83**: 448–59.
- 5 Diamond SL. Engineering Design of Optimal Strategies for Blood Clot Dissolution. *Annu Rev Biomed Eng* 1999; **1**: 427–61.
- 6 Anand S, Wu J -H, Diamond SL. Enzyme-mediated proteolysis of fibrous biopolymers: Dissolution front movement in fibrin or collagen under conditions of diffusive or convective transport. *Biotechnol Bioeng* 1995; **48**: 89–107.
- 7 Anselmo AC, Modery-pawlowski CL, Menegatti S, Kumar S, Vogus DR, Tian LL, Chen M, Squires TM, Gupta A Sen. Platelet-like Nanoparticles : Mimicking Shape , Flexibility , and Surface Biology of Platelets To Target Vascular Injuries. 2014; : 11243–53.
- 8 Murciano JC, Medinilla S, Eslin D, Atochina E, Cines DB, Muzykantov VR. Prophylactic fibrinolysis through selective dissolution of nascent clots by tPA-carrying erythrocytes. *Nat Biotechnol* 2003; **21**: 891–6.
- 9 Korin N, Kanapathipillai M, Matthews BD, Crescente M, Brill A, Mammoto T, Ghosh K, Jurek S, Bencherif SA, Bhatta D, Coskun AU, Feldman CL, Wagner DD, Ingber DE. *Blood Vessels*. 2012; : 738–43.

- 10 Shukla M, Sekhon UDS, Betapudi V, Li W, Hickman DA, Pawlowski CL, Dyer MR, Neal MD, Mccrae KR. In vitro characterization of SynthoPlate (synthetic platelet technology and its in vivo evaluation in severely thrombocytopenic mice). *J Thromb Haemost* 2017; **15**: 375–87.
- 11 Marinković S, Gibo H, Milisavljević M, Četković M. Anatomic and clinical correlations of the lenticulostriate arteries. *Clin Anat* 2001; **14**: 190–5.
- 12 Chen H, Kaminski MD, Pytel P, Macdonald L, Rosengart AJ. Capture of magnetic carriers within large arteries using external magnetic fields. *J Drug Target* Taylor & Francis; 2008; **16**: 262–8.
- 13 Chen JP, Yang PC, Ma YH, Wu T. Characterization of chitosan magnetic nanoparticles for in situ delivery of tissue plasminogen activator. *Carbohydr Polym* Elsevier Ltd.; 2011; **84**: 364–72.
- 14 Rosengart A, Chen H, Xie Y, Kaminski M. Magnetically guided plasminogen activator-loaded designer spheres for acutestroke lysis. *Med Hypotheses Res* 2007; **2**.
- 15 Ma YH, Wu SY, Wu T, Chang YJ, Hua MY, Chen JP. Magnetically targeted thrombolysis with recombinant tissue plasminogen activator bound to polyacrylic acid-coated nanoparticles. *Biomaterials* Elsevier Ltd; 2009; **30**: 3343–51.
- 16 Huang L, ZhuGe Q, Cheng R, Zhao Y, Mao L, Yang B, Jin K, Huang W. Acceleration of Tissue Plasminogen Activator-Mediated Thrombolysis by Magnetically Powered Nanomotors. *ACS Nano* 2014; **8**: 7746–54.
- 17 Blinc A, Francis CW, Trudnowski JL, Carstensen EL. Characterization of ultrasound-potentiated fibrinolysis in vitro. *Blood* United States; 1993; **81**: 2636–43.
- 18 Chernysh IN, Everbach CE, Purohit PK, Weisel JW. Molecular mechanisms of the effect of ultrasound on the fibrinolysis of clots. *J Thromb Haemost* 2015; **13**: 601–9.
- 19 Tasci TO, Herson PS, Neeves KB, Marr DWM. Surface-enabled propulsion and control of colloidal microwheels. *Nat Commun* Nature Publishing Group; 2016; **7**: 10225.
- 20 Bleil S, Marr DWM, Bechinger C. Field-mediated self-assembly and actuation of highly parallel microfluidic devices. *Appl Phys Lett* 2006; **88**: 1–4.
- 21 Sawetzki T, Rahmouni S, Bechinger C, Marr DWM. In situ assembly of linked geometrically coupled microdevices. *Proc Natl Acad Sci U S A* 2008; **105**: 20141–5.
- 22 Tierno P, Muruganathan R, Fischer TM. Viscoelasticity of dynamically self-assembled paramagnetic colloidal clusters. *Phys Rev Lett* 2007; **98**: 1–4.
- 23 Coughlan ACH, Bevan MA. Effective colloidal interactions in rotating magnetic fields. *J*

- Chem Phys* 2017; **147**: 074903.
- 24 Purcell EM. Life at low Reynolds number. *Am J Phys* 1977; **45**: 3–11.
- 25 Shaevitz JW, Lee JY, Fletcher DA. Spiroplasma swim by a processive change in body helicity. *Cell* 2005; **122**: 941–5.
- 26 Rodenborn B, Chen CH, Swinney HL, Liu B, Zhang HP. Propulsion of microorganisms by a helical flagellum. *Proc Natl Acad Sci U S A* 2013; **110**.
- 27 Liu B, Gulino M, Morse M, Tang JX, Powers TR, Breuer KS. Helical motion of the cell body enhances *Caulobacter crescentus* motility. *Proc Natl Acad Sci U S A* 2014; **111**: 11252–6.
- 28 Gobin YP, Starkman S, Duckwiler GR, Grobelny T, Kidwell CS, Jahan R, Pile-Spellman J, Segal A, Vinuela F, Saver JL. MERCI 1: A phase 1 study of mechanical embolus removal in cerebral ischemia. *Stroke* 2004; **35**: 2848–53.
- 29 Collet JP, Park D, Lesty C, Soria J, Soria C, Montalescot G, Weisel JW. Influence of fibrin network conformation and fibrin diameter on fibrinolysis speed: Dynamic and structural approaches by confocal microscopy. *Arterioscler Thromb Vasc Biol* 2000; **20**: 1354–61.
- 30 von Burkersroda F, Schedl L, Gopferich A. Why degradable polymers undergo surface erosion or bulk erosion. *Biomaterials* 2002; **23**: 4221–31.
- 31 Lyu S, Sparer R, Untereker D. Analytical solutions to mathematical models of the surface and bulk erosion of solid polymers. *J Polym Sci Part B Polym Phys* 2005; **43**: 383–97.
- 32 Blinc A, Francis CW. Transport Processes in Fibrinolysis and Fibrinolytic Therapy. *Thromb Haemost* 1996; **76**: 481–91.
- 33 Wufsus AR, MacEra NE, Neeves KB. The hydraulic permeability of blood clots as a function of fibrin and platelet density. *Biophys J* Biophysical Society; 2013; **104**: 1812–23.
- 34 Banyai L, Patthy L. Importance of intramolecular interactions in the control of the fibrin affinity and activation of human plasminogen. *J Biol Chem* 1984; **259**: 6466–71.
- 35 Hoylaerts M, Rijken DC, Lijnen HR, Collen D. Kinetics of the activation of plasminogen by human tissue plasminogen activator. Role of fibrin. *J Biol Chem* © 1982 ASBMB. Currently published by Elsevier Inc; originally published by American Society for Biochemistry and Molecular Biology.; 1982; **257**: 2912–9.
- 36 Nieuwenhuizen W, Vermond A, Voskuilen M, Traas DW, Verheijen JANH. Identification of a site in fibrin(ogen) which is involved in the acceleration of plasminogen activation by

- tissue-type plasminogen activator. 1983; **748**: 86–92.
- 37 C-domains FR, Tsurupa G, Medved L. Identification and Characterization of Novel tPA- and Plasminogen-Binding Sites. 2001; : 801–8.
- 38 Verheijen JH, Nieuwenhuizen W, Wijngaards G. Activation of plasminogen by tissue activator is increased specifically in the presence of certain soluble fibrin(ogen) fragments. *Thromb Res* 1982; **27**: 377–85.
- 39 Verheijen JH, Nieuwenhuizen W, Traas DW, Chang GTG, Hoegge E. Differences in Effects of Fibrin(ogen) Fragments on the Activation of 1-Glu-Plasminogen and 442-Val-Plasminogen by Tissue-type Plasminogen Activator. *Thromb Res* 1983; **32**: 87–92.
- 40 Schoeman RM, Rana K, Danes N, Lehmann M, Di Paola JA, Fogelson AL, Leiderman K, Neeves KB. A Microfluidic Model of Hemostasis Sensitive to Platelet Function and Coagulation. *Cell Mol Bioeng* 2017; **10**: 3–15.
- 41 Voronov RS, Stalker TJ, Brass LF, Diamond SL. Simulation of intrathrombus fluid and solute transport using in vivo clot structures with single platelet resolution. *Ann Biomed Eng* 2013; **41**: 1297–307.
- 42 Zidansek A, Blinc A, Lahajnar G, Keber D, Blinc R. Finger-like lysing patterns of blood clots. *Biophys J* Elsevier; 1995; **69**: 803–9.
- 43 Vidmar J, Blinc A, Kralj E, Balažic J, Bajd F, Serša I. An MRI study of the differences in the rate of thrombolysis between red blood cell-rich and platelet-rich components of venous thrombi ex vivo. *J Magn Reson Imaging* 2011; **34**: 1184–91.
- 44 Diamond SL, Anand S. Inner clot diffusion and permeation during fibrinolysis. *Biophys J* 1993; **65**: 2622–43.
- 45 Wufsus AR, Rana K, Brown A, Dorgan JR, Liberatore MW, Neeves KB. Elastic behavior and platelet retraction in low- and high-density fibrin gels. *Biophys J* Biophysical Society; 2015; **108**: 173–83.
- 46 Guthold M, Liu W, Stephens B, Lord ST, Hantgan RR, Erie DA, Taylor RM, Superfinell R. Visualization and mechanical manipulations of individual fibrin fibers suggest that fiber cross section has fractal dimension 1.3. *Biophys J* Elsevier; 2004; **87**: 4226–36.
- 47 Chautems C, Zeydan B, Charreyron S, Chatzipirpiridis G, Pané S, Nelson BJ. Magnetically powered microrobots: A medicalrevolution underway? *Eur J Cardio-thoracic Surg* 2017; **51**: 405–7.
- 48 Song C, Wang P, Makse HA. A phase diagram for jammed matter. *Nature* 2008; **453**: 629–32.

- 49 Pugh N, Simpson AMC, Smethurst PA, De Groot PG, Raynal N, Farndale RW. Synergism between platelet collagen receptors defined using receptor-specific collagen-mimetic peptide substrata in flowing blood. *Blood* © 2010 by The American Society of Hematology; 2010; **115**: 5069–79.
- 50 Lehmann M, Wallbank AM, Dennis KA, Wufsus AR, Davis KM, Rana K, Neeves KB. On-chip recalcification of citrated whole blood using a microfluidic herringbone mixer. *Biomicrofluidics* 2015; **9**.

APPENDIX C

SUPPLEMENTARY MATERIALS FOR APPENDIX B

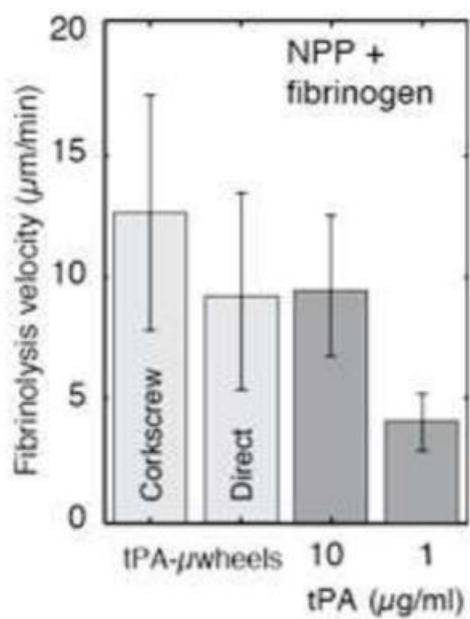


Figure C.1: Fibrinolysis velocity of PA versus tPA- μ wheels in fibrin gels derived from normal pooled plasma (NPP) with exogenous fibrinogen (final fibrinogen concentration = $10 \mu\text{g}/\text{mL}$). (Video B.S4).

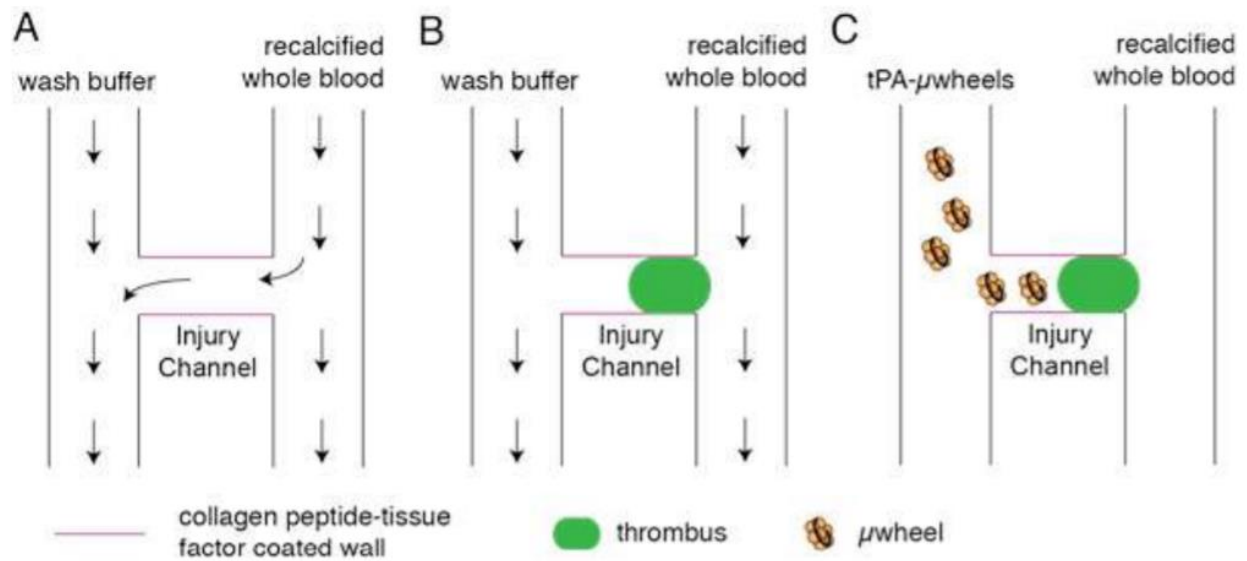


Figure C.2: Thrombus formation and tPA- μ wheel fibrinolysis in a microfluidic model of hemostasis. A. The device consists of two vertical channels connected by a horizontal channel. Recalcified citrated whole blood is perfused through the right vertical channel and a wash buffer containing sodium citrated in perfused through the left vertical channel. The horizontal channel is coated with collagen peptides to promote platelet adhesion and tissue factor (TF) to initiate coagulation. A. The inlets pressures of the two vertical channels are set so that there is a pressure difference across the horizontal channel that drives the blood from the right vertical channel to the left vertical channel. B. After ~ 5 min a thrombus occluded the horizontal channel. C. After occlusion, tPA- μ wheels are introduced through the left vertical channel and directed to the interface of the thrombus where they penetrate into the thrombus and lyse the fibrin.

APPENDIX D

SUPPLEMENTARY MATERIALS FOR CHAPTER 5

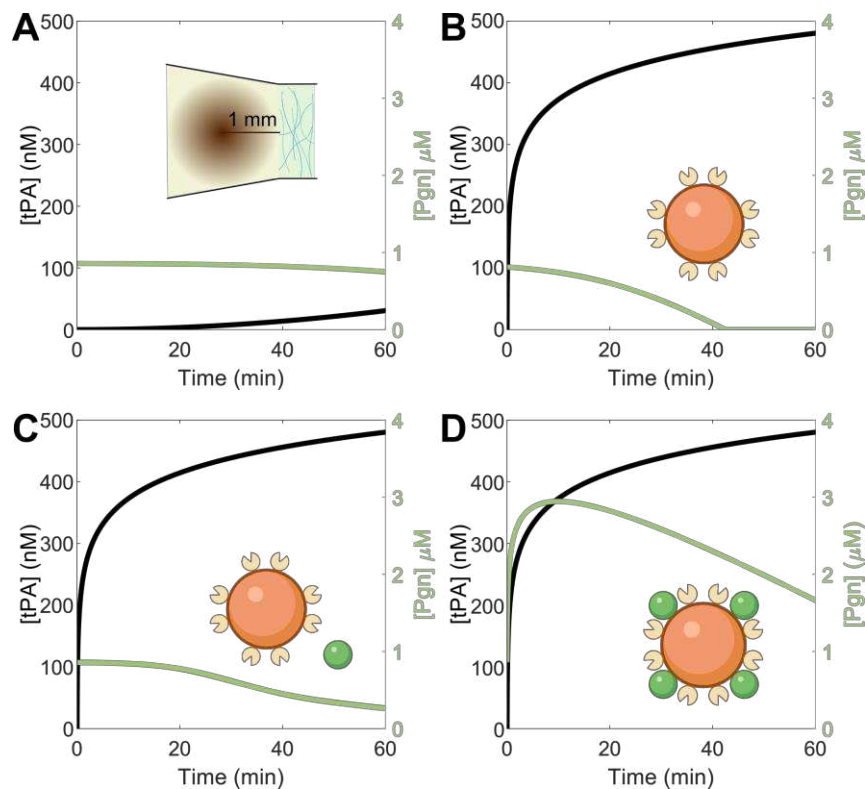


Figure D.1: A) Local concentration of tPA and plasminogen 1 mm from the injection of a 50 nM bolus of tPA and 1 μM plasminogen. B) Local concentration of tPA and plasminogen 1mm from the injection of 10⁵/μL tPA-beads. C) Local concentration of tPA and plasminogen 1mm from the injection of 10⁵/μL tPA-beads and 10⁶/μL pgn-mMSN. D) Local concentration of tPA and plasminogen 1 mm from the injection of 10⁵/μL pgn-tPA-beads.

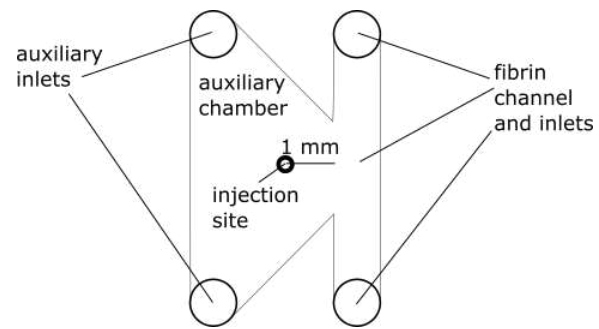


Figure D.2: Schematic of microfluidic device used for fibrinolysis experiments.

APPENDIX E

LIST OF ADDITIONAL FILES

Permissions:

Permissions.pdf: Includes all publisher and co-author permissions for reproduced materials.

Chapter 3:

Video 3.S1: Rotational velocity for Janus particles can be quantified with contrast between hemispheres. Silver film thickness is ~50 nm.

Video 3.S2: Spheres rotating at higher rates translate faster but at a larger gap width. Video provided at half speed.

Video 3.S3: Particles roll faster and at smaller gap widths when under higher loads. Video provided at half speed.

Video 3.S4: Particles at gap widths less than or equal to the surface roughness experience stick-slip rolling. Enhanced scattering is apparent at higher velocities when particles are closer to the surface.

Chapter 4/Appendix B:

Video B.S1: Direct and corkscrew motion of small μ wheel.

Video B.S2: Accumulation of μ wheels at fibrin gel over 30 min period.

Video B.S3: Lysis of NPP and PRP clots using μ wheels and free tPA.

Video B.S4: Comparison of μ wheel penetration into the fibrin gel using direct and corkscrew modes.

Video B.S5: Lysis of a platelet-rich clot formed from whole blood using μ wheels driven in the corkscrew mode.

Chapter 5:

Video 5.S1: Brightfield (left) and fluorescence (right) time lapses of the dissolution of plasma clots using soluble tPA and various μ wheel populations. Video playback is accelerated 12X.

Video 5.S2: Comparison of direct and corkscrew trajectories for a μ wheel monomer driven by a 10 Hz, 6.2 mT rotating magnetic field.

Video 5.S3: Dissolution of plasma clots using pgn-tPA- μ wheels in either direct or corkscrew modes. Front positions are indicated with red lines. For the corkscrew mode, green circles track penetrating pgn-tPA- μ wheels.